

Thermal Convection in Vertically Suspended Soap Films

by

Jie Zhang

B.S., University of Science & Technology of China, 1999

M.S., University of Pittsburgh, 2001

Submitted to the Graduate Faculty of  
Arts and Sciences in partial fulfillment  
of the requirements for the degree of  
Doctor of Philosophy

University of Pittsburgh

2005

UNIVERSITY OF PITTSBURGH  
FACULTY OF ARTS AND SCIENCES

This dissertation was presented

by

Jie Zhang

It was defended on

[March 29, 2005]

and approved by

XiaoLun Wu, Department of Physics and Astronomy

Jeremy Levy, Department of Physics and Astronomy

Rob Coalson, Department of Chemistry

Walter I. Goldberg, Department of Physics and Astronomy

Yadin Goldschmidt, Department of Physics and Astronomy

Dissertation Director: XiaoLun Wu, Department of Physics and Astronomy

# Thermal Convection in Vertically Suspended Soap Films

Jie Zhang, PhD

University of Pittsburgh, 2005

In normal fluids, a temperature difference can create a density difference. In the presence of the gravitational field, denser fluid will fall and lighter fluid will rise, causing fluid motion known as thermal convection. This type of convection can occur on different scales, from a single growing crystal to mantle movement inside the earth. Although many experiments have been conducted in unstably stratified fluids, there have been few laboratory experiments studying convective turbulence in stably stratified fluids, which is more common in nature. Here I present a two-dimensional (2D) convection in a stably stratified vertical soap film. It was found that the interaction between the gravitational potential energy, due to the 2D density fluctuation, and the kinetic energy is important. This interplay between the two energy sources manifests itself in the statistical properties of velocity and 2D density fluctuations in the system. Our experimental findings shed new lights to a turbulent system that strongly couples to a non-passive field.

## TABLE OF CONTENTS

1.	Introduction.....	1
1.1.	Rayleigh-Bénard convection.....	1
1.2.	Thesis overview .....	2
2.	Thermal Radiation and Thickness Fluctuations.....	4
2.1.	Abstract.....	4
2.2.	Introduction.....	4
2.3.	Experimental Methods.....	7
2.3.1.	Thermal Convection Setup .....	7
2.3.2.	Flow patterns.....	9
2.3.3.	Thermal Radiation from Semi-transparent Films and Its Measurement.....	11
2.4.	Experimental Results .....	16
2.4.1.	Temporal Fluctuations of Thermal Radiation in Thin Films .....	16
2.4.2.	Spatial Fluctuations of the Film Thickness Determined by 2D IR Imaging.....	19
2.4.3.	Statistics and Scaling Relations of 2D Density Fluctuation .....	28
2.4.4.	Full-Field 2D Density Flux Measurements.....	32
2.5.	Summary .....	34
2.6.	Appendix A.....	36
2.7.	Appendix B .....	40
3.	2D Density Fluctuations and 2D Compressibility .....	43
3.1.	Abstract.....	43
3.2.	Introduction.....	43
3.3.	Experimental Results .....	44
3.4.	Discussion.....	50
3.5.	Summary .....	53
4.	2D Density Field Measurements Using an IR Camera.....	54
4.1.	Multifractal Measurements of Thickness Dissipations.....	54
4.2.	The Potential Energy Field .....	60
4.3.	The skewness of the thickness fluctuations .....	64
4.3.1.	Lumley’s Theory.....	64
4.3.2.	Re-deriving Lumley’s Result Using Bolgiano’s Assumption .....	65
4.3.3.	Skewness Measurements .....	67
4.3.4.	Summary .....	70
5.	Single Point Velocity Statistics.....	73
5.1.	Abstract.....	73
5.2.	Introduction.....	73
5.3.	Experimental Results .....	74
5.4.	Summary .....	92
6.	Velocity Intermittency in a Buoyancy Sub-range.....	93
6.1.	Abstract.....	93

6.2.	Introduction.....	93
6.3.	Experimental Method.....	94
6.4.	Experimental Results .....	96
6.5.	Summary .....	102
BIBLIOGRAPHY .....		104

## LIST OF FIGURES

- Figure 2-1: Experimental Setup. The experimental setup consists of a thermal convection cell, which is made of two large aluminum cylinders stacked on top of each other. Each measures 10 cm in diameter and height. The lower cylinder is heated by stick-on Minco heaters and the upper one is cooled by four solid-state coolers. Separation of the two blocks can be adjusted so that films of different heights can be formed. Inside the lower cylinder is a slim stainless steel vessel, which serves as a reservoir of soap solution and is connected to an external soap-solution bottle. The height of the soap solution surface level inside the vessel can be adjusted. A thin stainless steel frame, 50  $\mu\text{m}$  thick, is used to draw the film from the reservoir. For this experiment, the size of the film was fixed at  $2 \times 2 \text{ cm}^2$ . For the thermal radiation measurement, the imaging optics was set up such that a single point in the film was directly mapped onto a light detector using 2f-2f geometry. In order to reduce noises, the incoming radiation signal was modulated by an optical chopper, amplified first by a pre-amplifier and then by a lock-in amplifier. A HeNe laser was used to aid the alignment of optics. The right corner shows a 3D plot of the set up. .... 8
- Figure 2-2: Shadowgraphs of Thermal Convection Patterns in Soap Films. The images were taken by a CCD camera with a shutter speed of 1 ms. The height and width of the film were respectively 2 by 2 cm. (a) The shadowgraphs were taken at a  $\Delta T=31 \text{ K}$  (a) and a  $\Delta T=62 \text{ K}$  (b). In both cases, thermal plumes of various sizes are clearly discernible. However, for a low temperature gradient case (a), plumes can only climb half way up the film, leaving the top half essentially quiescent. One can occasionally observe, as shown in (a) that a hot plume ascends from the lower thick film region into the upper thin film region, or the secondary emission. This type of plumes is not as energetic as the ones directly ejected from the bottom of the cell. In the presence of a large temperature difference (b), plumes can readily reach to the top of the film, causing vigorous mixing throughout the entire film. ... 10
- Figure 2-3: Schematics of Multiple-beam Reflection in a Film. The input light  $I_0$  is multiply reflected and attenuated due to IR light absorption. The film is assumed to have a uniform thickness  $h$  and a constant absorption length  $Z_0$ . The light reflectivity  $r$ , transmittance  $t$ , and emissivity  $\varepsilon$  are calculated based on this geometry. See text for details. .... 13
- Figure 2-4: Thermal Radiation from a Thick Glass Plate. This is a calibration curve using a Pyrex glass plate. A Minco heater was attached to the back of the plate and its surface temperature was monitored by a thermister. The vertical axis is the voltage output from the lock-in amplifier. As shown in the plot the radiation signal scales linearly with  $T^4$  as expected. Using the known thermal emissivity of glass  $\varepsilon=0.94$ , the sensitivity of the setup can be calculated. .... 15
- Figure 2-5: A Time Trace of Radiation Signal from a Turbulent Convection Film. The data was digitized at a rate of 1 kHz and at a 14-bit resolution. The measurement condition corresponds to  $\Delta T=55 \text{ K}$  and  $T_{\text{top}}=15.5 \text{ }^\circ\text{C}$  fixed. The large voltage fluctuations are due to passages of thermal plumes through the detected area,  $\sim 1 \text{ mm}$  in diameter. The small-scale fluctuations are presumably due to fine internal structures of plumes. .... 17

Figure 2-6: Power Spectrum of Thermal Radiation from a Turbulent Convection Film. The upper curves are measured from the film at  $y=1.3$  (black),  $1.0$  (green), and  $0.7$  cm (red), and the lower curve is the background without the film. The  $y$  is defined as  $y=0$  at the foot of film and  $y=2$ cm at the film top. The power spectrum shows two scaling regimes separated by a characteristic frequency  $f_c \sim 8$  Hz. Interestingly the scaling behavior  $\Gamma(f) \sim f^{-1.4}$  in the low-frequency regime ( $f < f_c$ ) is close to the theoretically expected ones. See text for more details. .... 18

Figure 2-7: Thermal Convection in Different Geometries (a) A “rough” lower boundary, (b) a semi-elliptical boundary, and (c) a triangular boundary. The temperature difference  $\Delta T=41$  K. Though thermal plumes are more likely to be emitted from the “rough” boundary, the measured power spectra, for the rough cell (green), the semi-elliptical cell (black), and triangular cell (red), are nonetheless similar as delineated in (d). .... 20

Figure 2-8: Thickness Map Measured by an IR Transmission Technique. (a) An instantaneous thickness at a  $\Delta T=61.5$  K and with  $T_{top}=14$  °C fixed. The presence of a large-scale circulation, in this case clockwise, makes the thermal plumes to be generated near the side boundary of the cell. One also observes small granular structures in the background, suggesting film thickness undulates on those scales. (b-d) Time averaged thickness maps obtained at  $\Delta T=37$  K (b),  $49.5$  K (c), and  $61.5$  K (d), respectively. For a low  $\Delta T=37$  K (b), thermal plumes are predominantly generated from the bottom, as a result, the thickness stratifies uniformly in the vertical direction. For a  $\Delta T \sim 49.5$  K (c), some plumes gain sufficient energy to climb the film’s top. Convection takes place in entire film. However, this flow is a peculiar one in that the emission of thermal plums is not symmetric. As picture (c) shows, plumes emit mostly from the lower right corner, breaking the left-right symmetry (LRS) of the system. For a large  $\Delta T=61.5$  K (d), large scale-circulation causes film to be thick near boundaries and thin in the center. The LRS is nearly recovered. .... 22

Figure 2-9: Instantaneous Thickness Variations  $\Delta h$  Along a Center Horizontal Line of a Turbulent Convection Soap Film. This curve represents the thickness distribution along the vertical height,  $y=1.2$  cm, of the film shown in Fig. 2-8(a). Here the mean thickness was subtracted. One observes that the thickness varies on large and small scales. Thermal plumes give most significant contributions to the thickness variations. A sharp cliff, indicated by the arrow, can also be observed in the above figure. .... 23

Figure 2-10: The Vertical Mean Thickness Profile  $h(y)$  and the Standard Deviation  $\delta h(y)$ . Both measurements were made along the central vertical axis of the film using the thickness maps presented in Fig. 2-8(b) and 2-8(d). The top figure (a) corresponds to a  $\Delta T=37$  K and the bottom figure (b) corresponds to a  $\Delta T=61.5$  K. In both figures, the average film thickness  $h$  is represented by the squares and the standard deviation  $\delta h$  is represented by circles. The horizontal axis is the vertical height  $y$  of the film. .... 27

Figure 2-11: Probability Density Function of the Film Thickness Variations. (a) Different symbols correspond to  $\tau=1/256$  (open circles),  $5/256$  (open squares),  $10/256$  (diamonds),  $20/256$  (triangles),  $40/256$  (asterisks),  $80/256$  (crosses),  $0.5$  (tilted triangles), and  $1.0$  s (pluses). (b) The skewness as a function of  $\tau$ . We noted that the skewness is significantly greater in the range  $0.1 < \tau < 0.5$  s, which coincides rather well with the Bolgiano regime.... 31

Figure 2-12: The Ensemble Averaged Thermal Flux in Presence of a Large-scale Circulation. Simultaneous velocity and thermal radiation fields were measured at a  $\Delta T=61.5$  K and with  $T_{top}=14$  °C. This allows the local mass flux to be calculated. Even after the ensemble

average over 500 fields, the mass flux still does not average to zero but instead shows a closed loop with a clockwise circulation. The loop is squashed in the vertical direction, resulting from the density stratification. ....	33
Figure 2-13: The Measured Probability Density Functions of Radiation Power. The probability density functions measured in the presence of the soap film (right), the water vapor but no film (middle), and in the absence of both water vapor and the film (left). The measurements were carried out under the same condition as in Fig. 2-5. ....	39
Figure 2-14: The Infrared Absorption Length $Z_0$ of Water as a Function of Wavelengths. See Ref. [54]. ....	41
Figure 2-15: The Plot of the Function $f(h,\lambda)=\exp(-h/Z(\lambda))$ for Different Film Thicknesses $h$ . The function $f$ is plotted for the relevant film thickness observed in our experiment. The symbols are respectively $h=1$ (squares), 3 (circles), 5 (up triangles), 7 (down triangles), and 9 $\mu\text{m}$ (diamonds). The plot is restricted to the camera's spectral range 8-14 $\mu\text{m}$ . ....	42
Figure 2-16: The Plot of the Normalized Transmittance $F(h)$ vs. the Film Thickness $h$ . The area calculated underneath each curve in Fig. 2-15 is presented. The semi-logarithmic plot shows a quasi-linear behavior. The slope of the line yields the inverse of the effective absorption length $Z_0$ over the spectral width 8-14 $\mu\text{m}$ . For our system $Z_0=7.83 \mu\text{m}$ . ....	42
Figure 3-1: Convection Patterns in Soap Films. The pictures on the left were acquired using shadowgraph technique. The shutter speed of the video camera was 1 ms. From top to bottom, $\Delta T= 31$ (a), 50 (b), and 62 K (c), respectively. At the top of the film $T_{\text{top}}=14 \text{ }^\circ\text{C}$ was fixed in all measurements. Typical velocity fields corresponding to $\Delta T$ s are displayed next to the shadowgraphs. The most striking feature is the gradual erosion of the top quiescent part of the fluid as $\Delta T$ increases. ....	46
Figure 3-2: The thickness power spectra $\Gamma(f)$ . They consist of two power-law regimes $\Gamma_l(f) \sim f^{-\alpha}$ and $\Gamma_h(f) \sim f^{-\beta}$ separated by $f_c$ . (a) For a small $\Delta T(=44\text{K})$ , $\alpha=1.4\pm 0.1$ is consistent with the Bolgiano scaling. (b) For a large $\Delta T(=51\text{K})$ , $\alpha=1.0\pm 0.1$ is consistent with the Batchelor exponent. The background radiation is much weaker than the signal, as shown by the lower curves. The compensated spectra are presented in the insets. ....	48
Figure 3-3: The scaling exponent $\alpha$ and the compressibility $C$ vs. $\Delta T$ . Both $\alpha$ and $C$ show a sudden jump as $\Delta T$ crosses $\Delta T_C \sim 48 \pm 2 \text{ K}$ . The inset of (a) presents the scaling exponent $\beta$ vs. $\Delta T$ . ....	49
Figure 3-4: The thickness profile $\bar{h}(y)/Z_0$ vs. vertical height $y$ . The two figures correspond to $\Delta T=37 \text{ K}$ (a) and $\Delta T=61.5 \text{ K}$ (b). The profiles are horizontally averaged. ....	51
Figure 4-1: A Thickness Dissipation Field $\varepsilon(x,y)$ . The $y$ axis is along the vertical direction and the $x$ axis is along the horizontal direction, with the origins (0,0) being the top left corner of the film. One pixel size is 78 $\mu\text{m}$ . ....	56
Figure 4-2: The log-log plot of the $q^{\text{th}}$ moment of the thickness dissipation field $\langle \sum (E_i/E_0)^q \rangle$ versus the box size $l$ . The different symbols used in the plots stand for $q=-8$ (the open circles), $-7$ (the open squares) ... $q=8$ (the solid triangles right). ....	57
Figure 4-3: The Generalized Dimensions $D_q$ as a Function of Integer Number $q$ . ....	59
Figure 4-4 The Multifractal Spectrum $F(\alpha)$ of the Singularity Exponent $\alpha$ . ....	59
Figure 4-5: A Potential Energy Field $pe(x,y)$ . The origin (0,0) is the lower left corner. The intensity of $pe(x,y)$ is in arbitrary units. Those black lines are contour lines with constant $pe$ . ....	61

Figure 4-6: The 2D Correlation of $pe$ as a Function of Separation Distance ( $l_x, l_y$ ). The lower plot is the 1D correlation cut along horizontal and vertical directions, where an arrow indicates the Bolgiano length scale ( $l_B \approx 2$ mm). The red (black) curve is the correlation in the horizontal (vertical) direction. ....	63
Figure 4-7: A thickness fluctuation field $\delta h(x,y)$ and its thickness gradient field. The origin (0,0) is the top left corner of the film. ....	68
Figure 4-8: The PDF of $\delta h_l \equiv \langle \delta h(x,y+l) - \delta h(x,y) \rangle$ . Here the angle bracket $\langle \rangle$ is the ensemble average over the whole film for all $(x,y)$ followed with a time average of all pictures. The length scale $l_s$ are in the units of pixels. Different symbols are $l=1$ (circles), 2 (squares), 4 (diamonds), 8 (triangle-ups), 16 (triangle-lefts), 32 (triangle-downs), 64 (triangle-rights), and 90 pixels (stars). One pixel is $78 \mu\text{m}$ . ....	71
Figure 4-9: The skewness ( $\equiv \langle \delta h_l^3 \rangle / \langle \delta h_l^2 \rangle^{3/2}$ ) along the vertical direction as a function of $l$ ... ..	72
Figure 4-10: A simple sketch demonstrates the existence of positive and negative skewness on small and large scales. ....	72
Figure 5-1: Three shadow graphs (a), (b), and (c) of the thermal convection. These three pictures were taken consecutively with a time delay $\tau=1/30$ s. Red Crosses in (a) illustrate the measurement locations of the single point velocity measurements. There exists a mixing zone as indicated by the blue arrows, with height $L$ . ....	75
Figure 5-2: Single-point Velocity PDF along the Horizontal $x$ Direction (a) and along the Vertical $y$ direction (b). In (a) and (b), the circle symbol is measured at the center, and the square symbol is measured 2mm away from the center. In (a), PDF are close to super-Gaussian forms in the tail part and in (b) PDF have large slow decay tails for positive $v_y$ . $\Delta T=31.1$ K in the measurements, and the film with a square geometry is used. ....	77
Figure 5-3: Another set of PDF measured in a square geometry at a different $\Delta T=37.1$ K with all other conditions same as Fig. 5-1. ....	79
Figure 5-4: Single point velocity PDF measured in a square geometry at $\Delta T=41.7$ K in the absence of large scale circulation. Different symbols stand for different measurement spots away from the center of the cell, circles (0 mm), square (1 mm), diamond (2 mm), triangle-up (3 mm), triangle-left (4 mm), triangle-down (6 mm) and triangle-right (8mm). Again, (a) plots PDF of $v_x$ , and (b) plots PDF of $v_y$ . ....	80
Figure 5-5: Local mean flow $\langle v_x \rangle$ (a), $\langle v_y \rangle$ (c), and the local fluctuations $\langle (v_x - \langle v_x \rangle)^2 \rangle^{1/2}$ (b), $\langle (v_y - \langle v_y \rangle)^2 \rangle^{1/2}$ (d) as a function of distance $\Delta x$ . The distance $\Delta x$ is defined as $\Delta x=0$ at the middle of the film and $\Delta x=1$ cm at the right side wall. ....	82
Figure 5-6: Plume Emission Statistics in 2D Convection. The plume velocity (a) and the emission rate $n_{plume}$ (number of emitting plumes per 33 ms) (b) were measured using consecutive shadowgraphs similar to the ones shown in Fig. 5-1. The measurements were taken when an incipient plume just emerges from the lower thermal boundary layer. ....	84
Figure 5-7: (a) $\langle v_y \rangle$ as a function of vertical height $y$ . Here $\langle \rangle$ stands for the assemble average over a horizontal layer with same height $y$ in one velocity field and then average over all velocity fields. Only two temperature differences, $\Delta T=67.7$ K (circles) and $\Delta T=25.5$ K (diamonds), are plotted to illustrate $\langle v_y \rangle \neq 0$ . Other $\Delta T$ s show similar behavior. (b) The $v_{rms}$ (black squares) and $\langle v_y^2 \rangle_{max}^{0.5}$ (red circles) as a function of $\Delta T$ . The dot dashed line is guide to the eye. ....	86
Figure 5-8: (a) $\langle v_y^2 \rangle^{1/2} / \langle v_y^2 \rangle_{max}^{1/2}$ and (b) $\langle v_x^2 \rangle^{1/2} / \langle v_x^2 \rangle_{max}^{1/2}$ vs. height $y$ . $\langle \rangle$ indicates the ensemble average of a horizontal layer at a height $y$ at a $\Delta T$ . The inset in (a) is a plot of $y_p$	

(peak of  $\langle v_y^2 \rangle^{1/2} / \langle v_y^2 \rangle_{\max}^{1/2}$ ) vs.  $\Delta T$ . The inset in (b) plots  $y_1$  (black color, max y of  $\langle v_y^2 \rangle^{1/2} / \langle v_y^2 \rangle_{\max}^{1/2}$ ) and  $y_2$  (red color, max y of  $\langle v_x^2 \rangle^{1/2} / \langle v_x^2 \rangle_{\max}^{1/2}$ ) vs.  $\Delta T$ . Different symbols in (a-b) represent  $\Delta T=21.6$  (circle), 25.5 (square), 30.9 (diamond), 36.3 (triangle-up), 39.7 (triangle-left), 45.5 (triangle-down), 52 (triangle-right), 55.5 (star), 64 (plus) and 67.7 K (A). ..... 87

Figure 5-9: Single point velocity PDF measured in a square geometry at  $\Delta T=70-14.3=55.7$  K with large scale circulations. Different symbols stand for different measurement spots away from the center of the cell, circles (0 mm), square (1 mm), diamond (2 mm), triangle-up (3 mm), triangle-left (4 mm), triangle-down (6 mm) and triangle-right (8mm). ..... 91

Figure 6-1: The experimental setup. The film is sandwiched between two aluminum blocks and is in contact with a soap-solution reservoir. The velocity difference  $\delta v_l$  is measured by two LDV probes at locations indicated by two “X” on the sketch to the upper right. Only the horizontal component of the velocity is measured. .... 95

Figure 6-2: (a) The velocity-difference pdf's  $P(\delta v_l)$  as a function of  $l$  (in  $\mu\text{m}$ ), 120 (squares), 240 (circles), 481 (up triangles), 721 (down triangles), 962 (diamonds), 1442 (left triangles), 1923 (right triangles), 2404 (hexagons), 3606 (stars), 4808 (pentagons), 7212 (pluses), 9616 (crosses), 12020 (asterisks). The inset is the flatness  $F(l)$  as a function of  $l$ . The solid line is a guide to the eyes. (b) The log-log plot of  $S_2(l)$ . The line indicates a power-law  $S_2(l) \sim l$  in the Bolgiano regime ( $10^3 < l < 10^4 \mu\text{m}$ ). The inset is a plot of  $S_{(3)}(l) (= \langle \delta v_l^3 \rangle)$ , showing  $S_{(3)}(l) \sim l^{1.5}$ . The  $S_{(3)}(l) > 0$  indicates that there is an inverse energy cascade in our system. ... 97

Figure 6-3 (a): A typical velocity field measured by PIV at  $\Delta T=63.5$  K. The presence of a LSC is evident. The velocity field is isotropic as indicated by the 2D energy spectrum  $E(k_x, k_y)$  in (b). The division in the horizontal and vertical axes is  $\Delta k_x = \Delta k_y = 5 \text{ cm}^{-1}$ . ..... 99

Figure 6-4: (a) The log-log plot of  $S_q(l) \sim l^{\zeta_q}$  for  $1 \leq q \leq 8$  in the Bolgiano regime. (b) The exponent  $\zeta_q$  is plotted against  $q$ . The dashed line is based on Bolgiano's theory, the dot-dashed line is our measurement, assuming no intermittency, and the solid line is the fit to the random cascade model  $\zeta_q = q/2 + (\mu/18)(3q - q^2)$ , where  $\mu=0.42$ . ..... 103

## **Acknowledgments**

I am greatly indebted to my advisor, XiaoLun Wu for his great support during my study in his lab.

I would also like to thank Walter I. Goldberg, who is such a kind gentleman that he is always willing to discuss questions with students and is always encouraging students.

I am grateful to my friend Yonggun Jun. We enjoyed our time working together in the lab. I am amazed how smart he is when we discussed many interesting physics problems.

I am also indebted to John R. Cressman, Matthew Shtrahman, Radu Moldovan, Mahesh Bandi, Pedram Roshan, Suddhashil Chattopadhyay, and Emily Chapman for their help.

Finally, I would like to thank my family, especially my wife, Miao Chen, for their love and support.

## 1. Introduction

### 1.1. Rayleigh-Bénard convection

In normal fluids, a temperature difference can create a density difference. If the fluid is placed in a gravitational field, the denser part of the fluid will tend to fall and the lighter part will rise. Different flow structures can be created depending on the heating rate [1]. Applying a very low heating rate, the fluid remains quiescent and the heat is transported through pure conduction. As the heating rate increases, the fluid motion gradually evolves from steady motion to oscillatory motion and to chaotic motion. This process is known as bifurcation in non-linear dynamics [2]. The fluid motion caused by temperature difference is known as thermal convection. Thermal convection can occur on all different scales, from a single growing crystal in a melt to mantle movement inside the planet earth [1].

Among most thermal convection experiments studied in laboratories, Rayleigh-Bénard convection (RBC) is the most common. It usually consists of a horizontal layer of fluids sandwiched between two parallel plates. The top plate is cooled and the bottom plate is heated. The fluids can be liquid, gas, liquid crystal or some other interesting materials. Under Boussinesq approximation [3], there are two important dimensionless parameters. The first parameter is the Rayleigh number  $Ra$ , defined as:  $Ra \equiv \alpha g \Delta T L^3 / \nu \kappa$ , where  $\alpha$  is the thermal expansion coefficient of the fluids,  $g$  is the gravitation constant,  $\Delta T$  is the temperature difference between the two plates,  $L$  is the system height,  $\nu$  is the kinematic viscosity and  $\kappa$  is the thermal conductivity of the fluids. Naively  $Ra$  can be thought of as a dimensionless temperature difference to characterize the strength of thermal driving of the system. The second important parameter is the Prandtl number  $Pr$ , defined as  $Pr \equiv \nu / \kappa$ . The  $Pr$  number has the important interpretation that it is the ratio between the thicknesses of velocity boundary layer and thermal boundary layer.  $Pr$  is only a function of physical properties of fluids. Liquid metals have  $Pr$  less

than 1, and most gases have Pr close to one. In pure water, Pr is around 7. For different systems with the same geometry, RBC will be characterized completely by Ra and Pr.

Intuitively, the physical meaning of Ra can be simply understood based on dimensional ground. The thermal convection problem contains only three relevant time scales. The first is  $t_v \sim L^2/\nu$ , the time scale of momentum diffusion. Here system height L is chosen since it is the only length scale of the system, assuming the system is infinite in other dimensions. The second is  $t_\kappa \sim L^2/\kappa$ , the time scale of heat diffusion. The third is  $t_s \sim (L/\alpha g \Delta T)^{0.5}$ , which is the time of the ballistic motion of a fluid blob due to buoyancy. Thus,  $t_s^2$  and  $t_v t_\kappa$  have the same dimension, and they must satisfy  $t_s^2 \ll t_v t_\kappa$  in order to generate convective motion because if the time for a hot (or cold) blob to lose momentum or heat is too short the blob will quickly reach equilibrium with its neighboring and become motionless. The ratio  $t_v t_\kappa / t_s^2$  gives Rayleigh number of a system.

For a given system, there exists a critical Rayleigh number  $Ra_c$ . Below  $Ra_c$ , the system is stable to infinitesimal perturbations. Beyond  $Ra_c$ , the system will become unstable. Using linear stability analysis, it can be shown that a system with two infinite solid walls (top and bottom) has  $Ra_c \approx 1700$  [4]. A quick estimation can easily show that a layer of pure water at room temperature with 1 cm height, 1 K temperature difference has  $Ra \approx 15,000$ , which is already one order magnitude larger than  $Ra_c$ . This may explain why thermal convection is so common in nature.

## 1.2. Thesis overview

This thesis presents an experimental study of thermal convection in vertically suspended soap films. The convection in our soap film is *not* a Rayleigh-Bénard type because of its stable stratification. The thesis is organized as following.

Chapter 2 concerns measurement of the thermal radiation emission from the film using an infrared detector. As will be described in this chapter, the radiation signal carries the information of local thickness fluctuations. The mean thickness profiles of the film were also measured using a single point scanning infrared camera.

Using the radiation measurement technique developed in chapter 2 and Particle Image velocimetry, in chapter 3, the two dimensional (2D) density fluctuations and the 2D compressibility are studied at different temperature differences. These quantities show different behaviors in a strongly stratified state and a strongly mixed state, which is characterized by a large scale circulation (LSC) in the system.

While chapter 2 and chapter 3 mainly focus on local film thickness fluctuations, chapter 4 studies the 2D thickness fluctuation field in the whole film at a fixed high temperature difference in the existence of the LSC. The potential energy field correlation, the multifractal distributions of thickness dissipations, the skewness of thickness fluctuation along the vertical direction, and some other properties are included in this chapter.

Finally, in the last two chapters, velocity statistics (Chapter 5) and velocity intermittency in a Buoyancy sub-range (chapter 6) are presented.

## 2. Thermal Radiation and Thickness Fluctuations

### 2.1. Abstract

We present the successful thermal radiation measurements from freely suspended soap films using a single-point mercury-cadmium-tellurium detector and a lock-in amplifier. The film is driven by a vertical temperature gradient similar to the classical Rayleigh-Bénard convection. A systematic method is developed to calibrate the emitted thermal power and its temporal fluctuations at a local point on the film. Despite the small film thickness, which is typically a few microns in thickness, thermal radiation is measurable and can yield useful information about local temperature and thickness of the film. We show that for the IR detector with a spectral range within 8-14  $\mu\text{m}$ , the dominant temporal contribution to the radiation signal is due to fluctuations of the thermal emissivity of the film, which is a function of the film thickness  $h$ . The technique thus provides a rapid and convenient means to measure mass density variations in the film. A variant of this technique allows direct imaging of the film thickness and reveals for the first time the correlation between the formation of a large-scale circulation and the asymmetric mass distribution in the convection cell. Our experiment also shows that it is feasible to measure temperature fluctuations in the film if the detector is operated near the 3  $\mu\text{m}$  wavelength range, where water absorbs electromagnetic waves most strongly with an absorption length less than one micrometer. In this strong absorption regime, a film of a few microns in thickness is essentially opaque, behaving like an ideal blackbody with emissivity close to unity. In this case, the radiated thermal power gives a direct measurement of local temperature in the film.

### 2.2. Introduction

Studies of fluid flow and turbulence using freely suspended aqueous and liquid crystal films have attracted much attention over the past decade [5-11]. This interest can be traced to the unique physical properties of these films being so thin that fluid motion can be treated as nearly

two dimensional (2D). It has been shown recently based on general physical grounds that an aqueous film with a trace of soluble surfactants obeys the 2D incompressible Navier-Stokes equation if the following two conditions are satisfied: (i) The in-plane root mean square (rms) velocity  $U$  varies on a scale  $L$  that is much larger than film thickness  $h$ , and (ii)  $U$  itself is much smaller than the elastic (or the Marangoni) wave velocity  $v_e$  [12]. The first condition is readily satisfied in most experiments since  $h \sim 1 \mu\text{m}$  and  $L$  is of order of a few millimeters to several centimeters, making  $h/L < 10^{-3}$ . On the other hand, the second condition is more demanding but can still be satisfied in many experiments since the elastic velocity of film is  $\sim 10 \text{ m/s}$  [5, 12] and the typical turbulent velocity fluctuations  $v_{\text{rms}}$  is several centimeters per second, making  $v_{\text{rms}}/v_e \sim 10^{-1}$  or less. Thus, freely suspended soap films have a great potential for exploring fluid physics in low spatial dimensions where a wealth of new phenomena can be studied [13-16].

A few years ago it was discovered that when a soap film is exposed to a large vertical temperature gradient, warm at the film's bottom and cold at its top, steady-state convection could be established [17]. The convection has a remarkable effect of prolonging the film lifetime from a few seconds, if the temperature gradient were absent, to almost indefinitely. This is because convective mass current continuously replenishes fluid loss at the top of the film due to gravitational stratification, making the entire film more uniform. In a steady state, the thermal convection can be vigorous, achieving rms velocity fluctuation of several centimeters per second in a film that measures only a few centimeters across. The phenomenon is in sharp contrast with earlier attempts using freely suspended liquid crystal films where the convection velocity  $\sim 10 \mu\text{m/s}$  was observed [18, 19]. The ability to induce strong convection in these freely suspended aqueous films makes them ideally well suited for studying 2D convective turbulence, where there are many theoretical predictions [16, 20-24] but very few laboratory experiments. However since in the early experiment we were unable to measure temperature and thickness in the film, the latter corresponding to the 2D mass density of the fluid, the behavior of these important dynamic variables remain largely unknown.

In this chapter, we report new studies of thermal turbulence in freely suspended soap films by exploiting the fact that long wavelength photons can readily escape from the interior of the film and can be detected by sensitive IR detectors. These photons carry useful information

about their local environment, such as temperature and 2D fluid density; both are important for quantitative understanding of thermal turbulence. Unfortunately there is no off-the-shelf instrument that can be readily used to measure weak thermal radiation on time scales shorter than fluctuation times of turbulence in the soap films. One of the objectives of this chapter is thus to report development of a remote IR sensing technique and its calibration. Specifically, we report the implementation of a single-point radiation thermometer based on a phase-lockin technique and a mercury-cadmium-tellurium (HgCdTe) detector, which is cooled to liquid nitrogen temperature. A full-field IR transmission imaging system was also implemented to visualize directly entire film thickness profile  $h(x,y)$ . This latter technique is a generalization of an earlier experiment in which IR transmission was used to measure the thickness at a *local* point in the film [25]. The single-point radiation thermometry and the full-field IR imaging method are complementary techniques in that the former is suitable for measuring fast temporal fluctuations of thermal radiation while the latter is suitable for imaging spatial distribution of the 2D mass density. The combination of the two techniques allows us to draw an important conclusion that the measured spatial and temporal variations of the radiation signals are dominated by the fluctuations of the thermal emissivity of the film, which are related to the film thickness. This subtle point has not been properly treated in a recent experiment [26].

The validity of our experimental techniques is demonstrated by the investigation of temporal fluctuations of the 2D mass density in the film driven by a large temperature gradient. Interestingly, even with a moderate film size,  $2 \times 2 \text{ cm}^2$ , the measured power spectrum of density fluctuations is in remarkably good agreement with Bolgiano's theoretical prediction for a density-stratified fluid [27, 28]. The steady-state density profile in the film is shown to be a function of the temperature gradient. An interesting density inversion, from a stably stratified to an unstably stratified profile, is observed when the temperature gradient is increased. We also found, using the simultaneous full-field IR imaging and particle tracking velocimetry, that the time averaged 2D mass flux forms a closed loop, spanning the entire sample, even though neither mass field nor velocity field, individually, exhibits such a large coherent structure. The observation therefore demonstrates the subtle, but important correlations between the velocity and the mass density in convection with a vertical density gradient. These findings are new and

can have general implications for convections with strong density variations, such as ocean, atmospheric, and mantle convections.

This chapter is organized as follows. In Sec. 2.3, I first introduce the experimental methods for creating 2D freely suspended soap films in a uniform temperature gradient. The same section also contains the design of a single-point radiometer for measuring thermal radiation from a semi-transparent film. Section 2.4 is the main body, describing detection of rapid fluctuations of thermal radiations by the single-point detector and by the 2D full-field imaging system. The technique is then applied to a strongly convective soap film, demonstrating that it is feasible to measure small thermal radiation from the film. The signal-to-noise is sufficient for a meaningful calculation of the power spectrum. Mean density profiles as a function of the temperature gradient are reported in the same section. Section 2.5 provides a brief summary of the experiment. Most experimental details, such as the calibration procedures and certain calculations, are contained in Appendices A and B. The two appendices are for the sake of completeness and would be useful for those who are interested in implementing similar techniques in their own experiments.

## **2.3. Experimental Methods**

### **2.3.1. Thermal Convection Setup**

A schematic drawing of the experimental setup is shown in Figure 2-1. Here two anodized aluminum blocks are used to stabilize the thermal gradient. The temperature  $T_{\text{bottom}}$  (the lower block) and  $T_{\text{top}}$  (the upper block) are controlled independently by two Tronac temperature controllers with a long-term stability better than 10 mK. The two aluminum blocks are separated by an adjustable gap in which a freely suspended film is drawn from a reservoir imbedded in the lower aluminum block. Main ingredients of soap solution are 2% (by weight) detergent (Dawn) and 98% of water. To facilitate velocity measurements using LDV and PIV, small colloidal particles are seeded into the soap solution. The addition of these particles is known to have little effect on fluid flows in the film. A thin stainless steel frame (50  $\mu\text{m}$  thick) with a square (2x2  $\text{cm}^2$ ) cut in the center is used to initiate the film. When the frame is lowered into the soap solution reservoir and raised slowly, a film forms naturally and can last for a long time.

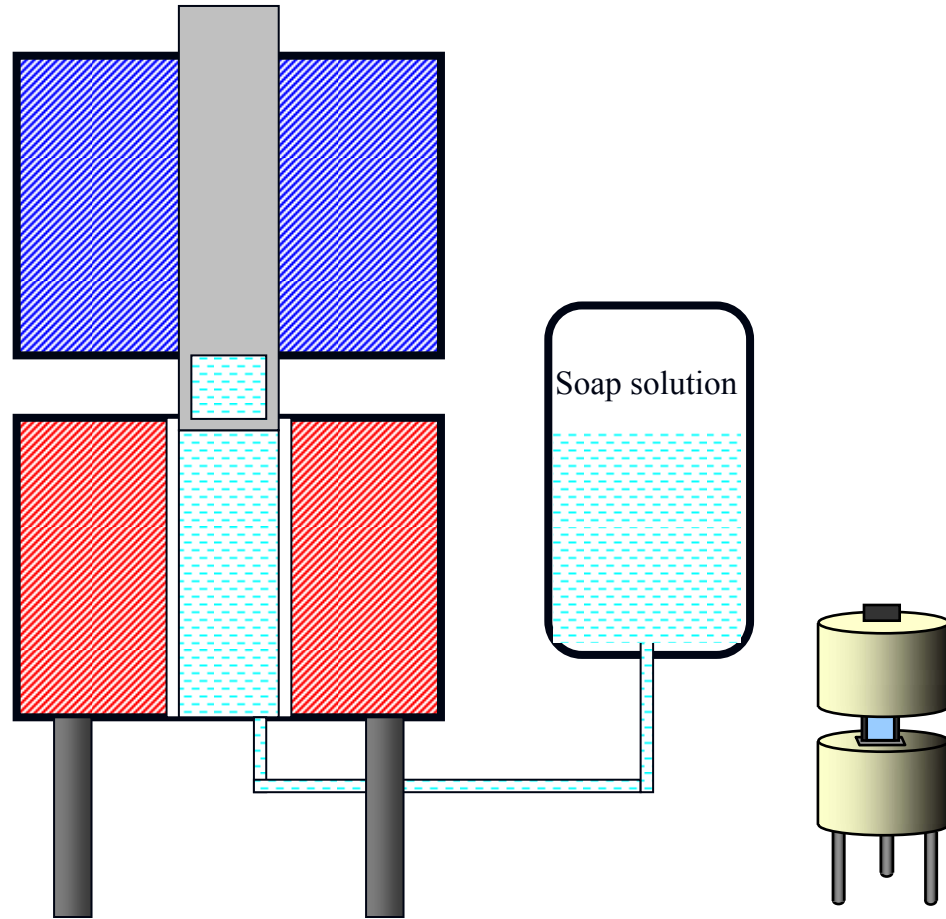


Figure 2-1: Experimental Setup. The experimental setup consists of a thermal convection cell, which is made of two large aluminum cylinders stacked on top of each other. Each measures 10 cm in diameter and height. The lower cylinder is heated by stick-on Minco heaters and the upper one is cooled by four solid-state coolers. Separation of the two blocks can be adjusted so that films of different heights can be formed. Inside the lower cylinder is a slim stainless steel vessel, which serves as a reservoir of soap solution and is connected to an external soap-solution bottle. The height of the soap solution surface level inside the vessel can be adjusted. A thin stainless steel frame, 50  $\mu\text{m}$  thick, is used to draw the film from the reservoir. For this experiment, the size of the film was fixed at  $2 \times 2 \text{ cm}^2$ . For the thermal radiation measurement, the imaging optics was set up such that a single point in the film was directly mapped onto a light detector using 2f-2f geometry. In order to reduce noises, the incoming radiation signal was modulated by an optical chopper, amplified first by a pre-amplifier and then by a lock-in amplifier. A HeNe laser was used to aid the alignment of optics. The right corner shows a 3D plot of the set up.

### 2.3.2. Flow patterns

To appreciate what we attempted to investigate, it is useful to review flow patterns observed in the film. Figure 2-2 shows typical flows when the temperature gradients ( $\Delta T/H$ ) are respectively  $\Delta T=31$  K (a) and  $\Delta T= 62$  K (b), with the upper temperature  $T_{\text{top}}$  fixed at  $14$  °C. Here  $H=2\text{cm}$  is the film height. Standard shadowgraph techniques [29] are used. Images are taken with a normal CCD camera. As can be seen, for the small temperature gradient (a), the dominant flow structures are thermal plumes that are emitted stochastically from the lower boundary, driving fluid flow in the lower part of the film. The emission of thermal plumes from the film top is much less frequent. The asymmetric plume emission shows that our system is intrinsically different from the classical paradigm of Rayleigh-Bénard convection, where plume emission is more or less symmetric at top and bottom [30-33]. This observation implies that when  $\Delta T$  is not large, density stratification plays an important dynamic role in our system [17, 34] and potential energy overwhelms the kinetic energy of the thermal plumes. For large temperature differences ( $\Delta T \geq 48 \pm 3$  K), thermal plumes gain considerably more kinetic energy, allowing them to readily reach the top of the film. In this so-called kinetic energy dominated regime (b), one observes that vigorous convection takes place throughout the entire film and a large-scale circulation often forms and switches directions in a chaotic fashion. Despite the small system used, typical fluctuations in the flow velocity are rather high;  $v_{\text{rms}} \sim 3$  cm/s, which is much larger than in normal 3D systems [35]. Large velocity fluctuations in the film give the appearance of strong turbulence as seen in the pictures.

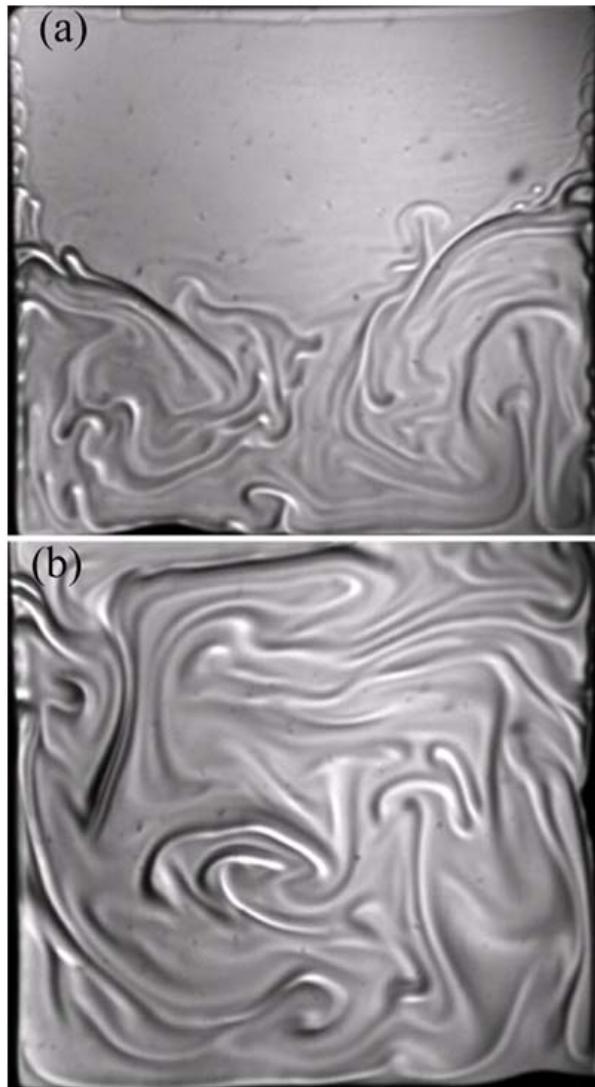


Figure 2-2: Shadowgraphs of Thermal Convection Patterns in Soap Films. The images were taken by a CCD camera with a shutter speed of 1 ms. The height and width of the film were respectively 2 by 2 cm. (a) The shadowgraphs were taken at a  $\Delta T=31$  K (a) and a  $\Delta T=62$  K (b). In both cases, thermal plumes of various sizes are clearly discernible. However, for a low temperature gradient case (a), plumes can only climb half way up the film, leaving the top half essentially quiescent. One can occasionally observe, as shown in (a) that a hot plume ascends from the lower thick film region into the upper thin film region, or the secondary emission. This type of plumes is not as energetic as the ones directly ejected from the bottom of the cell. In the presence of a large temperature difference (b), plumes can readily reach to the top of the film, causing vigorous mixing throughout the entire film.

### 2.3.3. Thermal Radiation from Semi-transparent Films and Its Measurement

Reliable temperature and thickness measurements in a freely suspended liquid film are not trivial. This is partly due to small film thickness and partly due to fluid motions in the film. For temperature measurements as an example, the small film thickness contributes to a small thermal mass, which can be easily perturbed by a conventional contact thermometer, making the measurement inaccurate. Similarly, fluid wetting on temperature sensor could also significantly distort planar geometry of a film, obstructing fluid flows. We note that a typical freely suspended film used in our experiment has thickness at least 10 times smaller than the smallest thermistor ( $\sim 100 \mu\text{m}$  in diameter) or thermocouple ( $\sim 50 \mu\text{m}$  in diameter) commercially available. To study convection in film, therefore, it is highly desirable if a noninvasive and fast-response probe can be built in laboratory.

We have designed and tested an infrared (IR) radiometer, which allows us to measure rapid fluctuations in thermal radiation signal from a small spot on the film. The technique is deeply rooted in the fundamental physics of blackbody radiation, which historically played an important role in the discovery of quantum physics [36]. For an ideal blackbody, the mathematical description of energy distribution follows the Planck equation:

$$I_{\lambda}^0 = \frac{2\pi hc^2 \lambda^{-5}}{e^{hc/\lambda k_B T} - 1}, \quad (2.1)$$

where  $I_{\lambda}^0$  is the thermal radiation energy at a given wavelength  $\lambda$ ,  $k_B T$  is the thermal energy,  $c$  is the speed of light in vacuum, and  $h(=6.6262 \times 10^{-34} \text{ J}\cdot\text{s})$  is the Planck constant. From Eq. (2.1), it follows that maximum energy emission takes place at a wavelength  $\lambda_0 = \frac{2.898 \times 10^{-3} \text{ K}\cdot\text{m}}{T}$ , for a given temperature  $T$ . For a typical temperature used in our experiment,  $60 \text{ }^\circ\text{C}$ , the maximum emission occurs at  $\lambda_0 = 8.7 \mu\text{m}$ . The total radiation energy is given by the summation of all wavelengths in Eq. (2.1), and it obeys the Stefan-Boltzmann equation  $I = \int I_{\lambda} d\lambda = \sigma T^4$ , where  $\sigma = 5.67 \times 10^{-8} \text{ J/s}\cdot\text{m}^2\cdot\text{K}^4$  is a universal constant. This relation holds only for an ideal blackbody radiation. For an arbitrary object, its radiation ability depends on the transparency of the body as well as its surface condition. The Stefan-Boltzmann equation for a non-ideal radiator is given by

$I = \varepsilon \sigma T^4$ , where  $\varepsilon$  is the thermal emissivity and can be determined by the Kirchoff's law:  $\varepsilon + r + t = 1$ . Here  $r$  is the reflectivity of the surface and  $t$  is the transmittance. If the body is opaque with  $t = 0$ , the surface reflectivity alone determines the thermal emissivity with the result  $\varepsilon + r = 1$ . In our liquid thin films with a finite thickness  $h$ , the transmittance  $t$  cannot be negligible. However,  $\varepsilon$  can still be determined based on the generalized Fresnel's law of reflection, which takes into account the light absorption property of a material. Using the schematics in Fig. 2-3 and assuming a single absorption length  $Z_0 = Z_0(\lambda_0)$ , the reflectivity and the transmittance can be calculated with the result:

$$t = \frac{I_t}{I_0} = \frac{(1-R)^2 e^{-h/z_0}}{1 - R^2 e^{-2h/z_0}}, \quad (2.2)$$

$$r = \frac{I_r}{I_0} = R \frac{1 + (1-2R)e^{-2h/z_0}}{1 - R^2 e^{-2h/z_0}}, \quad (2.3)$$

$$\varepsilon = 1 - r - t = 1 - \frac{(1-R)^2 e^{-h/z_0} + R(1 + (1-2R)e^{-2h/z_0})}{1 - R^2 e^{-2h/z_0}}, \quad (2.4)$$

where  $R$  is the reflectivity at water-air interface. The bulk water is an excellent radiator due to its low reflectance and high absorption in the near IR regimes. For instance, at  $\lambda \sim 2.98 \mu\text{m}$ , the attenuation length  $Z_0$  is only  $0.9 \mu\text{m}$ ; a film of a few microns in thickness is therefore opaque and all exponential terms in Eqs. (2.2-2.4) can be dropped and  $\varepsilon$  is essentially a constant, independent of  $h$ . Measurements show that thermal emissivity of bulk water is quite high with  $\varepsilon = 1 - R \sim 98\%$ , yielding  $R \sim 2\%$  over the wavelength range  $3 < \lambda < 14 \mu\text{m}$ , which is relevant to the IR detectors used in this experiment [37]. The smallness of  $R$  allows the calculation of  $\varepsilon$  for an aqueous film to be simplified. To the first order in  $R$ , we find

$$\varepsilon \approx (1-R) - (1-2R)e^{-h/z_0} - R e^{-2h/z_0}. \quad (2.5)$$

The leading thickness dependence is thus given by

$$\varepsilon \approx 1 - e^{-h/z_0}, \quad (2.6)$$

if the contribution of  $R$  is neglected. The above derivation shows that thermal radiation can be used to measure separately temperature and film thickness depending on the detection wavelength. For those wavelengths at which water absorbs strongly with  $Z_0 \ll h$ , thermal radiation is dominated by temperature fluctuations since  $\varepsilon \sim 1$ . On the opposite limit when  $Z_0 \gg h$ , this technique is sensitive to temporal fluctuations in the thermal emissivity, which can be

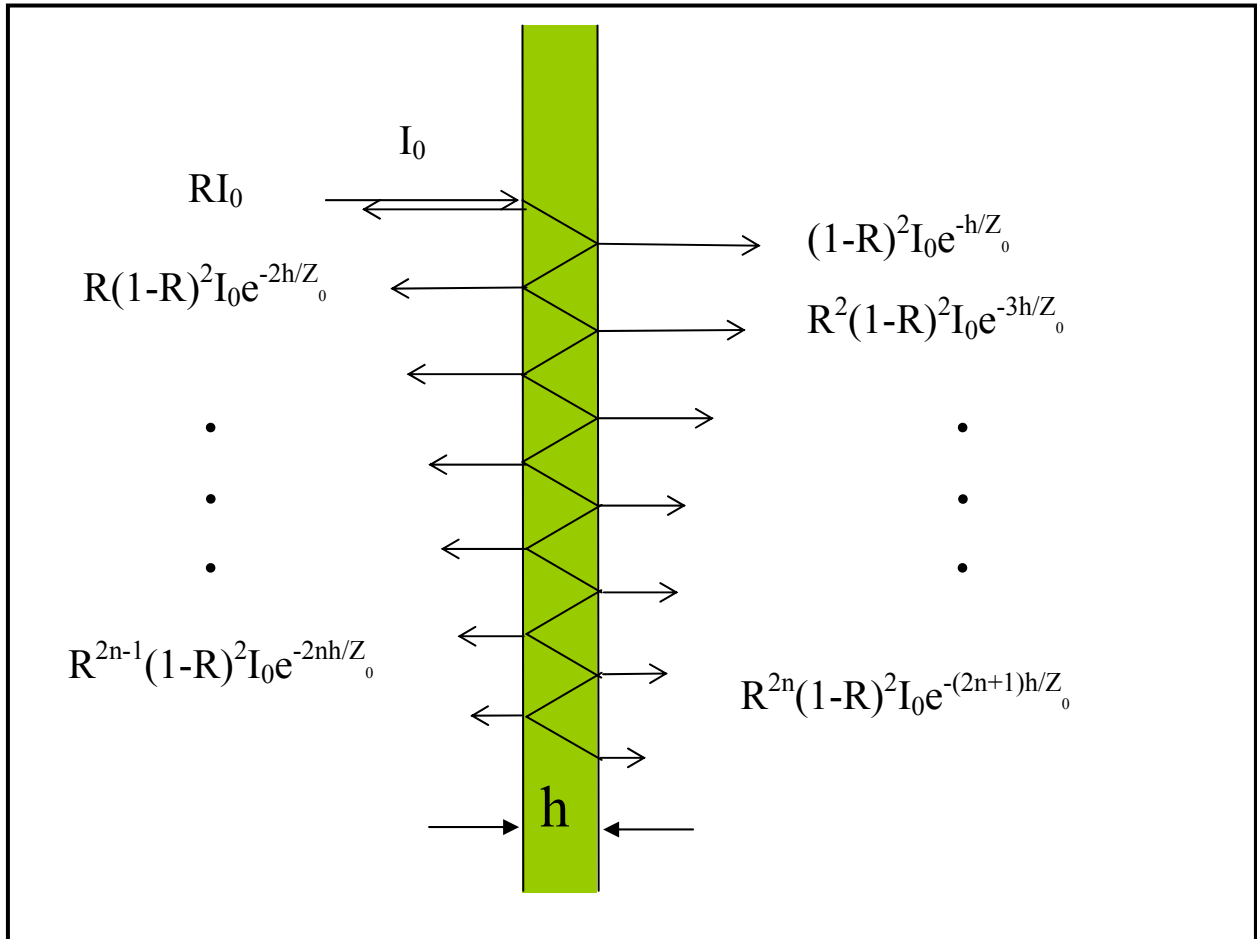


Figure 2-3: Schematics of Multiple-beam Reflection in a Film. The input light  $I_0$  is multiply reflected and attenuated due to IR light absorption. The film is assumed to have a uniform thickness  $h$  and a constant absorption length  $Z_0$ . The light reflectivity  $r$ , transmittance  $t$ , and emissivity  $\varepsilon$  are calculated based on this geometry. See text for details.

related to variations in film thickness since  $\varepsilon \sim h/Z_0$ . Thus in the thin-film limit,  $h/Z_0 \rightarrow 0$ , thermal radiation diminishes as expected.

To measure thermal radiation from the film we used a mercury-cadmium-tellurium (HgCdTe) detector from EG&G. The detector was installed in a double-window Dewar and cooled down to liquid nitrogen temperature 77K. A small spot in the center of the film,  $\sim 1$  mm size, was imaged onto the photo-detector by a ZnSe lens (II-VI, Inc). A high numerical aperture lens (f-number=0.8 with FL=2.25 cm) was used to collect the light from the film. To reduce background noises, a cold screen was placed behind the film. The screen was made of sheet copper, painted dull black, and cooled to 4 °C by a set of heat exchange coils welded to the screen. To further improve the signal-noise ratio, the incoming IR signal was mechanically chopped at a frequency of 4,000 Hz, pre-amplified, before sending to a lock-in amplifier (EG&G, Model 5209).

Systematic methods were developed to calibrate the thermal radiometer and the procedures are detailed in Appendix A. Briefly, the detector measures the difference between thermal radiations emitted from the film and those from the chopping wheel. As a demonstration of the technique, we first calibrated the radiometer against a piece of Pyrex glass, which has a thermal emissivity  $\varepsilon (\approx 0.94)$  [38] comparable to that of bulk water [37]. As shown in Fig. 2-4, as the temperature of the glass increases, the output voltage  $V$  of the lock-in amplifier increases. The plot of  $V$  vs.  $T^4$  exhibits a straight line as expected from the generalized Stephen-Boltzmann equation  $I \sim \varepsilon \sigma T^4$ . Since  $\varepsilon$  is known for the glass, the slope in Fig. 2-4 yields a direct measurement of the collecting efficiency  $\alpha = I/\varepsilon \sigma T^4$  of our optical setup. This collecting efficiency, which will be discussed in more details in Appendix A, was kept fixed throughout the measurements.

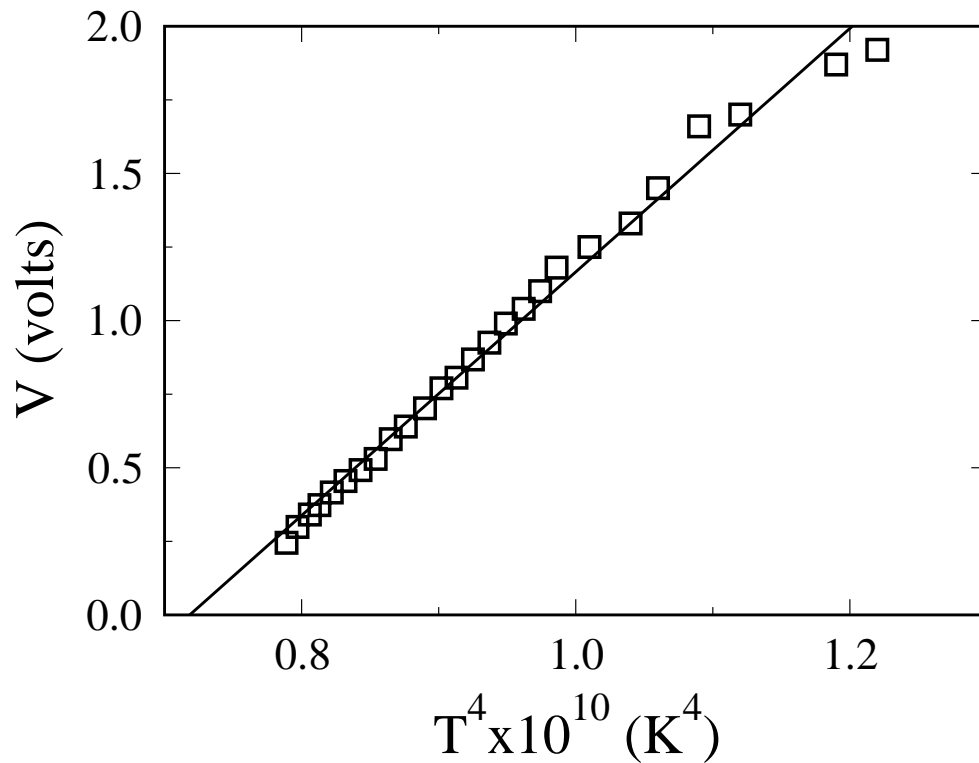


Figure 2-4: Thermal Radiation from a Thick Glass Plate. This is a calibration curve using a Pyrex glass plate. A Minco heater was attached to the back of the plate and its surface temperature was monitored by a thermister. The vertical axis is the voltage output from the lock-in amplifier. As shown in the plot the radiation signal scales linearly with  $T^4$  as expected. Using the known thermal emissivity of glass  $\epsilon=0.94$ , the sensitivity of the setup can be calculated.

## 2.4. Experimental Results

### 2.4.1. Temporal Fluctuations of Thermal Radiation in Thin Films

We next proceeded to measure thermal radiation from the freely suspended soap film. A “stationary” film stratifies so rapidly that systematic measurements become very difficult. Hence, all of our experiments in the film were conducted in the presence of a temperature gradient. Figure 2-5 is a time trace of a typical run when  $\Delta T=41$  K and the upper temperature is fixed at  $T_{\text{top}}=14$  °C. One observes that radiation power fluctuates rapidly on different time scales from tens of milliseconds to  $\sim 1$  s. The fluctuation amplitude is  $\sim 100$  mV which is significantly larger than the noise level of the lock-in output. The electronic noise is  $\sim 5$  mV in the relevant frequency range of  $0.1 < f < 10^3$  Hz. The fluctuations have no discernible structures suggesting that they are self-similar, which is a signature of spatiotemporal chaos or turbulence in the fluid.

The time trace such as this one can be used to compute the power spectrum  $\Gamma(f)$  of the radiated thermal power from the film. Figure 2-6 displays a set of three measurements carried out at three different vertical locations in the center of the cell. As can be seen, the power spectrum  $\Gamma(f)$  consists of two different regimes and is not very sensitive to the location where  $\Gamma(f)$  is measured. For small frequencies, the spectrum displays a power-law-like behavior and can be mimicked by the function  $\Gamma(f) \sim f^{1.4 \pm 0.1}$  over a limited (or about a half decade) frequency range. For large frequencies, the spectrum decays more rapidly and can be characterized by a different power-law with  $\Gamma(f) \sim f^{-4.2 \pm 0.8}$ . The solid lines in the figures are guides to the eye. To ascertain that the fluctuations measured by the detector were indeed arising from the film, the measurement was repeated using the identical setting except the film was removed. As shown by the lower curve in Fig. 2-6, even in the absence of the film, the background radiation still contributes to the signal, but the magnitude is smaller by nearly three orders of magnitude in the low frequency regime. This residual signal is due to the saturated water vapor above the soap solution reservoir in the convection cell. The weakness of this background signal is reassuring, demonstrating the sensitivity of our experiment.

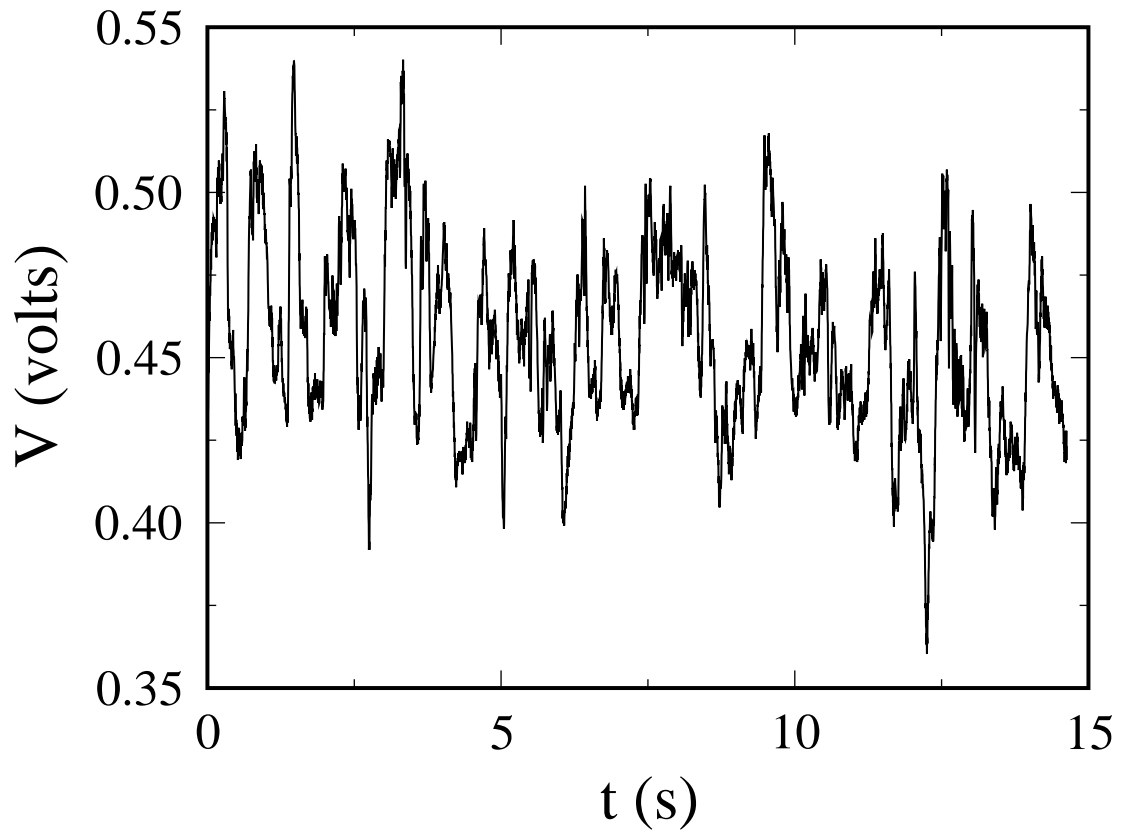


Figure 2-5: A Time Trace of Radiation Signal from a Turbulent Convection Film. The data was digitized at a rate of 1 kHz and at a 14-bit resolution. The measurement condition corresponds to  $\Delta T=55$  K and  $T_{\text{top}}=15.5$  °C fixed. The large voltage fluctuations are due to passages of thermal plumes through the detected area,  $\sim 1$  mm in diameter. The small-scale fluctuations are presumably due to fine internal structures of plumes.

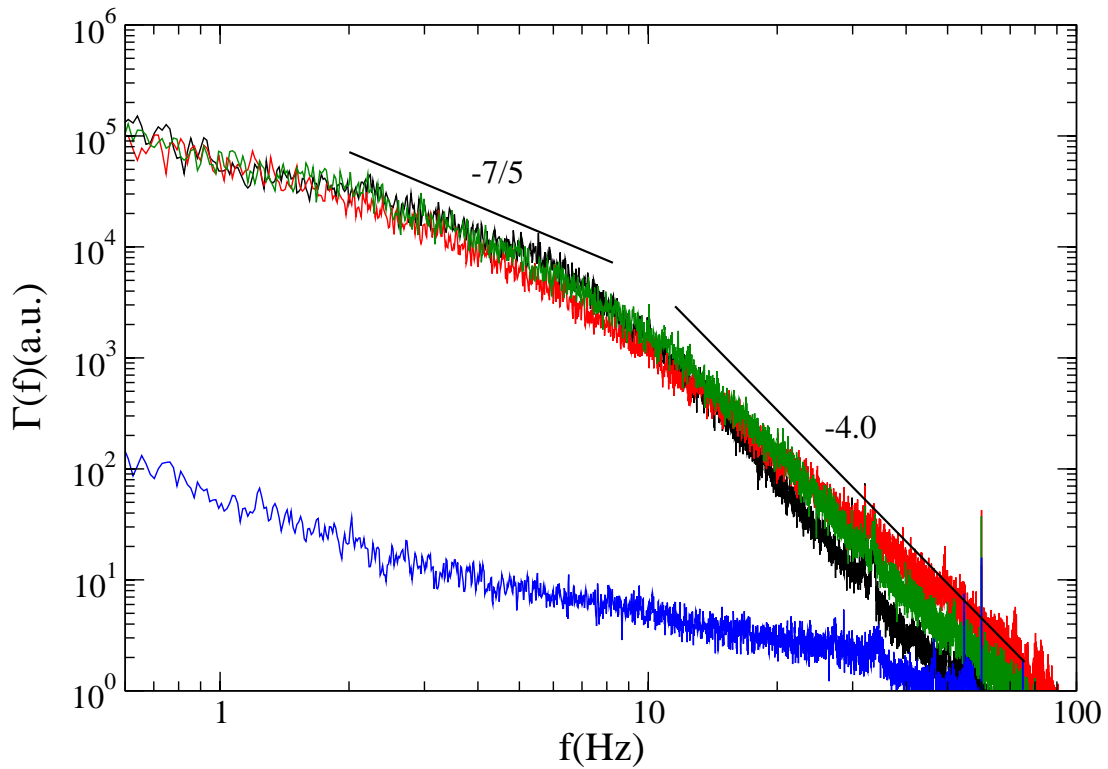


Figure 2-6: Power Spectrum of Thermal Radiation from a Turbulent Convection Film. The upper curves are measured from the film at  $y=1.3$  (black),  $1.0$  (green), and  $0.7$  cm (red), and the lower curve is the background without the film. The  $y$  is defined as  $y=0$  at the foot of film and  $y=2$  cm at the film top. The power spectrum shows two scaling regimes separated by a characteristic frequency  $f_c \sim 8$  Hz. Interestingly the scaling behavior  $\Gamma(f) \sim f^{-1.4}$  in the low-frequency regime ( $f < f_c$ ) is close to the theoretically expected ones. See text for more details.

We also explored whether different confining geometries can affect the power spectrum. In 3D convection experiments, it was found that heat transport can be significantly influenced by the topographic features of the heated (cooled) surfaces [39] and by the shape of the container [40]. However, it is unclear if the power spectrum itself is affected. In our 2D experiment, these geometric parameters are particularly easy to vary as demonstrated in Fig. 2-7, where typical convection patterns in cells with a “rough” lower boundary (a), semi-elliptical, and triangular boundaries are displayed. All these cells are constructed by milling of a thin stainless steel sheet 50  $\mu\text{m}$  in thickness and with the aspect ratio close to unity. As can be seen in the figure (d), the measured  $\Gamma(f)$  for the three geometries yield essentially the same result for small frequencies with  $\Gamma(f) \sim f^{1.4}$ , which is also seen in the square cell. The scaling behavior for high frequencies is varied even more, with the exponent ranging from 3.5 for the triangular cell to 4.4 for the semi-circular cell.

The above measurements suggest that for small frequencies  $f$ , which corresponds to large spatial scales, there is a limited range (about a half decade) where the radiation spectra follow a power law and appear to be independent of the geometrical shape of the confinement. The spectrum  $\Gamma(f) \sim f^{1.4}$  is suggestive of a Bolgiano scaling [28], but from this measurement alone it is unclear whether such scaling arises because of temperature or density fluctuations. This question would be answered by the findings in the following subsection.

#### **2.4.2. Spatial Fluctuations of the Film Thickness Determined by 2D IR Imaging**

Since only the radiation power from the film has been measured, it seems to be not entirely clear whether the fluctuations observed is due to the film thickness or to temperature variations. Recall that the generalized Stephen-Boltzmann relation for a soap film is proportional to the product of  $\varepsilon$  and  $T^4$ , where  $\varepsilon$  is a function of the thickness  $h$  via Eq. (2.6). In order to answer this question, direct thickness measurements were made using an IR camera (Inframetrics, Model 600 L). The camera uses the same light-sensing element (HgCdTe) as our home-built detector, and thus has the same spectrum range in the IR regime. To form an image, the camera’s internal mirror scans line-by-line, forming images at a rate of 30 fps.

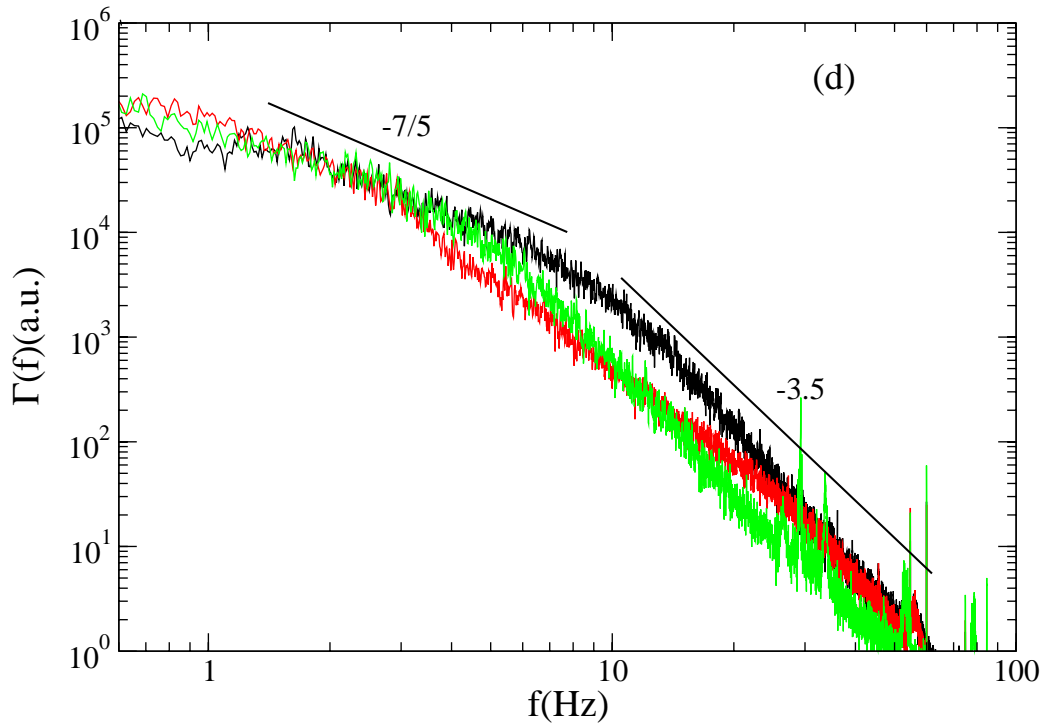
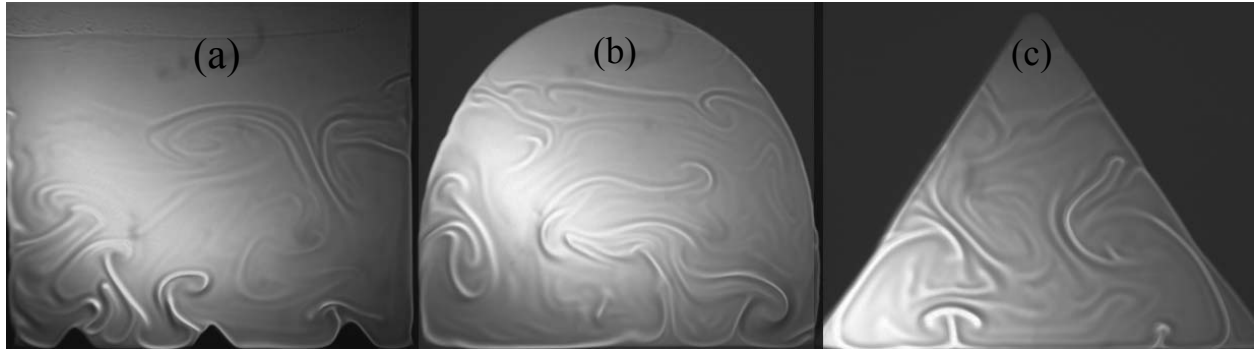


Figure 2-7: Thermal Convection in Different Geometries (a) A “rough” lower boundary, (b) a semi-elliptical boundary, and (c) a triangular boundary. The temperature difference  $\Delta T=41$  K. Though thermal plumes are more likely to be emitted from the “rough” boundary, the measured power spectra, for the rough cell (green), the semi-elliptical cell (black), and triangular cell (red), are nonetheless similar as delineated in (d).

Each IR image consists of H256xV200 equivalent pixels and has 8-bit resolution. Because water absorbs IR strongly, a transmission geometry is adopted in the measurement where Lambert-Bear law can be used to find  $h(=Z_0 \ln(I_0/I))$  [25]. Here  $I/I_0$  is the normalized transmittance and  $Z_0$  is the effective absorption length. For the given spectral width of the camera, a calculation, in Appendix B, shows that  $Z_0=7.83 \mu\text{m}$ .

In the transmission measurement, the cold screen was replaced by a blackened hot plate, uniformly heated to 350 °C. The single-point detector was replaced by the IR camera. In the absence of the film, the camera's sensitivity was adjusted such that each pixel was nearly saturated. Because the plate was a good radiator with  $\epsilon \sim 1$  and sufficiently hot compared to the film and its surroundings, in the absence of the plate, the pixel readings are uniformly zero for the given sensitivity setting. The gray scale of each pixel  $I(x,y)$  normalized by its corresponding reading without the film  $I_0(x,y)$  thus yields the transmittance of the film  $t(x,y)=I(x,y)/I_0(x,y)$  at each point. Three sets of measurements at three different temperature gradients,  $\Delta T= 37, 49.5,$  and  $61.5 \text{ K}$ , were carried out. For each temperature difference,  $10^3$  images were collected at a time interval of 2 fps with the exposure time of 33 ms. The large time interval between the pictures ensures that thermal images are statistically independent, allowing ensemble averages for the mean thickness  $\langle h(x,y) \rangle$  and its standard deviation  $\langle \delta h(x,y)^2 \rangle^{1/2}$  to be calculated.

Figure 2-8(a) is a typical snapshot of a thickness map converted from the transmission image according to the formula  $h(x,y)=Z_0 \ln(I_0(x,y)/I(x,y))$ . Because the picture was taken at a relatively large temperature gradient,  $\Delta T=61.5 \text{ K}$ , a large-scale circulation was present. In the picture, one observes a hot plume shooting out near the sidewall instead of from the lower boundary, suggesting the presence of a clockwise circulation. The instantaneous thickness of the plume,  $h \sim 5 \mu\text{m}$ , is considerably larger than the background thickness of  $\sim 3 \mu\text{m}$ . As can also be seen from this instantaneous thickness map, the background  $h$  is not uniform, consisting of many granular structures. This suggests that  $h$  undulates on small scales, which is a signature of strong turbulence. Figure 2-9 is a horizontal cut along  $y=1.2 \text{ cm}$ . The mean thickness has been subtracted from the measurement, and the data therefore represents the thickness variations  $\Delta h$  along the horizontal line.

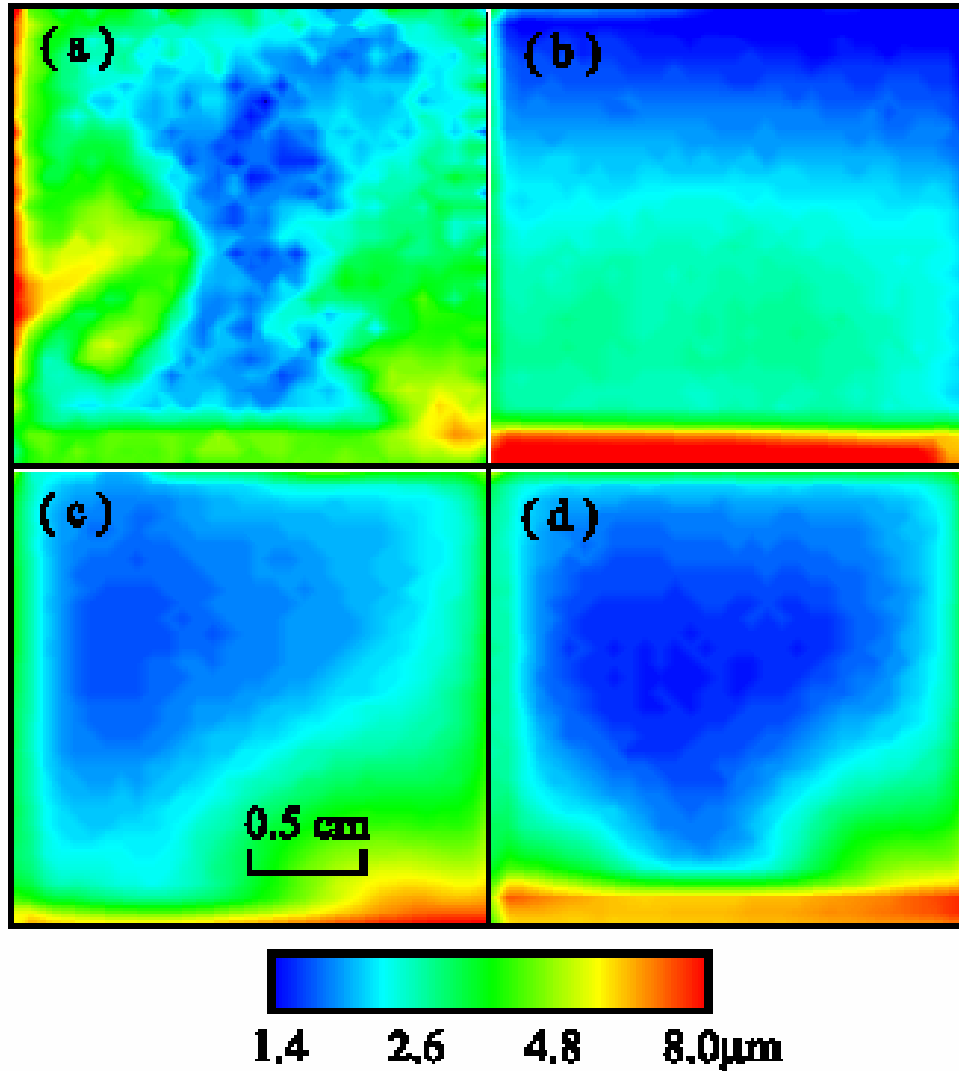


Figure 2-8: Thickness Map Measured by an IR Transmission Technique. (a) An instantaneous thickness at a  $\Delta T=61.5$  K and with  $T_{\text{top}}=14$  °C fixed. The presence of a large-scale circulation, in this case clockwise, makes the thermal plumes to be generated near the side boundary of the cell. One also observes small granular structures in the background, suggesting film thickness undulates on those scales. (b-d) Time averaged thickness maps obtained at  $\Delta T=37$  K (b), 49.5 K (c), and 61.5 K (d), respectively. For a low  $\Delta T=37$  K (b), thermal plumes are predominantly generated from the bottom, as a result, the thickness stratifies uniformly in the vertical direction. For a  $\Delta T\sim 49.5$  K (c), some plumes gain sufficient energy to climb the film's top. Convection takes place in entire film. However, this flow is a peculiar one in that the emission of thermal plums is not symmetric. As picture (c) shows, plumes emit mostly from the lower right corner, breaking the left-right symmetry (LRS) of the system. For a large  $\Delta T=61.5$  K (d), large scale-circulation causes film to be thick near boundaries and thin in the center. The LRS is nearly recovered.

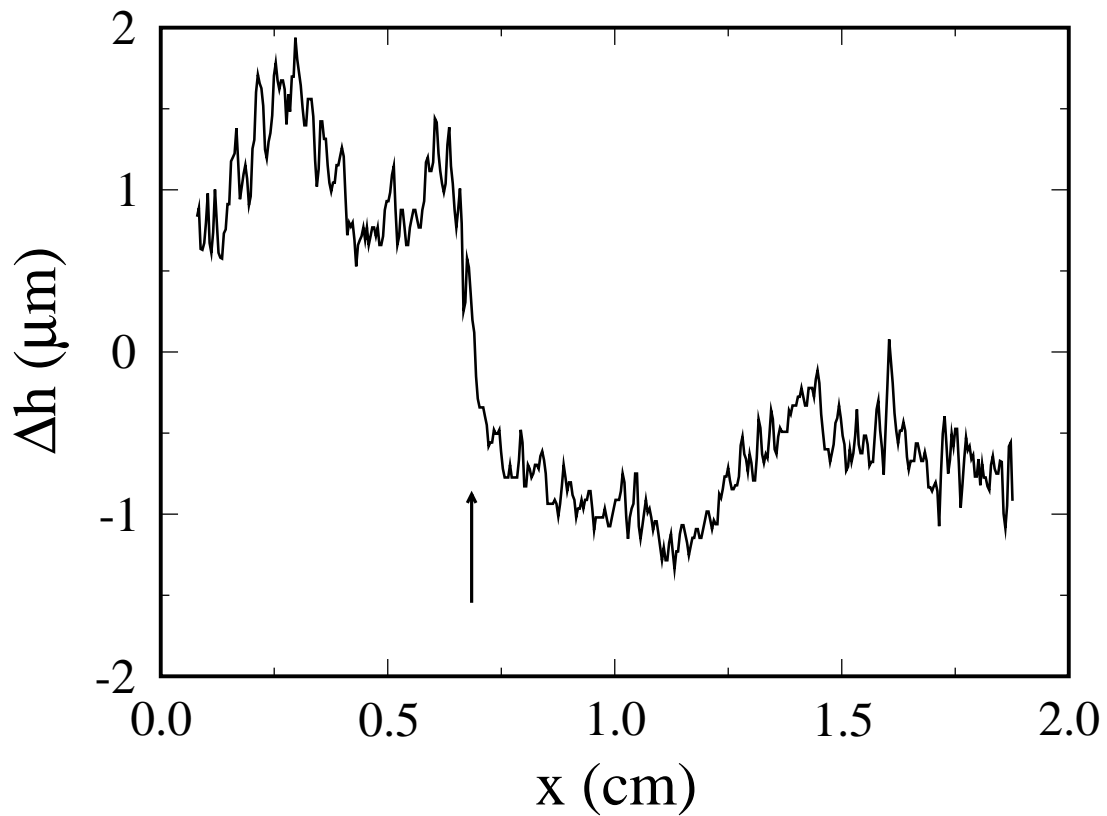


Figure 2-9: Instantaneous Thickness Variations  $\Delta h$  Along a Center Horizontal Line of a Turbulent Convection Soap Film. This curve represents the thickness distribution along the vertical height,  $y=1.2$  cm, of the film shown in Fig. 2-8(a). Here the mean thickness was subtracted. One observes that the thickness varies on large and small scales. Thermal plumes give most significant contributions to the thickness variations. A sharp cliff, indicated by the arrow, can also be observed in the above figure.

Here the fine structures can be seen more clearly, and the interface between the plume and the background shows a sharp drop (or a cliff) as commonly seen in scalar turbulence with a large Schmidt number [41]. The Schmidt number is defined as the ratio between the kinematic viscosity and the mass transfer diffusion coefficient of a scalar.

A sequence of pictures such as Fig. 2-8(a) can be averaged, and the results are presented in Fig. 2-8(b-d). For a low  $\Delta T=37$  K, the average film thickness is uniformly stratified, thick near the bottom and thin near the top as evident in Fig. 2-8(b). There are only small variations in  $h$  along the horizontal direction, as one would expect by the symmetry of the system. Direct visual observations showed that at this low  $\Delta T$ , thermal plumes are predominantly ejected from the bottom and they are not energetic enough to reach the top of the film. The upper portion of the film therefore is relatively quiescent with only occasional incursions by a few powerful plumes. Thermal plumes carry heat, fluid mass, and kinetic energy, and efficiently stir up the lower part of film, making the average thickness in the lower region larger than the average thickness of the whole film. When  $\Delta T$  increases, the plumes become more and more energetic, and are able to ascend to a greater height. As a consequence, the lower, thick-film region expands with  $\Delta T$ . When a significant number of hot plumes are able to reach the top of the film, the dynamics of the system changes significantly; the film appears to lose its global balance, in the sense that the fluid motion tends to turnover, forming a large-scale circulation. However, near the threshold of the instability, the fluid motion lacks the energy to sustain circulation on such a large scale and the motion is intermittent. Another interesting feature near the onset is that thermal plumes tend to accumulate at one of the lower corners of the convection cell, forming jets near that part of the side boundary. The system is very susceptible to perturbations or small imperfections in the setup, and the left-right symmetry of the system can be easily broken. For instance, it was observed that a tiny air bubble trapped near the corner of the cell was sufficient to bias the flow, causing plumes and jets to eject near that side of the convection cell. Figure 2-8(c) shows the flow near the threshold ( $\Delta T_c \approx 48$  K), where plumes are predominantly generated near the right boundary. Unlike the low  $\Delta T$  case presented in Fig. 2-8(b), here the thickness profile shows variations in both the horizontal and vertical directions. When an even larger temperature difference was imposed, large-scale circulations were created in the cell. The flow chaotically switches circulation directions from clockwise to counterclockwise and vice versa, and the left-

right symmetry is partially restored. This type of large-scale circulations (LSC) was first reported by Krishnamurti and Howard [42] and has been subsequently observed in many 3D experiments [31, 40, 43-45]. However, the physics behind this fascinating phenomenon still remains to be explained. Unlike 3D convection experiments, the period of persistent circulation in the film is somewhat shorter, about a few seconds, instead of many minutes to hours [44, 46]. Figure 2-8(d) shows the thickness profile when  $\Delta T=61.5$  K. As can be seen, the thickness distribution is very different from those observed when the temperature gradient is low;  $h$  appears to be quite uniform near the center and most thickness gradient appears near film boundaries, resulting from LSC.

To further quantify our measurements; in Fig. 2-10, the thickness profile  $h(y)$  (squares) and its standard deviation  $\delta h(y)$  (circles) along the central vertical axis of the film are presented. Data are plotted for two extreme temperature differences  $\Delta T=37$  K and  $\Delta T=61.5$  K, corresponding to (b) and (d) of Fig. 2-8. In both cases, one observes that near the foot of the film,  $y \sim 0$ , the thickness is very large with  $h/Z_0$  close to unity. However  $h$  decreases rapidly over a vertical height of a few millimeters. For a small  $\Delta T=37$  K, the stratification above the foot is stable ( $dh/dy < 0$ ); i.e. the thickness decreases with  $y$  as shown in (a). On the other hand, for a large  $\Delta T=61.5$  K, the stratification above the foot is unstable ( $dh/dy > 0$ ) with a small but discernible inverted thickness gradient as shown in (b). We also noticed that overall, the film thickness in the middle of the convection cell decreases as  $\Delta T$  increases. Thus the onset of the LSC has the remarkable effect of not only homogenizing the mass distribution along the vertical axis but also redistributing the mass so that the density profile switches from stable to unstable configurations. Quantitatively, we found that  $h/Z_0$  is about 20-40% and  $\delta h/Z_0$  is about 10% in different temperature gradients. In particular, the standard deviation of the thickness  $\delta h/Z_0$  turns out to be only weakly dependent on  $\Delta T$  as shown by the squares in Fig. 2-10(a-b). For  $Z_0=7.83$   $\mu\text{m}$ , the average film thickness in the flowing soap film is  $h \sim 2.2$   $\mu\text{m}$  and  $\delta h \sim 0.8$   $\mu\text{m}$ . It is reassuring that the measured thickness is in reasonably good agreement with that determined by the single-point radiometry measurement, where the averaged thermal emissivity was found to be  $\varepsilon_f \approx 0.185$ , yielding  $h \approx 1.7$   $\mu\text{m}$ . As shown in Appendix A, the small ratio  $h/Z_0$  causes the

thermal emissivity of the film to fluctuate and is the dominant source of temporal fluctuations in the radiation signal.

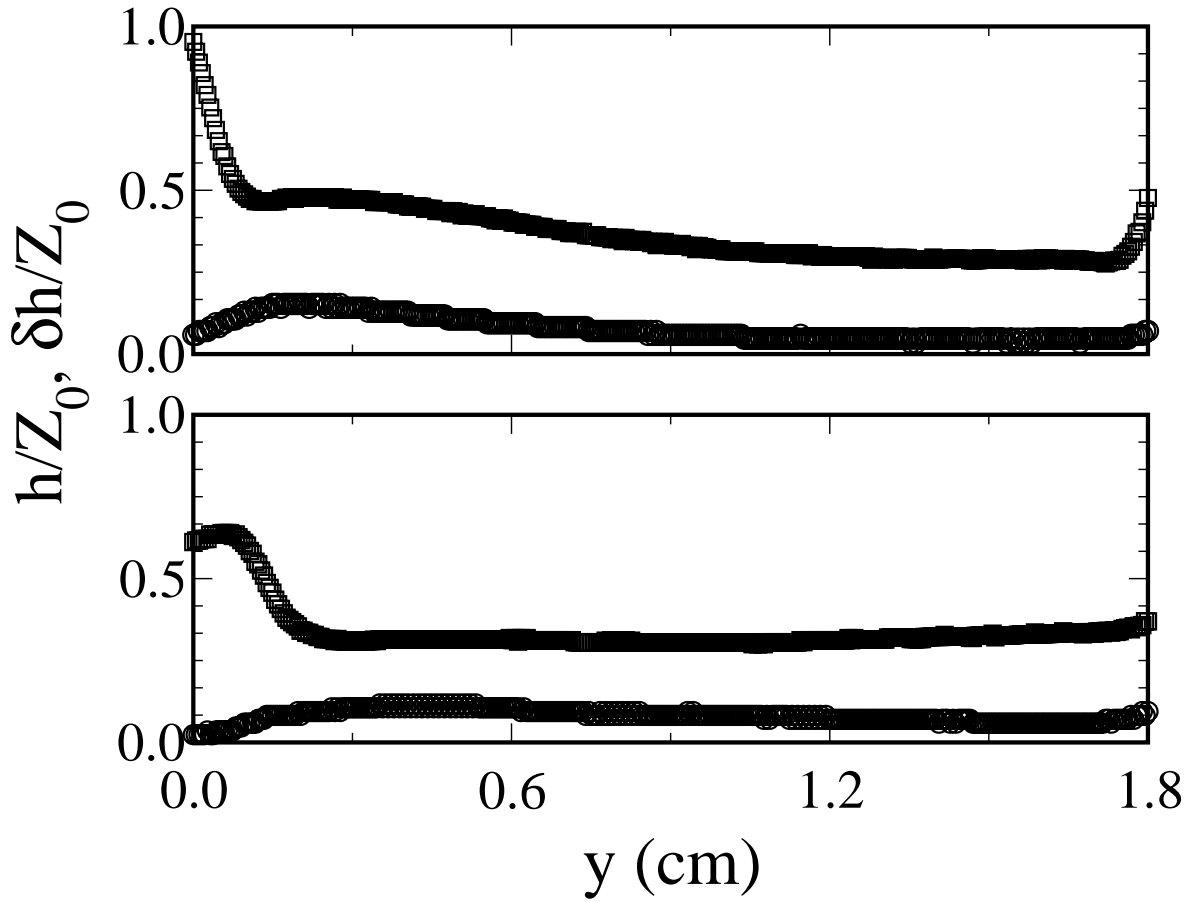


Figure 2-10: The Vertical Mean Thickness Profile  $h(y)$  and the Standard Deviation  $\delta h(y)$ . Both measurements were made along the central vertical axis of the film using the thickness maps presented in Fig. 2-8(b) and 2-8(d). The top figure (a) corresponds to a  $\Delta T=37$  K and the bottom figure (b) corresponds to a  $\Delta T=61.5$  K. In both figures, the average film thickness  $h$  is represented by the squares and the standard deviation  $\delta h$  is represented by circles. The horizontal axis is the vertical height  $y$  of the film.

### 2.4.3. Statistics and Scaling Relations of 2D Density Fluctuation

Returning to the single-point measurement, the physics underlying the power spectra observed in Fig. 2-6 and Fig. 2-7(d) now become clear. What we have observed are essentially the 2D density fluctuations of the film. In year 1950s, Bolgiano postulated that convective turbulence in a stably stratified fluid, such as in the earth's atmosphere or in oceans, shall behave very differently from barotropic turbulence in homogeneous media [27, 28]. The difference stems from the fact that there is constant "tradeoff" of kinetic energy and gravitational potential energy such that the kinetic energy flux  $\varepsilon$  at large scales is no longer a constant but depends on the measurement length scale  $l$ . The situation is in contrast with barotropic turbulence where  $\varepsilon$  does no dependent on  $l$  in the inertial range and the Kolmogorov 5/3-law follows [47].

It is straightforward to generalize Bolgiano's scaling argument to convection in soap films. Since the time rate of change of 2D density ( $\rho_2 = \rho h$ ) fluctuations is a constant of motion, i.e.,  $\chi_\rho = d\langle \delta\rho_2^2 \rangle / dt = \text{const}$ , it follows that

$$\langle \delta\rho_{2l}^2 \rangle \sim \chi_\rho l / v_l, \quad (2.7)$$

where  $\rho_{2l}$  and  $v_l$  are respectively the 2D density and velocity variations on scales  $l$ . Assuming that potential energy and kinetic energy are balanced on the scale  $l$  ( $\frac{1}{2}\rho_2 v_l^2 = \delta\rho_{2l} g l$ ), one finds  $v_l \sim (2\delta\rho_{2l} g l / \rho_2)^{1/2}$ . Replacing  $v_l$  in Eq. (2.7), one finally arrives at the scaling relation for the structural function of  $\delta\rho_{2l}$ ,

$$\langle \delta\rho_{2l}^2 \rangle \sim \chi_\rho^{4/5} (g/\rho_2)^{-2/5} l^{2/5}. \quad (2.8)$$

In momentum space, the corresponding relationship is the power spectrum that scales as  $\Gamma(k) \sim k^{-7/5}$  [28]. Here the wavenumber  $k$  and the scale  $l$  are related by  $k \equiv 2\pi/l$ . The predicted scaling for  $\Gamma(k)$  is nearly identical to what we have observed  $f^{-1.4 \pm 0.1}$  for different cell geometries in Fig. 2-6 and Fig. 2-7, except that the measurements were carried out in frequency space whereas the

calculation is presented in momentum space. However, such a difference can be reconciled if one takes the view that small-scale fluctuations are convected by large-scale ones with the result  $f \sim v_{\text{rms}}/l$  [48]. On a more fundamental level, the same scaling relation in the frequency domain (our measurements) and in the wavenumber domain (theory) may be expected and is a result of Kolmogorov's refined similarity hypothesis (K62) [49] to the scalar field. The K62, originally formulated for velocity field, postulates that if one measures the longitudinal velocity difference  $\delta v_l$  on scale of  $l$  and simultaneously measures (coarse-grained) energy dissipation  $\varepsilon_l$  on the same scale, one can form a new random variable  $V(1,0,0,0) \equiv \delta v_l / (l \varepsilon_l)^{1/3}$  such that the probability density function  $P(V)$  is *only a function* of locally defined Reynolds numbers  $Re_l = l \delta v_l / \nu$ , where the four indices of  $V$  stands for one longitudinal, two transverse components of velocity, and the time. It was further conjectured that  $V$  and  $\varepsilon_l$  are statistically independent and for  $Re_l \gg 1$ ,  $P(V)$  becomes independent of  $Re_l$  and is a universal function. As we can see, though the K62 did not make any statement about the form of  $P(V)$ , it did not exclude the possibility of using the time difference  $\delta t$  for forming the random variable  $V(0,0,0,1)$  and the pdf would be universal and independent of whether  $V$  is calculated based on distance or time. For the velocity field, K62 was reasonably well supported in fully developed 3D turbulence [50]. It seems plausible that the idea of K62 could be generalized to a scalar quantity and the statistical distribution of the quantity would be independent of whether it is measured in space or in time. However, to our knowledge, this has not been rigorously tested.

The two spectral ranges observed in the experiment allow us to define the crossover frequency  $f_C$ , which for this experiment is  $\sim 7$  Hz. Using the simple relation  $l_C \sim v_{\text{rms}}/f_C$  and the measured  $v_{\text{rms}} \sim 3$  cm/s, the crossover length turns out to be  $\sim 0.4$  cm. This length scale is comparable to the plume size in the middle of the cell and can be also associated as the Bolgiano's length scale  $l_B$ , which is the scale where the gravitational energy and the kinetic energy are approximately balanced [28].

While the  $k^{-1.4}$  scaling for the low-frequency regime was found to be robust, the corresponding scaling relation for the high-frequency regime is less reliable. Variations from  $k^{-3}$  to  $k^{-4.5}$  were observed in a range of temperature gradients,  $20 < \Delta T < 47$  K. There have been intense debates on what should be the proper scaling laws for length scales  $l (= 2\pi/k)$  less than the

Bolgiano length  $l_B$  but larger than the Kolmogorov energy dissipation scales  $l_D$ ,  $l_B < l < l_D$ , namely within the classical Kolmogorov's inertial range. Bolgiano's theoretical analysis suggested that for  $l < l_B$ , the density behaves like a passive scalar as such that  $\Gamma(k) \sim k^{-5/3}$ . Our measurement in the high-frequency regime clearly violates this scaling law. In a somewhat different derivation, Wheelon [51] and Villar and Weisskopf [52] assumed that density fluctuations are created by the turbulent velocity itself instead of "feeding" by the large-scale gradient, and found  $\Gamma(k) \sim k^{-3}$ . This scaling exponent is still smaller than but is closer to our measured value  $3.7 \pm 0.8$ . Based on the experimental observations, it is also possible that the high-frequency spectrum may be influenced by the plume structures as well as their emission statistics. In this case, new physics related to plumes, rather than the large-scale density gradient, are required in order to account for our observations.

It is clear from the above measurements that strong density variations in space and time are a hallmark of convection in freely suspended soap films. Thus by all measures,  $\delta\rho_2$  is an active scalar that couples strongly to the velocity field. However, certain statistical aspects of  $\delta\rho_2$  were found to be remarkably similar to a passive scalar such as a dye in a turbulent fluid. For instance, we can use the time trace from the single-point detector, such as the one in Fig. 2-5, to construct the probability density function (pdf) for the 2D density difference  $\delta\rho_2(\tau)$ , where  $\tau$  is the temporal separation between two points in the time trace of  $\rho_2$ . It is understood that the temporal separation is related to the spatial separation by  $l \approx v_{\text{rms}}\tau$ . As demonstrated in Fig. 2-11(a),  $P(\delta\rho_2(\tau))$  exhibits two remarkably different behaviors depending on the time scale  $\tau$ . For a small  $\tau$ , the pdf has the typical triangular shape on this semi-logarithmic plot, indicating that the wings of the pdf are exponential. On the other hand, for a large  $\tau$ , the pdf is, to a good approximation, a Gaussian function. We also noticed that for  $\tau > 0.4$  s, all the pdfs become identical, indicating that the density fluctuations have reached an outer scale, which we determined to be  $l_0 \sim v_{\text{rms}} * \tau \sim 1$  cm. The scale  $l_0$  can be identified as the largest eddy in the flow and is about half the size of the soap film for the given  $\Delta T$ .

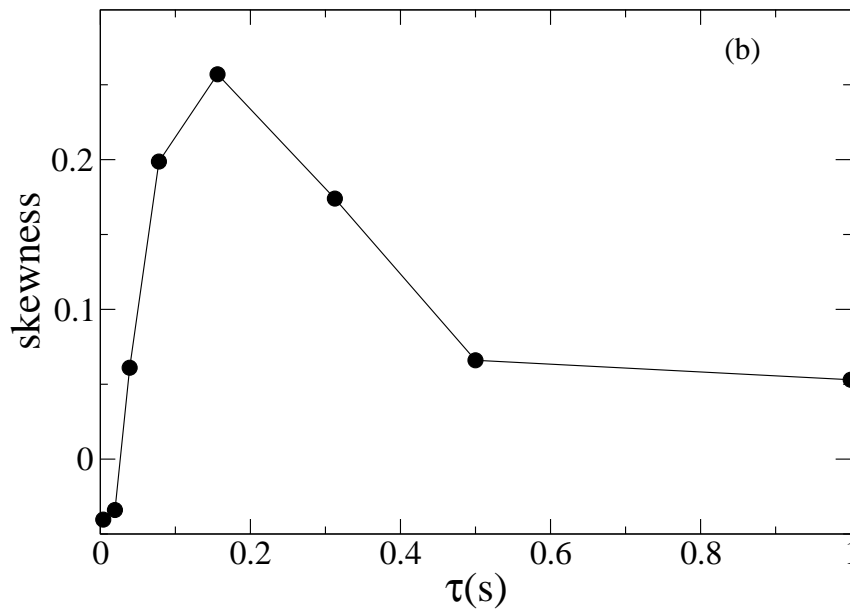
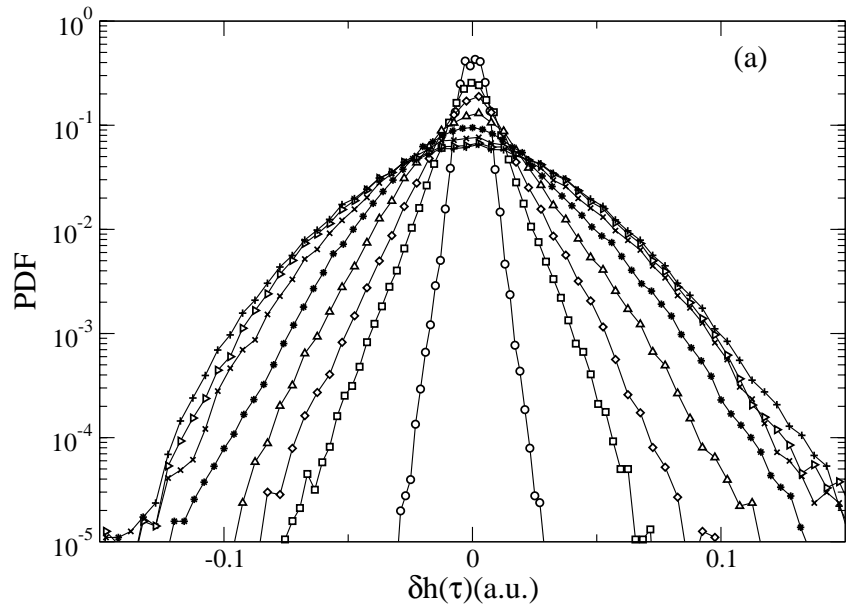


Figure 2-11: Probability Density Function of the Film Thickness Variations. (a) Different symbols correspond to  $\tau=1/256$  (open circles),  $5/256$  (open squares),  $10/256$  (diamonds),  $20/256$  (triangles),  $40/256$  (asterisks),  $80/256$  (crosses),  $0.5$  (tilted triangles), and  $1.0$  s (pluses). (b) The skewness as a function of  $\tau$ . We noted that the skewness is significantly greater in the range  $0.1 < \tau < 0.5$  s, which coincides rather well with the Bolgiano regime.

Another conspicuous feature of the pdfs is that they are skewed towards the positive side. The magnitude of the skewness  $S = \langle \delta h(\delta t)^3 \rangle / \langle \delta h(\delta t)^2 \rangle^{3/2}$  is substantial and is dependent on  $\delta t$  or  $l$ . Figure 2-11(b) shows that  $S$  is large in the Bolgiano regime,  $0.1 < \tau < 0.5$  s, and reaches a peak value of 0.25. We believe that this asymmetry is related to the imposed large-scale density variation as delineated in Fig. 2-10. Such an effect has been observed for a passive scalar, such as temperature in a wind tunnel, when a linear temperature gradient is present [53]. However, it is interesting to observe that as far as skewness is concerned, an active scalar (the 2D density in the film) behaves in a qualitatively the same way as a passive scalar.

#### 2.4.4. Full-Field 2D Density Flux Measurements

Finally we show that it is also possible to perform simultaneous measurements of the thickness  $h(x,y)$  and the velocity field  $\vec{v}(x,y)$ . In appendix A, it is shown that within the spectral range of the IR camera,  $8 < \lambda < 14$   $\mu\text{m}$ , the thermal emissivity  $\varepsilon$  is given by  $\varepsilon \approx h/Z_0$  when  $h \ll Z_0$ . The measurements thus allow us to probe the thermal flux as a function of position and time,  $\vec{j}(x,y) \sim (h/Z_0)\sigma T^4 \vec{v} = \sigma/Z_0(\bar{h} + \delta h)(T_0 + \delta T)^4 \vec{v}$ , where  $\bar{h}$  and  $T_0$  are the average film thickness and temperature, which are presumably only the function of  $y$ . The linearized form of the above equation, taking into account  $\delta h/\bar{h} \gg \delta T/T_0$ , is given by  $\vec{j}(x,y) \sim \sigma/Z_0 T_0^4 \bar{h} (1 + \delta h/\bar{h}) \vec{v}$ . If a time average is performed, the averaged thermal flux has a simple form given by  $\langle \vec{j}(x,y) \rangle \sim (\sigma/Z_0) T_0^4 \langle \delta h \vec{v} \rangle$ . As can be seen, the measured thermal flux, within our linear approximation, is formally equal to the 2D density flux in the film.

The thermal images were collected by the Inframetrics IR camera (Model 600L) and the velocity fields were acquired by a PIV system from TSI. The two cameras were synchronized by a video acquisition board in a computer. For each point in the film, the local density flux was calculated by combining the two images. Although the individual flux map appears to be uncorrelated from frame to frame, because of the rate of image acquisition was low (15 Hz), a time-averaged map shows interesting structures in the convection cell as delineated in Fig. 2-12. Specifically, we found that after  $\sim 500$  hundred averages, spanning several minutes of measurement time, the map displays a closed loop occupying the entire cell.

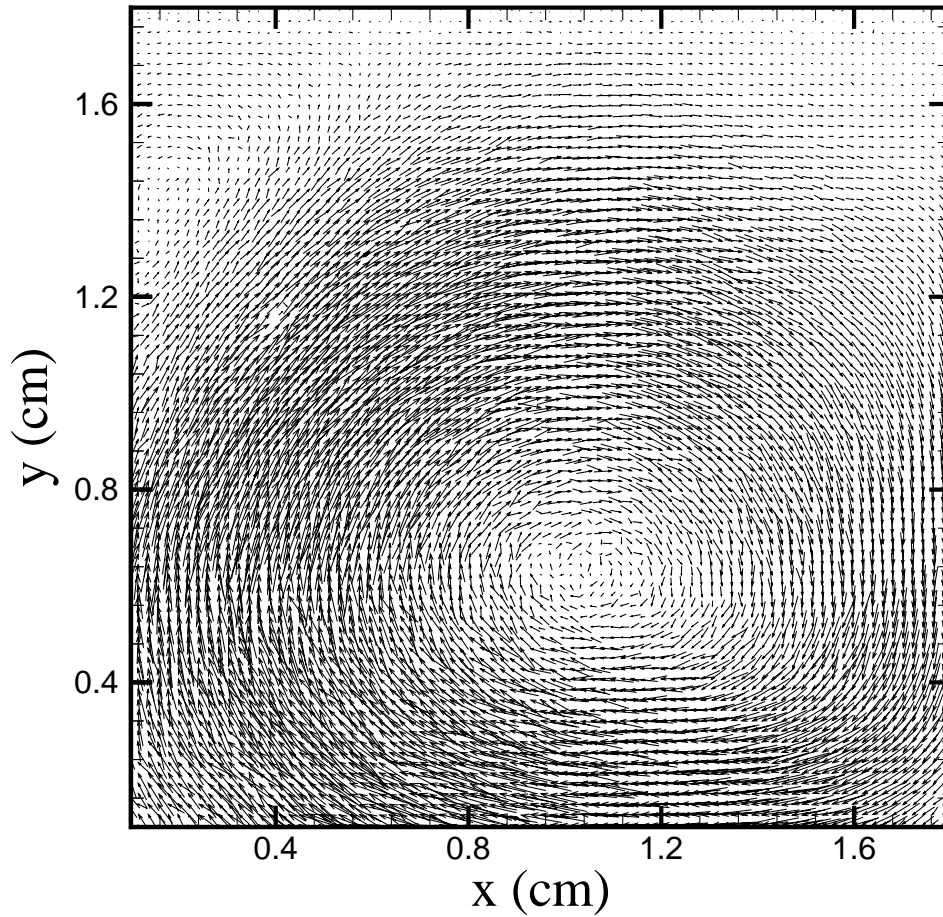


Figure 2-12: The Ensemble Averaged Thermal Flux in Presence of a Large-scale Circulation. Simultaneous velocity and thermal radiation fields were measured at a  $\Delta T=61.5$  K and with  $T_{\text{top}}=14$  °C. This allows the local mass flux to be calculated. Even after the ensemble average over 500 fields, the mass flux still does not average to zero but instead shows a closed loop with a clockwise circulation. The loop is squashed in the vertical direction, resulting from the density stratification.

Such a large coherent structure is not discernible in individual  $\vec{j}(x,y)$ . We noted that the center of the circulation does not coincide with the geometrical center of the cell but is somewhat lower. The data is reminiscent of the large-scale circulation commonly seen in 3D RBC systems and in 2D soap film as shown in Fig. 2-2(b). We believe that with a more sensitive IR camera, which is now commercially available, it is feasible to measure instantaneously local heat and mass fluxes in film. This would give much thrust in the study of convective turbulence in two dimensions.

## 2.5. Summary

Using a home-built radiometer, we have successfully measured thermal radiation from a freely suspended soap film subject to a vertical temperature gradient. The average film thickness profiles are measured and the strong mean density gradients are shown to be the cause of asymmetric emission of thermal plumes. We find for the first time that 2D mass density can switch from stable to unstable stratifications as the temperature difference  $\Delta T$  increases, i.e. when  $\Delta T > \Delta T_C$ . Our observation shows that the transition is closely related to the elimination of the stably stratified top layer when thermal plumes gain sufficient kinetic energy under a large  $\Delta T$ . The inverted density profile then brings about a large-scale-circulation. The formation of large-scale circulation is found to be extremely sensitive to any bias and local perturbation in the system. Even with runs that appear to eliminate all imperfections, the long-term average of the thermal flux still exhibits large coherent structures, which are not to be unexpected.

We also investigated temporal fluctuations of 2D mass density at a single point in the center of the film. The measured power spectra are in good agreement with the Bolgiano's theoretical calculation [28]. Specifically, for the low frequency regime, the power spectrum of 2D density scales as  $\Gamma(f) \sim f^{-1.4}$ . For the high frequency regime,  $\Gamma(f) \sim f^{-\beta}$  with  $\beta$  is between 3 and 4. This scaling behavior  $\beta$  is not well understood at this stage.

Finally, we would like to stress that the technique presented here is noninvasive and has a fast response time of  $\sim 1$  ms. Our simple calculation shows that the technique has the potential to

be used as a radiation *thermometer* for the film if the measured wavelength falls within the strong absorption band of water. By combining this technique with the laser Doppler velocimetry or particle imaging velocimetry new opportunities are created in the investigation of convective turbulence in a strongly stratified 2D fluid.

## 2.6. Appendix A

The lock-in signal  $V$  measures the difference in the radiation powers between the incoming signal  $A$  and the optical chopper  $A_w = \alpha_w \epsilon_w \sigma T_w^4$ :  $V = A - A_w$ . Here  $\alpha_w$  is a proportional constant determined by the geometry of the detector relative to the chopper and the gain of the lock-in amplifier,  $\sigma (= 5.67 \times 10^{-8} \text{ J/s} \cdot \text{m}^2 \cdot \text{K}^4)$  is the Boltzmann-Stefan constant, and  $\epsilon_w$  as well as  $T_w$  are respectively the thermal emissivity and the temperature of the optical chopper. The constant background  $A_w$  can be compensated internally by the lock-in amplifier and thus does not contribute to the signal we observed. In the presence of the film, the incoming signal consists of three contributions  $A = A_f + A_v + A_s$ , where  $f$ ,  $v$  and  $s$  are respectively the film, the water vapor, and the screen behind the film. The  $A_s$  can be treated as a constant since the temperature of the screen is fixed. The rest of the two contributions can be written as  $A_i = \alpha \sigma \epsilon_i T_i^4$ , where  $i = f$  and  $v$ . Because the film and the water vapor are sufficiently far from the detector,  $\alpha$  is treated as a constant factor for both contributions.

To make a quantitative measurement in the film, control experiments are needed to determine all the unknown parameters, such as  $A_s$ ,  $\alpha$ ,  $\epsilon_f$ , and  $\epsilon_v$ . To this end, we used a glass plate 3.0 mm in thickness to determine  $\alpha$ . The plate was heated from behind using a Minco heater and the surface temperature of the glass was measured using a thermistor. The lock-in output due to the thermal radiation from the glass is given by  $V = \alpha \sigma \epsilon_g T_g^4$  and the measured data is displayed in Fig. 2-4. From the slope of this graph and the known thermal emissivity of the glass  $\epsilon_g \sim 0.94$  [38], we determined the constant  $\alpha \sigma = (1.16 \pm 0.10) \times 10^{-10} \text{ volts/K}^4$ . In order to find the constant radiation background  $A_s$  from the screen, the soap solution was removed from the reservoir so that dry air filled the gap between the two aluminum blocks. The background radiation signal from the cold screen (4°C) was found to be only  $A_s = 0.073 \text{ volts}$ , which is quite small compared to signals from the film  $\sim 0.5 \text{ volts}$ .

To estimate the sensitivity of our setup, measurements were also carried out in the presence of a soap film and in its absence. Data were accumulated over several minutes at a regular interval of 1 ms with a 12-bit resolution, and the probability density function for the radiation power from the film was calculated based on time traces similar to that given in Fig. 2-5. As shown by the curve on the right-hand-side of Fig. 2-13, the PDF in the presence of the film is not a strict Gaussian but has a well-defined mean of  $V_{\text{ave}}=0.41$  volts and a full width at the half height  $\delta V = 0.062$  volts. To ensure that the signal was due to thermal radiation from the film, we popped the film and measured the power fluctuations of saturated water vapor in the gap between the two heating blocks. The PDF measured in the water vapor phase, the center curve in Fig. 2-13, is significantly different from that of the film. Not only does the mean voltage drop by nearly a factor of two,  $V_{\text{ave}}=0.225$  volts, but also a significant reduction in the width of the PDF,  $\delta V=0.014$  volts. In the vapor phase, the measured signal is given by:  $V=A_v+A_s =\alpha\sigma\varepsilon_v T_v^4+A_s$  and the variation of  $V$  is given by:  $\delta V=4\alpha\sigma\varepsilon_v T_v^3\delta T_v$ . Dividing the two measured quantities  $V-A_s$  and  $\delta V$  and rearranging terms, we found  $T_v=4(V-A_s)(\delta T_v/\delta V)$ . The temperature variation  $\delta T_v$  in the water vapor phase was directly measured by the thermistor  $\delta T=7.4$  K, and the ratio  $(V-A_s)/\delta V$  measured by the IR detector is 11.01, yielding  $T_v = (325.7 \pm 10)$  K. This value is to be compared with the mean temperature at the middle of the cell:  $T_{\text{ave}} = (T_{\text{bottom}}+T_{\text{top}})/2=316.2\text{K}$ , where the upper and lower temperatures were set at  $T_{\text{top}}=15.5$  °C and  $T_{\text{bottom}}=70.5$  °C. The two values do not agree exactly but are within the uncertainty of our calibration procedure. This measurement also allowed us to find the thermal emissivity of nearly saturated water vapor  $\varepsilon_v=0.12\pm 0.02$  in our experiment.

In the presence of the film, the total signal arrived at the detector is given by the following equation:

$$V=\alpha\sigma\varepsilon_f T_f^4 + \frac{1}{2} A_v + (1-\varepsilon_f)\left(\frac{1}{2} A_v + A_s\right), \quad (2.A1)$$

where  $A_v$  is divided into two parts, one representing the contribution of vapor in front of the film and the other behind it, and  $1-\varepsilon_f$  is the transmittance  $t_f$  of the film defined in Eq. (2.2). Here the approximation of low film reflectance  $r_f \sim R \ll 1$  is made. Because of finite transparency of the film, it follows from the Kirchoff's law that the thickness variation causes the thermal emissivity of the film  $\varepsilon_f$  to change according to Eq. (2.6),  $\varepsilon_f \approx 1 - e^{-h/z_0}$ . Using measured parameters  $\alpha\sigma$ ,

$A_v$  and  $A_s$  and assuming that the average temperature of the film is the same as the vapor, one can estimate  $\varepsilon_f$  from Eq. (2.A1) with the result  $\varepsilon_f \approx 0.183$ . Note that this value is significantly smaller than the thermal emissivity of bulk water ( $\varepsilon = 0.98$ ), implying  $h/Z_0$  is small as well. The Taylor expansion of Eq. (2.6) then yields  $\varepsilon_f \approx h/Z_0 \approx 0.20$ .

It is useful to estimate the relative contributions to the temporal fluctuations of the signal arising from the film thickness and from temperature variations. First let us examine the relative contribution of the first and the second terms in Eq. (2.A1) resulting from variations in  $\varepsilon_f$ . The variance of  $V$  due to these two terms is given respectively by  $\alpha\sigma T_f^4 \delta\varepsilon_f \approx \alpha\sigma T_f^4 |\delta h/Z_0|$  and  $(\frac{1}{2}A_v + A_s) \delta\varepsilon_f \approx (\frac{1}{2}A_v + A_s) |\delta h/Z_0|$ . Using experimentally determined values ( $\alpha\sigma$ ,  $A_s$ , and  $A_v$ ), we find that the second term is only 8% of the first term and is therefore not a dominant contribution to the radiation signal. The variation of  $V$  from the first term in Eq. (2.A1) can be further separated into two parts, one due to the temperature and the other thickness fluctuations with the result:  $\delta V = 4\alpha\sigma T^3 h/Z_0 \delta T + \alpha\sigma T^4 \delta h/Z_0$ . The relative change of  $\delta V$  is given by:

$$\frac{\delta V}{V'} = \sqrt{\left(\frac{4\delta T}{T}\right)^2 + \left(\frac{\delta h}{h}\right)^2}, \quad (2.A2)$$

where  $V' = V - A_v/2 - (1 - \varepsilon_f)(A_v/2 + A_s)$ . Our measurements performed at  $\Delta T = 55$  K showed that in the film  $\delta T \sim 3$  K,  $T \approx 320$  K and  $\delta h/h \approx 0.3$ . This gives the ratio between  $(4\delta T/T)^2$  and  $(\delta h/h)^2$  to be  $\sim 1.5\%$ . This calculation therefore indicates that the dominant contribution to  $\delta V$  is due to the film thickness variation rather than temperature; i.e.,  $\delta V/V' \approx \delta h/h$ , with an uncertainty of about 10%. From measured  $\delta V/V'$  and the estimated  $h (= 0.183 * Z_0)$ , we found that  $\delta h/Z_0 = 0.06$  or  $\delta h/h \sim 30\%$ . The thickness variance  $\delta h/Z_0 \sim 0.06$  corresponds to a change of 0.053 volts in the lock-in output. Since our setup can easily resolve  $\sim 5$  mV, the resolution for thickness fluctuation is approximately  $0.05 \mu\text{m}$ .

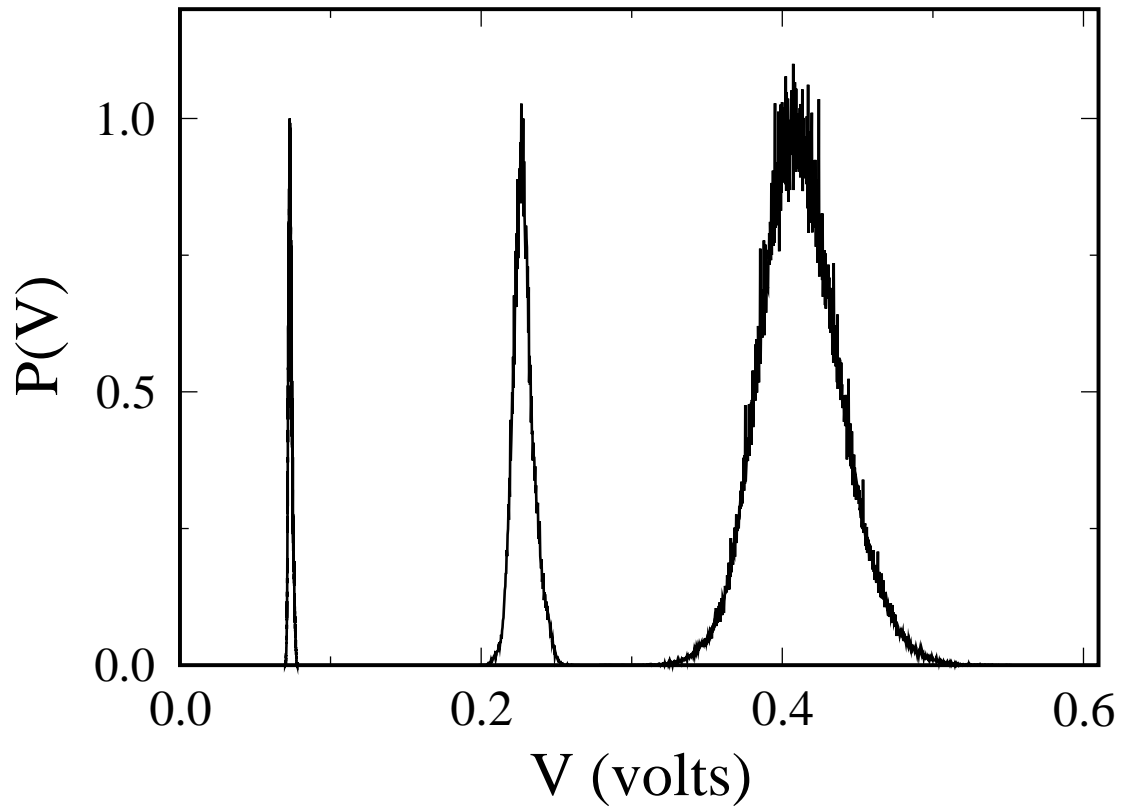


Figure 2-13: The Measured Probability Density Functions of Radiation Power. The probability density functions measured in the presence of the soap film (right), the water vapor but no film (middle), and in the absence of both water vapor and the film (left). The measurements were carried out under the same condition as in Fig. 2-5.

## 2.7. Appendix B

To interpret the transmission data and to deduce the film thickness  $h$ , it is important to know the absorption length of bulk water  $Z_0$ . Fortunately, water is one of the materials that extensive measurements exist and were documented in the literature [54]. Our measurement however is complicated by the fact that a broad band of incoming radiations, from 8 to 14  $\mu\text{m}$ , were simultaneously detected, and the absorption length  $Z_0$  is not a constant throughout this spectral range [54]. As shown in Fig. 2-14, the IR absorption is relatively weak for shorter wavelengths with a correspondingly large absorption length  $Z_0 \sim 17 \mu\text{m}$ , and the absorption becomes stronger for longer wavelengths with  $Z_0 \sim 3 \mu\text{m}$ . Assuming that all wavelengths contribute equally to the measured intensity, the measured transmittance corresponds to

$$\frac{I}{I_0} = \frac{\int_8^{14} e^{-h/Z(\lambda)} d\lambda}{\int_8^{14} d\lambda}, \quad (2.B1)$$

where  $Z(\lambda)$  is the wavelength dependent absorption length represented by Fig. 2-14 and  $I_0$  is the input intensity. The problem can be simplified considerably if the above integral can be approximated by a single exponential function:

$$F(h) = \frac{\int_8^{14} e^{-h/Z(\lambda)} d\lambda}{\int_8^{14} d\lambda} = e^{-h/Z_0}, \quad (2.B2)$$

where  $F(h)$  is the wavelength averaged transmittance. However, the existence of this single-exponential function is not assured in priori because the integration is highly non-linear in  $\lambda$ . We thus resorted to numerical integration of the function  $f(h, \lambda) = e^{-h/Z(\lambda)}$  for a set of  $h$  spanning the range of thicknesses that were relevant to our experiment. A set of curves for  $h=1, 3, 5, 7$  and  $9 \mu\text{m}$  are plotted in Fig. 2-15. As can be seen, for all curves the transmittance is higher for shorter wavelengths than for the longer ones and the total area underneath the curve, representing the total transmittance  $F(h) = \int f(h, \lambda) d\lambda / \int d\lambda$ , decreases as  $h$  increases. Using the Newton trapezoidal integration method, the total transmittance was calculated for different  $h$  and the result is presented in Fig. 2-16. On this semi-logarithmic plot one observed that  $-\ln(F(h))$  vs.  $h$  is

not strictly linear, particularly for large thicknesses. However, for our purpose a linear approximation is more than adequate. Using a linear regression algorithm and imposing the condition that the line has to pass through the origin, it was found that the effective absorption length for our system is  $Z_0=7.83 \mu\text{m}$ .

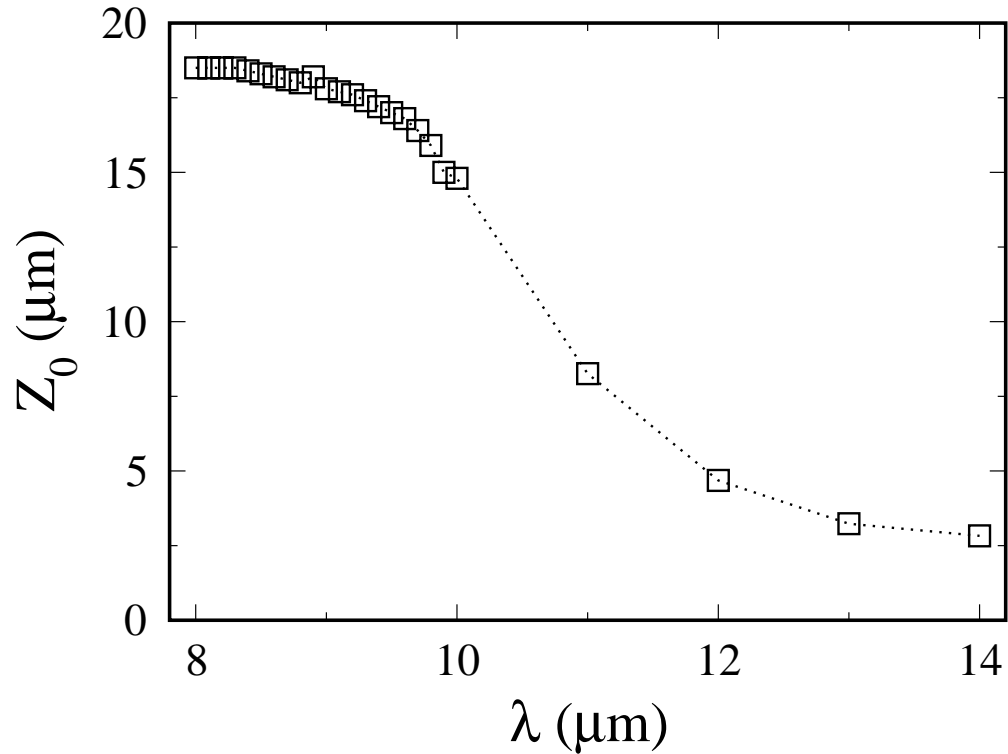


Figure 2-14: The Infrared Absorption Length  $Z_0$  of Water as a Function of Wavelengths. See Ref. [54].

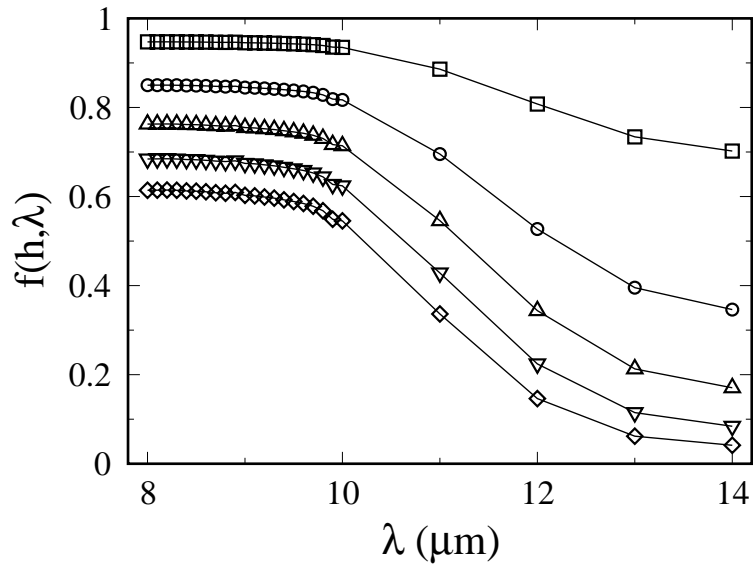


Figure 2-15: The Plot of the Function  $f(h, \lambda) = \exp(-h/Z(\lambda))$  for Different Film Thicknesses  $h$ . The function  $f$  is plotted for the relevant film thickness observed in our experiment. The symbols are respectively  $h=1$  (squares), 3 (circles), 5 (up triangles), 7 (down triangles), and 9  $\mu\text{m}$  (diamonds). The plot is restricted to the camera's spectral range 8-14  $\mu\text{m}$ .

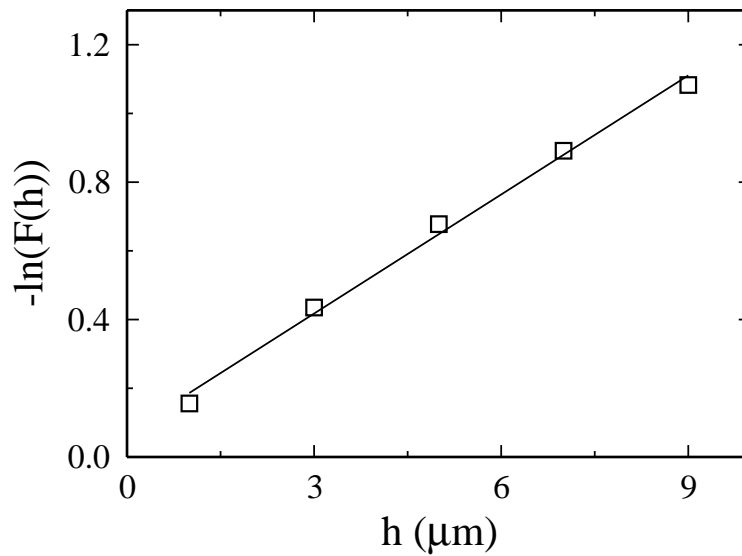


Figure 2-16: The Plot of the Normalized Transmittance  $F(h)$  vs. the Film Thickness  $h$ . The area calculated underneath each curve in Fig. 2-15 is presented. The semi-logarithmic plot shows a quasi-linear behavior. The slope of the line yields the inverse of the effective absorption length  $Z_0$  over the spectral width 8-14  $\mu\text{m}$ . For our system  $Z_0 = 7.83$   $\mu\text{m}$ .

### 3. 2D Density Fluctuations and 2D Compressibility

#### 3.1. Abstract

We present a study of density fluctuations in two-dimensional soap-film convection. When the temperature difference ( $\Delta T$ ) imposed vertically along the film is smaller than a critical value ( $\Delta T_C \approx 48\text{K}$ ), the convective motion is in a strongly stratified state and the frequency power spectrum of density fluctuations shows a Bolgiano-like scaling  $f^{-7/5}$  in the buoyancy sub-range. When  $\Delta T > \Delta T_C$ , the fluid motion crosses over to a strongly mixed state characterized by the emergence of a large-scale circulation (LSC). The density power spectrum in this state has a passive-scalar-like scaling  $f^{-1.0}$ .

#### 3.2. Introduction

Experience informs us that when a soap film is set vertically, it stratifies rapidly. Once the top of the film becomes too thin to support its weight, it breaks. As was discovered a few years ago that when a temperature gradient is applied vertically along the film, steady-state buoyancy-driven convection can be initiated and maintained [17]. The convective flow replenishes the fluid loss due to stratification, making the film more uniform. In the steady state, thermal convection is vigorous and can last indefinitely. The film is stably stratified, similar to the earth's atmosphere, and has strong two-dimensional (2D) characteristics. We noted that the film thickness  $h$  is about  $10^3$  times smaller than its lateral extent and the flow field is constrained to the film plane [55]. This 2D characteristic was exploited in this work by the fact that important dynamic quantities such as the velocity and the 2D density ( $\rho_2 = h\rho_3$ ) of the fluid are assessable by particle image velocimetry and infrared remote sensing techniques [56], where  $\rho_3$  is the density of water. An interesting result of the study is the observation of an abrupt change in the dynamics of density fluctuations and the compressibility of the fluid when the convective motion crosses over from a strongly stratified regime to a strongly mixed regime in which the kinetic energy (KE) of thermal plumes overwhelms the potential energy (PE) of stratification. This crossover is brought about by an increase in the temperature difference  $\Delta T$  and is characterized to be the onset of a large-scale circulation (LSC) spanning the entire system.

The experimental setup is similar to the one described in chapter 2. The overall temperature gradient imposed on the film was given by  $\Delta T/H=(T_{\text{bottom}}-T_{\text{top}})/H$ . The velocity fields were measured using a particle tracking technique [56]. By tracking individual particles, a high vector density (2,500 vectors/cm<sup>2</sup>) was achieved.

A novel feature of the experiment is the application of a mercury-cadmium-tellurium (HgCdTe) detector from EG&G to measure thermal radiation from the film directly. The detector was kept at 77 K to reduce thermal noises. To increase the light collection efficiency, a high numerical aperture lens (NA~1.2) made of ZnSe was used. The incoming signal was mechanically chopped at a frequency of 4 kHz, pre-amplified before it was sent to a lock-in amplifier. A cold black screen (~3 °C) was placed behind the soap film to stabilize a low thermal background.

The radiation power  $P$  received by the IR detector is given by  $P=\alpha\varepsilon\sigma T^4$ , where  $\sigma$ ,  $\varepsilon$ , and  $T$  are respectively the Stefan-Boltzmann constant, the emissivity, and temperature of the film. The constant  $\alpha$  is system dependent and is determined by calibration of the IR setup against a known target. The detailed calibration procedures were reported in previous chapter. The HgCdTe detector has a spectral range of 8-14  $\mu\text{m}$ , resulting in an effective extinction length  $Z_0=7.83 \mu\text{m}$  for water. In all our measurements,  $Z_0$  is greater than the average film thickness  $\bar{h}$  and soap film is semi-transparent to IR photons. Consequently, the thermal emissivity  $\varepsilon$  is not a constant but depends on  $h$  as  $\varepsilon\approx h/Z_0$ . Since the incoming signal contains fluctuations both in  $T$  and  $h$ , the relative contribution to the signal is given by  $\delta P/P=((\delta h/h)^2+(4\delta T/T)^2)^{1/2}$ . For our system  $|\delta h/h|\sim 0.30$  and  $|\delta T/T|\sim 0.01$ ; if one is interested in fluctuations in  $P$ ,  $\delta P$  is dominated by the variations of the film thickness or the 2D density of the fluid. Thus the measured power spectrum yields directly the density fluctuations in the film.

### 3.3. Experimental Results

Figure 3-1 shows a set of shadowgraphs of convection patterns with  $\Delta T=31$  (a), 50 (b), and 62 K (c), respectively. The typical velocity field for each  $\Delta T$  is displayed next to the

shadowgraph. Several interesting features deserve commenting. We noted that thermal plumes are emitted predominantly from the bottom of the cell with only occasional cold plumes from the top. This observation is in contrast with the classical Rayleigh-Bénard convection (RBC), where the up-down symmetry is preserved. We also noted that when  $\Delta T$  is not so large, only the bottom part of the film is mixed by the plumes (see Fig. 3-1(a)), leaving the top part relatively quiescent with intermittent gravity induced oscillatory waves. However, the lower mixed region expands with  $\Delta T$  as plumes gain more KE and are able to ascend to greater heights. This is delineated in Fig. 3-1(b), where thermal plumes are just able to reach the top of the film. As  $\Delta T$  increases further, the system changes its behavior drastically; it appears to lose the left-right symmetry and tends to turnover, producing a LSC, which is delineated in Fig. 3-1(c). The onset of LSC occurred at  $\Delta T_C \sim 48 \pm 2$  K and the phenomenon is akin to those observed in 3D RBC [42] and in liquid crystal films [57]. The velocity fields yield similar information, showing gradual erosion of the quiescent region as  $\Delta T$  increases. This suggests that density stratification is an important element for understanding convection in these films. For all  $\Delta T$ s, the density fields (see shadowgraphs) appear far more complex than the velocity fields, containing intricate folds on different scales. One can also observe secondary instabilities (see Fig. 3-1(a)), where small plumes ride on large falling ones.

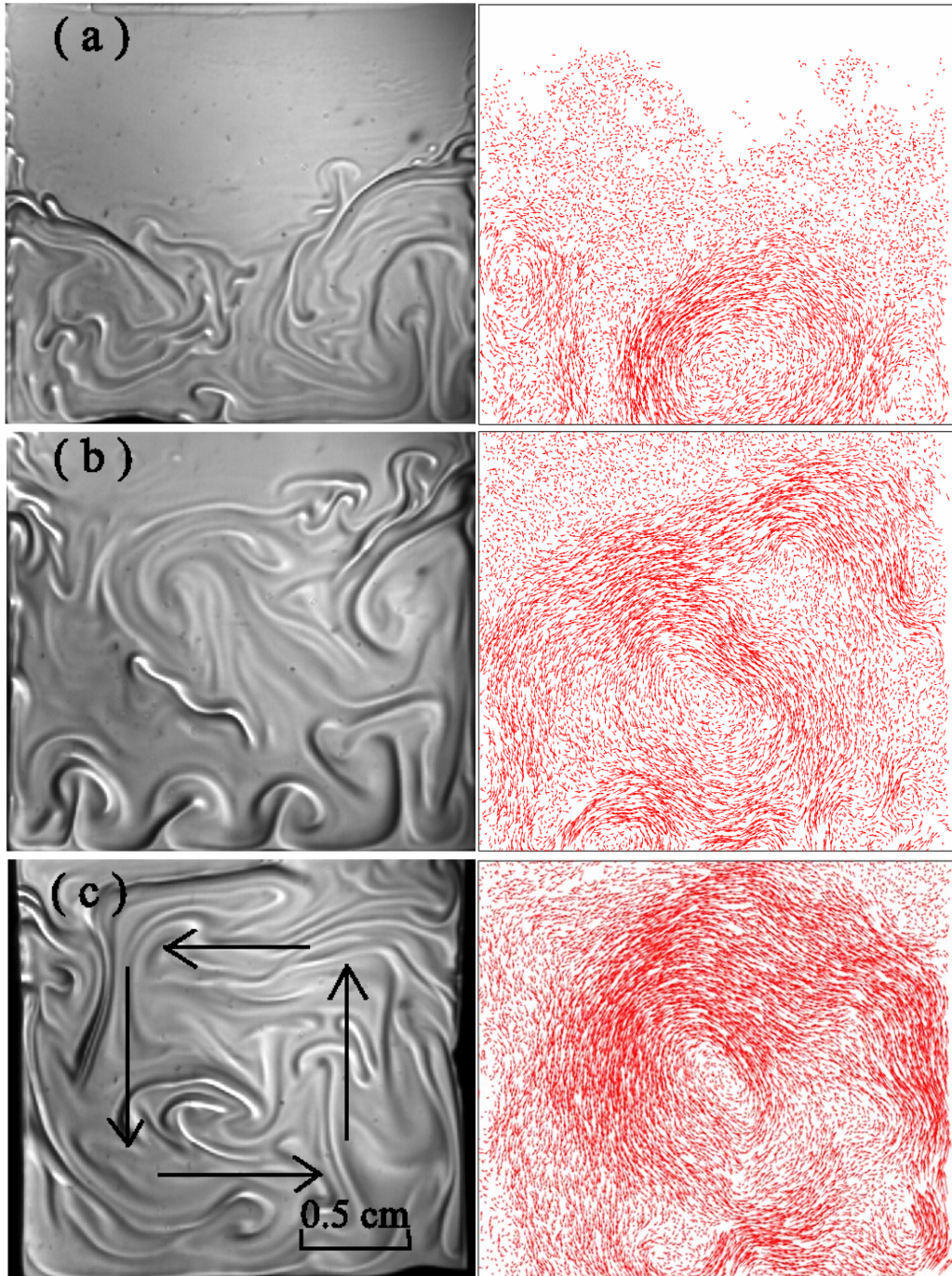


Figure 3-1: Convection Patterns in Soap Films. The pictures on the left were acquired using shadowgraph technique. The shutter speed of the video camera was 1 ms. From top to bottom,  $\Delta T = 31$  (a),  $50$  (b), and  $62$  K (c), respectively. At the top of the film  $T_{\text{top}} = 14$  °C was fixed in all measurements. Typical velocity fields corresponding to  $\Delta T$ s are displayed next to the shadowgraphs. The most striking feature is the gradual erosion of the top quiescent part of the fluid as  $\Delta T$  increases.

To investigate the statistical properties of 2D density fluctuations, the time series of radiation signals were digitized at 1 kHz with a 12-bit resolution. The time-averaged power spectrum  $\Gamma(f)$  was then calculated. Figure 3-2 shows two spectra measured at  $\Delta T_1=44\text{K}$  and  $\Delta T_2=51\text{K}$ . The detector was aligned such that thermal radiation from a small spot (diam=1 mm) at the center of the film was mapped onto the detector. We demonstrated that the radiation signal from the film was significantly greater than the background  $\Gamma_B(f)$ , measured by breaking the film. As illustrated by the lower curves in Figs. 3-2(a-b),  $\Gamma_B(f)$  is nearly three orders of magnitude smaller than  $\Gamma(f)$  for  $0.1 < f < 10$  Hz, where most useful physics are extracted.

Figure 3-2(a-b) shows that all spectra consist of two regimes and can be characterized by power laws  $\Gamma_l(f) \sim f^{-\alpha}$  and  $\Gamma_h(f) \sim f^{-\beta}$  for low and high frequencies. The crossover frequency  $f_c$  in both cases is  $\sim 8$  Hz with a small shift to a higher  $f$  as  $\Delta T$  increases. For  $v_{\text{rms}} \sim 3$  cm/s, the  $f_c$  translates to a spatial scale  $l_c (=v_{\text{rms}}/f_c) \sim 0.38$  cm. The scalar dynamics therefore show remarkably different behaviors above and below  $l_c$ . For the small temperature difference ( $\Delta T_1$ ), the scaling exponents were measured to be  $\alpha=1.4 \pm 0.1$  and  $\beta=4.2 \pm 0.3$ . A similar crossover was also observed for the large temperature difference ( $\Delta T_2$ ), where  $\alpha=1.0 \pm 0.1$  and  $\beta=3.1 \pm 0.3$ . The goodness of the scaling can be examined by the compensated spectra, which are displayed as insets in Figs. 3-2(a-b). Though the scaling range is limited, the exponent  $\alpha$  is nonetheless consistent between different runs and shows a remarkable jump when  $\Delta T$  passes a critical value  $\Delta T_C=48 \pm 2$  K as delineated in Fig. 3-3(a). In contrast the scaling exponent  $\beta$  is less reproducible, showing large variations ( $3 < \beta < 4.2$ ) from run to run (see the inset).

The above observation indicates there is a quantitative change in the density fluctuations before and after the onset of the LSC, which enhances mass transport and may even alter the overall mass distribution in the cell. To shed more light on the phenomenon, we investigated 2D density profiles as a function of  $\Delta T$ . In this part of the experiment, we relied on strong absorption of IR photons by water and used an IR camera (Inframetrics, Model 600L) to record the IR transmittance  $t(x,y)$  in the spectral range of 8-14  $\mu\text{m}$  when a heated plate (300 °C) was placed behind the film. The local film thickness  $h$  can be calculated according to Beer's law:  $h(x,y) = -Z_0 \cdot \ln t(x,y)$  [25].

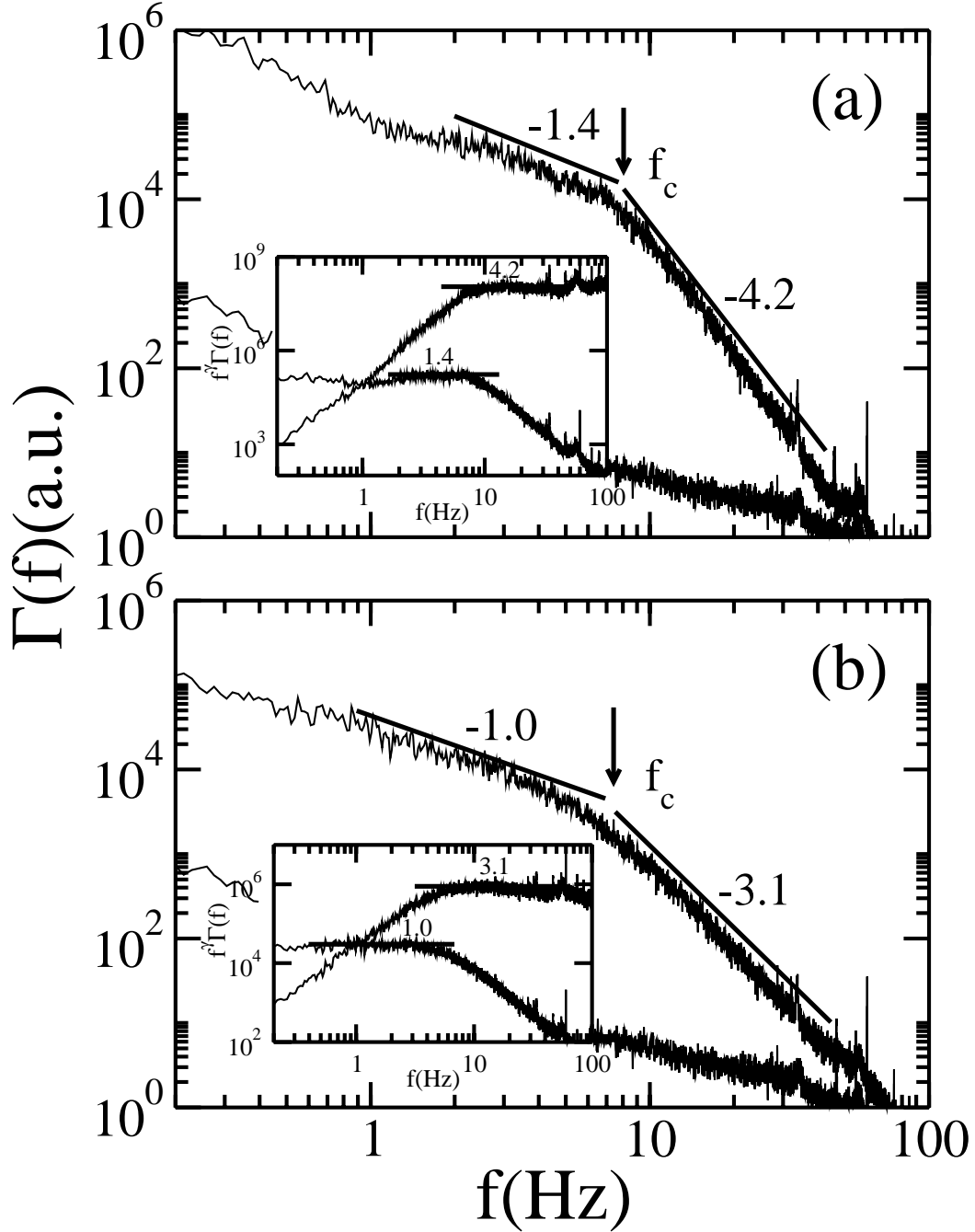


Figure 3-2: The thickness power spectra  $\Gamma(f)$ . They consist of two power-law regimes  $\Gamma_l(f) \sim f^{-\alpha}$  and  $\Gamma_h(f) \sim f^{-\beta}$  separated by  $f_c$ . (a) For a small  $\Delta T (=44\text{K})$ ,  $\alpha=1.4\pm 0.1$  is consistent with the Bolgiano scaling. (b) For a large  $\Delta T (=51\text{K})$ ,  $\alpha=1.0\pm 0.1$  is consistent with the Batchelor exponent. The background radiation is much weaker than the signal, as shown by the lower curves. The compensated spectra are presented in the insets.

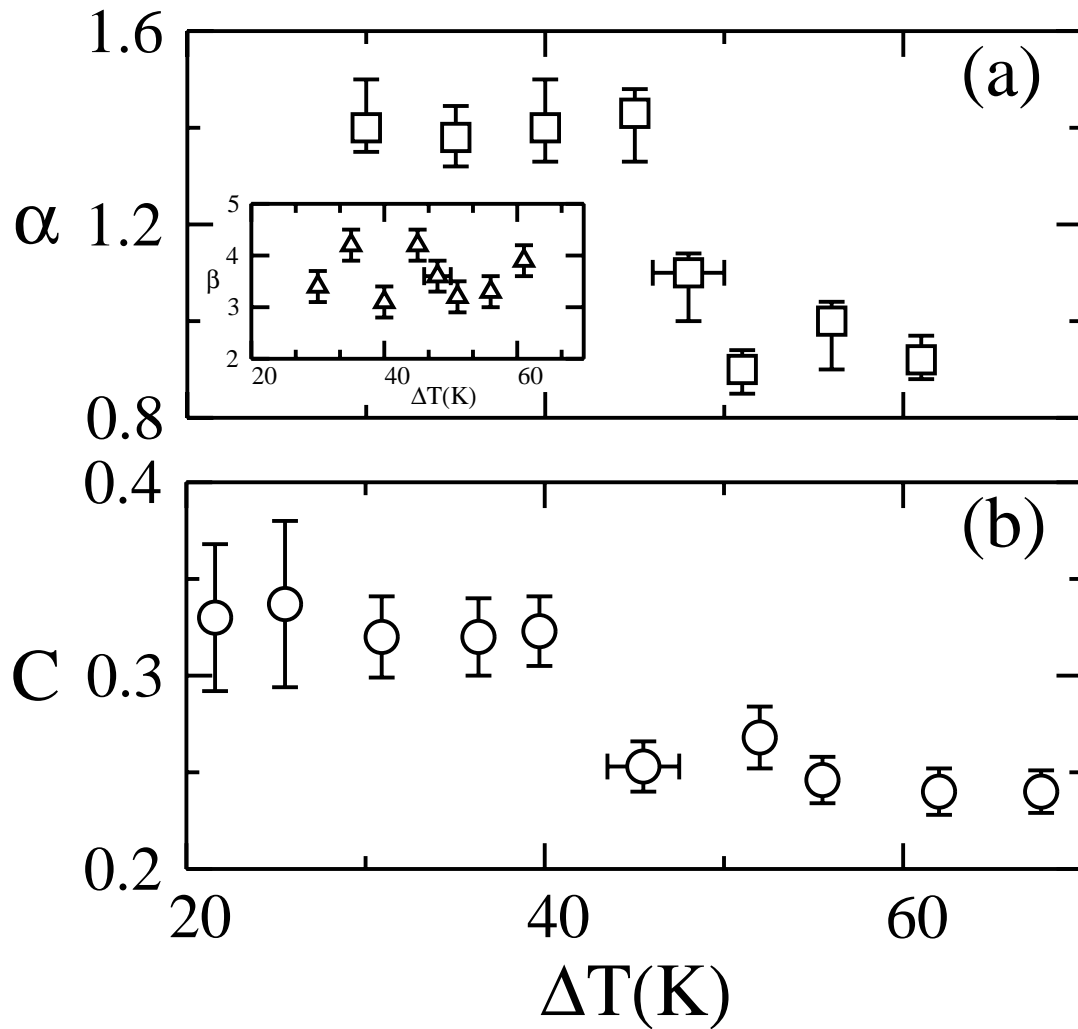


Figure 3-3: The scaling exponent  $\alpha$  and the compressibility  $C$  vs.  $\Delta T$ . Both  $\alpha$  and  $C$  show a sudden jump as  $\Delta T$  crosses  $\Delta T_c \sim 48 \pm 2$  K. The inset of (a) presents the scaling exponent  $\beta$  vs.  $\Delta T$ .

Figure 3-4 shows two thickness profiles measured at  $\Delta T = 37$  and  $61.5$  K. One observes that the foot of the film is rather thick and spans  $\sim 2$  mm in the lower part of the film. Above the foot, the film thins considerably with the average thickness of a few microns. For  $\Delta T = 37$  K (Fig. 3-4(a)), the thickness gradient is stably stratified with  $d\bar{h}/dy < 0$ . However, for a large  $\Delta T = 61.5$  K (Fig. 3-4(b)), the density gradient becomes unstably stratified with  $d\bar{h}/dy > 0$ . Thus the onset of the LSC not only efficiently mixes the film, making it more uniform, but also has the remarkable effect of changing the stability of the film from the stable to the unstable stratification.

Accompanying the change in the mean density profiles, we also observed that the compressibility of the film varies with  $\Delta T$ . The effect is not coincidental but reflects an important coupling between the velocity and the 2D density, i.e., the 2D density in this experiment is *not* a passive scalar. It should also be pointed out that this compressible effect, though involves motion perpendicular to the film, does not affect the two dimensionality of the flow [55]. We defined the

dimensionless compressibility as  $C \equiv \frac{\langle (\nabla_2 \cdot \vec{v})^2 \rangle}{\langle \sum_{i,j} (\partial_i v_j)^2 \rangle}$ , where  $i$  and  $j$  correspond to the two

components of the  $\vec{v}$ , and  $\nabla_2$  is the 2D gradient operator [58]. We noted that by this definition,  $C$  varies between 0 and 0.5, where the upper limit corresponds to the extreme case when  $\partial v_x/\partial x$  and  $\partial v_y/\partial y$  are uncorrelated. The compressibility of the film for each  $\Delta T$  is displayed in Fig. 3-3(b). For a small  $\Delta T (< \Delta T_C)$ , the film is strongly compressible with  $C \approx 33\%$ . This is substantial considering that  $C_{\max}$  is 50%. For a large  $\Delta T (> \Delta T_C)$ ,  $C$  drops precipitously, similar to the  $\alpha$  exponent seen in Fig. 3-3(a), and remains at a constant level of  $\sim 24\%$ . The value of  $C$  is comparable to the fluctuation in  $h$ , which we determined to be  $\delta h/h \sim 30\%$  as seen in previous chapter.

### 3.4. Discussion

To our knowledge density fluctuations in thermal turbulence either in stably or unstably stratified fluids have not been previously studied in a laboratory. Earlier signs that density fluctuations might affect turbulence behavior arose from an internal inconsistency when applying K41 to stratified earth's atmosphere [27, 28].

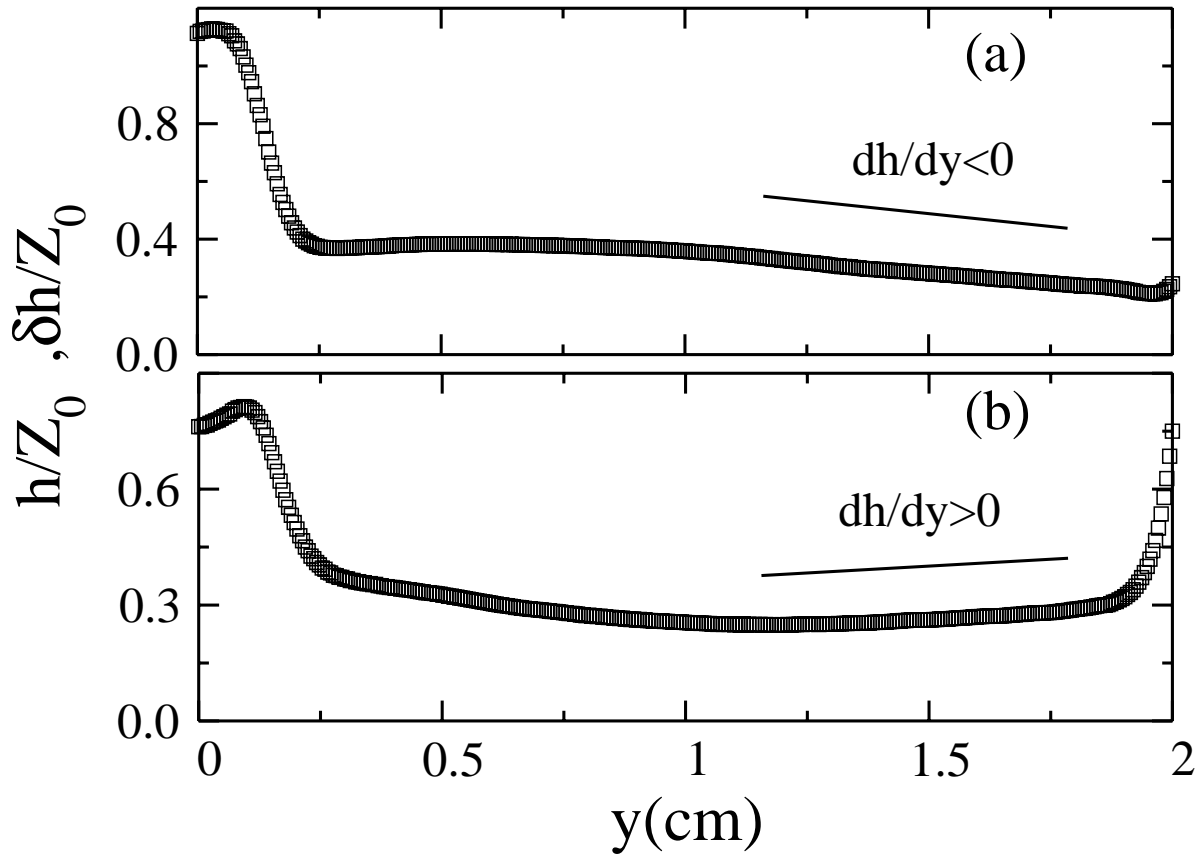


Figure 3-4: The thickness profile  $\bar{h}(y)/Z_0$  vs. vertical height  $y$ . The two figures correspond to  $\Delta T = 37$  K (a) and  $\Delta T = 61.5$  K (b). The profiles are horizontally averaged.

Deviations from the Kolmogorov  $k^{-5/3}$  law were proposed by Bolgiano as a necessary consequence of the exchange of KE of turbulence and PE of density stratification. Bolgiano's fundamental idea can be recast for understanding thermal convection in soap films. The source of KE is thermal plumes that are constantly ejected from the thermal boundary layer. Due to density stratification, when a thick patch of fluid rises from the bottom, its KE is converted to PE and spreads out in space. Thus, over a wide range of scales, there is a tradeoff between KE and PE. However, for sufficiently small scales such a tradeoff is less important because gravitational energy is insignificant on those scales. Thus dynamics on large (PE dominant) and small (KE dominant) scales are expected to be different. The scale separation is given by the Bolgiano scale:  $l_B = 2\pi\chi_\rho^{-3/4}(g/\rho_2)^{-3/2}\varepsilon^{5/4} = 2\pi(g^2/\tau)^{-3/4}(\delta\rho_2/\rho_2)^{-3/2}\varepsilon^{5/4}$ , where  $g$  is the gravity constant,  $\tau$  is the eddy turnover time,  $\varepsilon$  the energy injection rate, and  $\chi_\rho = d(\delta\rho_2)/dt \approx (1/\tau)(\delta\rho_2)^2$  is a constant of motion [28]. Experimentally, we determined  $\delta\rho_2/\rho_2 \approx 0.3$ ,  $v_{\text{rms}} = 3$  cm/s, and the height of the mixing layer  $L \approx 1$  cm. This gives  $\varepsilon = v_{\text{rms}}^3/L \approx 27$  cm<sup>2</sup>/s<sup>3</sup>,  $\tau = 2\pi(L/2)/v_{\text{rms}} \approx 1.1$  s, and consequently  $l_B = 0.13$  cm. The estimated  $l_B$  is comparable in size to the fine striations of thermal plumes (see Fig. 3-1) but is about a factor of 3 smaller than the crossover length  $l_c$ . This discrepancy may be a result of using the Taylor frozen-turbulence assumption to our closed system.

For large scales ( $l > l_B$ ), the density stratification is the source of inhomogeneities and  $\chi_\rho$  is a constant of motion [28]. Based on dimensional grounds, one expects  $\delta\rho_l^2 \approx \chi_\rho(l/v_l)$ , where  $v_l$  is the velocity difference on scale  $l$ . Also for large  $l$ , the tradeoff between KE and PE dictates that  $v_l \sim \sqrt{\delta\rho_l g l / \rho}$ . This yields  $\delta\rho_l^2 \sim \chi_\rho^{4/5} l^{2/5} (g/\rho_2)^{-2/5}$ , which gives the density spectrum  $\Gamma(k) \sim k^{-7/5}$ . This Bolgiano scaling relation is very close to what we have observed in the experiment ( $\Gamma_l(f) \sim f^{-1.4 \pm 0.1}$ ) when (i) the  $f < f_c$  and (ii) the LSC is absent. In the presence of the LSC, the fluid in the center of the cell is efficiently mixed by powerful jets near the side boundaries. The stable density gradient is eroded so that  $\rho_2$  behaves like a passive scalar. The square invariance in this case is again given by  $\chi_\rho$ , but the velocity statistics are determined by random stretching and folding, similar to the passive scalar dynamics deep within a dissipative range [59]. The variance of density fluctuations on the scale of  $l$  is again given by  $\delta\rho_l^2 \approx \chi_\rho(l/v_l)$ , where  $v_l \sim \gamma l$  with  $\gamma$  being the rms shear rate in the fluid. The corresponding

spectrum in this case is  $\Gamma(k) \sim k^{-1}$  as observed. We noted that the Bolgiano scaling was observed in 3D RBC even when LSC was present, in contrast with our observation. The spectra for high wavenumbers  $\Gamma_h(k) \sim k^{-\beta}$  have remained unsettled. Theoretically, it was predicted by Bolgiano that  $\beta$  should follow the Kolmogorov  $k^{-5/3}$  law in the inertial range. To our knowledge this exponent has rarely been observed in convection experiments except in [33]. In our case, since scales smaller than  $l_c$  are strongly affected by the inhomogeneities inside plumes, one cannot rule out the possibility that the observed  $\beta \sim 3-4$  is governed by the properties of the plumes rather than by the large-scale density gradient. In this regard, a better understanding of the plume structure and dynamics is called for.

### 3.5. Summary

To summarize, we have performed 2D density spectrum measurements in a thermally driven soap film that is strongly stratified by gravity. For the film of height  $H=2$  cm, the 2D density varies by nearly a factor of two from the bottom to the top, which is at least an order of magnitude greater than typical RBCs [33, 60, 61]. Within such a strongly stratified film, we observed that as long as the density gradient remains stable, i.e., when the overall PE of the system overwhelms the KE of the plumes, large-scale density fluctuations were in remarkably good agreement with the Bolgiano's prediction for the density spectrum  $\Gamma_l(f) \sim f^{-7/5}$ . However, at the opposite limit, when the KE of the plumes overshadows the overall gravitational PE, large-scale density fluctuations completely alter their behavior and can be explained by chaotic mixing with the spectrum  $\Gamma_l(f) \sim f^{-1.0}$ . Accompanying the spectral change, we also observed remarkable changes in the mean density profiles, from a stable to an unstable stratification, and a sharp drop in fluid compressibility. Thus the onset of the LSC is not only a signature of switching from a PE-dominant to a KE-dominant regime but also plays an important dynamic role, responsible for most of the interesting effects we have observed. However, due to certain features of the soap film, such as its coupling to air and unusual boundary conditions, it remains to be seen whether what we found in this experiment is universal for stably stratified fluids.

## 4. 2D Density Field Measurements Using an IR Camera

### 4.1. Multifractal Measurements of Thickness Dissipations

The multifractal property of the thickness dissipation fields was studied through analyzing a set of thermal radiation images recorded with an IR camera (320 x 256 pixels). The images were taken at  $\Delta T=67$  K, in the presence of large scale circulation. As previously discussed in chapter 2, an IR camera with a spectrum range away from the 3  $\mu\text{m}$  wave length is more sensitive to thickness fluctuations in the soap film. The thickness fluctuation is an important physical quantity in the soap film convection since it is directly related to the 2D mass density fluctuation of the film by multiplying a constant water density.

In 3D turbulence, the coarse-grained kinetic energy dissipation rate in the inertial range being not uniformly distributed in space, is believed to be the cause of the velocity intermittency seen in barotropic turbulence [62]. Because of the multiplicative nature of the energy transfer from scale to scale, the energy dissipation shows multifractal behavior and has been investigated extensively since the experimental work of Sreenivasan [63]. A similar idea was applied to the dissipation of a passive scalar quantity, dye concentration, in the turbulent and the laminar flows [64]. On the other hand, little was known about an active scalar field. The 2D density (or thickness) fluctuation in our soap film is much larger than in normal Rayleigh-Bénard convections [31, 33] and is strongly coupled to the velocity field by the buoyancy effect. The thickness fluctuation is ideal for an active scalar study, thus we are motivated to apply multifractal calculations to analyze the thickness dissipation field in our system.

Figure 4-1 shows a typical thickness dissipation field  $\varepsilon_h(x,y)$ <sup>1</sup>, computed from a corresponding thermal image. The local thickness dissipation  $\varepsilon_h(x,y)$  is defined as  $\varepsilon_h(x,y) \equiv (\partial \delta h(x,y)/\partial x)^2 + (\partial \delta h(x,y)/\partial y)^2$ , in which  $\delta h(x,y)$  is computed with subtraction of the time averaged mean intensity profile from individual thermal image. The numerical values of  $\delta h(x,y)$

---

<sup>1</sup> In this chapter, the symbol  $\varepsilon$  denotes mean square thickness dissipation while in chapter 6 it means kinetic energy dissipation.

as well as all the consequent computed quantities from the  $\delta h(x,y)$  are quantified using the grey scale intensities of images, which differ from the real thickness units by an undetermined constant. One can see from the figure that  $\varepsilon_h(x,y)$  is highly intermittent in the film plane. There are some places with very strong dissipation and other places with very weak dissipation, showing the hallmark of the multifractal characteristics in the thickness dissipation field due to the turbulent convective motion. Hentschel and Procaccia [65] proposed that this type of behaviors can be characterized by the generalized dimension  $D_q$ , which can be further measured by examining the scale invariance of all moments of coarse-grained dissipation  $E_l$  over a broad range of length scales. Here  $E_l$  is the total  $\varepsilon_h(x,y)$  on a square box of size  $l$ ; it is a random variable, which fluctuates from box to box and from picture to picture<sup>2</sup>. The  $q^{\text{th}}$  moment of  $E_l$  can be related to  $D_q$  as following:

$$\sum (E_l / E_0)^q \sim (l / L)^{D_q(q-1)}. \quad (4.1)$$

In the above equation,  $E_0$  is the time averaged total thickness dissipation of the whole film with the system size  $L=2$  cm. And the summation is performed for all boxes, of size  $l$ , covering the whole film. The exponent  $D_q$  is known as the generalized dimension. For positive  $q$ ,  $D_q$  emphasizes rare events with intense thickness dissipation in the boxes, and for negative  $q$ ,  $D_q$  emphasizes the boxes with weak dissipation.

The results of  $\langle \sum (E_l/E_0)^q \rangle$  as a function of  $l$  are plotted in Fig. 4-2, where the angle bracket  $\langle \rangle$  is the time average. Figure 4-2 shows that the  $\langle \sum (E_l/E_0)^q \rangle$  has a good power law relation with length scale  $l$  for more than one decade at different integer number  $q$  from -8 up to 8. The power law exponents  $D_q$  can be extracted from these curves using power law fittings and the final results of  $D_q$  are displayed in Fig. 4-3.  $D_0$  equals 2 as seen in Fig. 4-3 and it is known as the embedding dimension of the measure. Because of the 2D characteristics of a soap film,  $D_0$  is 2.  $D_1$  is defined as  $D_1 \equiv \text{Lim}_{q \rightarrow 1} D_q$ .  $D_1$  is found  $\approx 1.7$  as indicated in Fig. 4-3. Comparing the  $D_q$  results to the measured  $D_q$  of a passive scalar concentration in [64], the general features of  $D_q$  are similar.

---

<sup>2</sup> To calculate  $E_l$ , each  $\varepsilon_h(x,y)$  field is divided to total  $(L/l)^2$  number of square boxes, covering the whole  $\varepsilon_h(x,y)$  field. Different box does not overlap, and each gives one numerical value of  $E_l$ .

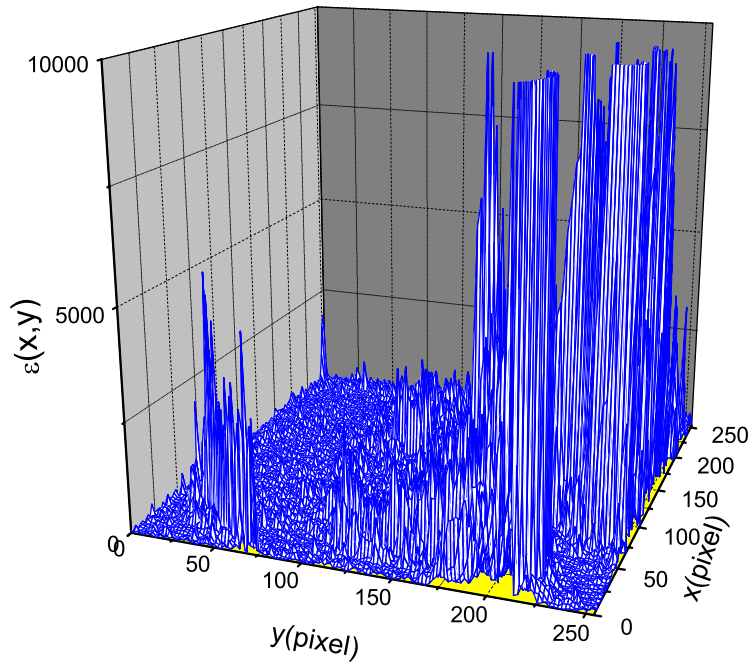


Figure 4-1: A Thickness Dissipation Field  $\varepsilon(x,y)$ . The  $y$  axis is along the vertical direction and the  $x$  axis is along the horizontal direction, with the origins  $(0,0)$  being the top left corner of the film. One pixel size is  $78 \mu\text{m}$ .

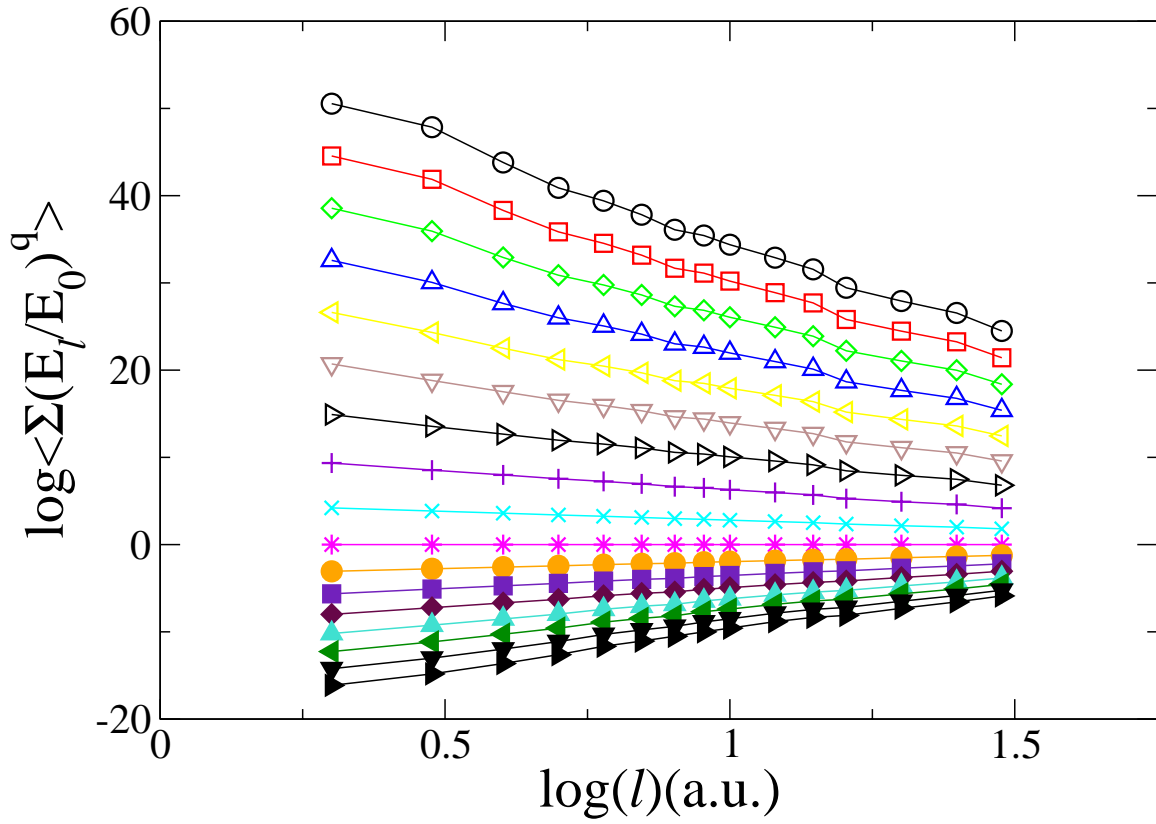


Figure 4-2: The log-log plot of the  $q^{\text{th}}$  moment of the thickness dissipation field  $\langle \Sigma(E_l/E_0)^q \rangle$  versus the box size  $l$ . The different symbols used in the plots stand for  $q=-8$  (the open circles),  $-7$  (the open squares) ...  $q=8$  (the solid triangles right).

An alternative way to characterize the intermittent behavior of the  $\varepsilon_h(x,y)$  field is to measure the multifractal spectrum  $F(\alpha)$  of the singularity exponent  $\alpha$ , which is defined from the relation  $E_l \sim l^\alpha$ . This fancy name ‘‘singularity’’ may come from the fact that when  $l$  goes to zero, the local dissipation density, which is  $E_l$  divided by the area  $l^2$ , might diverge. The exponent  $\alpha$  itself is a random variable, which fluctuates from place to place. Different values of  $\alpha$  imply different self-similarities within the system. The PDF of  $\alpha$  is scale invariant and assumes a functional form  $\sim (l/L)^{-F(\alpha)}$ . Here  $F(\alpha)$  can be shown to be related to  $D_q$  by the simple relation:

$$\sum E_l^q \sim E_0^q \int \rho(\alpha) (l/L)^{q\alpha - F(\alpha)} d\alpha \sim E_L^q (l/L)^{(q-1)D_q}, \quad (4.2)$$

in which  $\rho(\alpha)$  is a pre-factor of  $\alpha$  [63], and the integration is a spatial average over the system for different  $\alpha$  since  $\alpha$  is a spatially dependent quantity<sup>3</sup>. This integration can be further approximated using a saddle point expansion of  $\alpha^*$ , which is simply given by:

$$\partial F(\alpha^*) / \partial \alpha^* = q. \quad (4.3)$$

Hence,  $F(\alpha^*)$  and  $D_q$  could be linked together through:

$$F(\alpha^*) = q\alpha^* - (q-1)D_q. \quad (4.4)$$

Applying the partial derivative to variable  $q$  on both sides of the above Eq. (4.4), one can calculate  $\alpha^*$  for a given  $q$ , based on the measurements of  $D_q$  using the relation:

$$\alpha^* = d[(q-1)D_q] / dq. \quad (4.5)$$

The Eq. (4.4) and Eq. (4.5) are known as the Legendre transformation [62, 63]. From a mathematical point of view, if a PDF of a random variable is known, all the moments of the variable can be calculated, conversely, if all the moments of a variable are known, the PDF can also be constructed [62]. Physically these two methods view the same problem from two different angles, and the approach of  $F(\alpha)$  can be traced back to the Kolmogorov’s 1962 paper [49].

---

<sup>3</sup> Practically, to calculate  $F(\alpha)$ , a time average, namely the average over different images of a time sequence, is usually used in order to improve statistics.

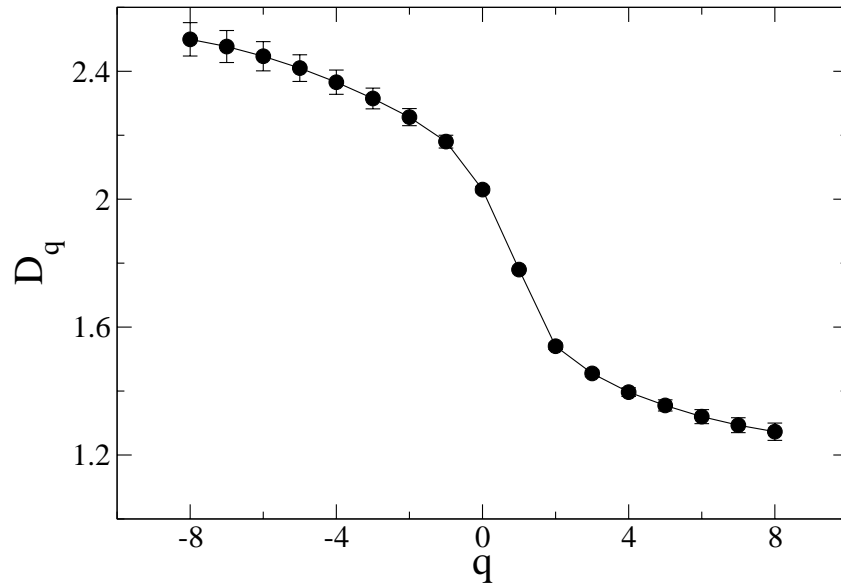


Figure 4-3: The Generalized Dimensions  $D_q$  as a Function of Integer Number  $q$ .

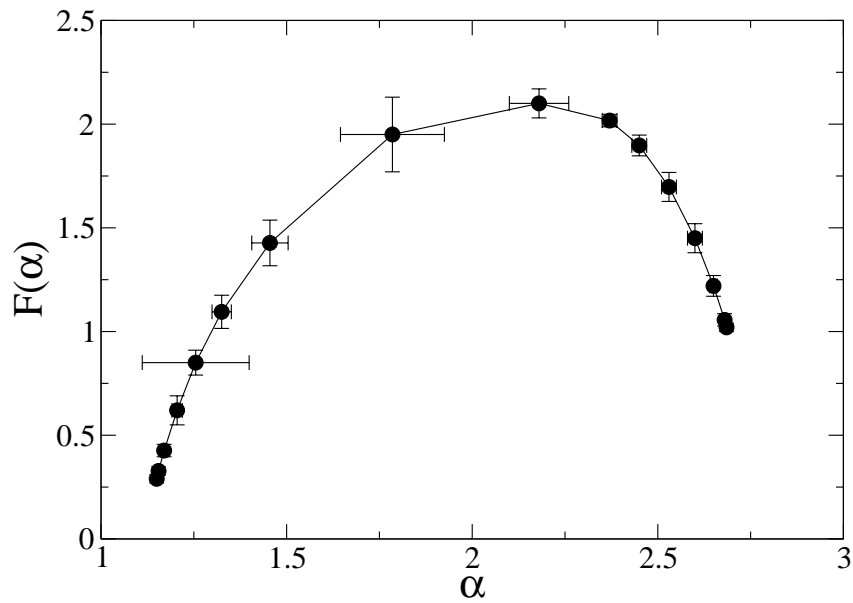


Figure 4-4 The Multifractal Spectrum  $F(\alpha)$  of the Singularity Exponent  $\alpha$ .

After applying the Legendre transformation,  $F(\alpha)$  is calculated and plotted in Fig. 4-4. The measured  $F(\alpha)$ , in the whole range of  $\alpha$  from the numerical values 1.1 to 2.6, has some discernable difference from a second order polynomial function, which usually indicates the lognormal distribution of the dissipation field. Kolmogorov assumed the kinetic energy dissipation in the inertial range obeys a lognormal distribution in his 1962 paper [49] to explain the velocity intermittency. The lognormal distribution has been verified experimentally in the multifractal measurement of the energy dissipation [62]. Here the differing of  $F(\alpha)$  from the lognormal distribution seems to suggest that the thickness dissipation field may inherently depend on the related turbulent velocity field. The correlation between the two fields has been proposed and been tested in the theory and in the experiments for passive scalars [66]. Little was known about the active scalars. Nevertheless, it is reasonable to believe that the correlation of two fields is even more important for an active scalar.

## 4.2. The Potential Energy Field

The potential energy of the fluid motion in thermal convection plays a key role to the understanding of thermal turbulence in both stratified and non-stratified fluids [28, 48]. However a direct measurement of a potential energy field is extremely difficult in 3D thermal convection. In 2D soap film convection, it becomes possible to measure directly the potential energy field using the recorded IR images, which essentially contain thickness fluctuation information. The potential energy  $pe$  of a fluid blob is defined as  $pe = \rho_0 \delta h A g l$ , where  $\rho_0$  is the 3D water density,  $\delta h$  is the film thickness fluctuation,  $A$  is a unit area,  $g$  is the gravitational constant, and  $l$  is the relative height to the bottom of the film.

A  $pe(x,y)$  field is constructed from a thickness fluctuation field by weighting a local thickness fluctuation  $\delta h$  at position  $(x,y)$  with its height  $l$ . One  $pe(x,y)$  field is plotted in Fig. 4-5, in which  $pe$  is expressed as a product of  $\delta h$ , in the grey scale of the IR image, and the  $l$ , in the units of pixel after neglecting the constants of  $\rho_0$ ,  $A$  and  $g$ . By this definition, a patch of fluid with negative  $pe$  has the tendency to absorb the kinetic energy as the time evolves and a patch of fluid with positive  $pe$  tends to release the potential energy back to the kinetic energy. As seen in Fig. 4-5, the distribution of  $pe(x,y)$  is very convoluted, containing many levels of structure.

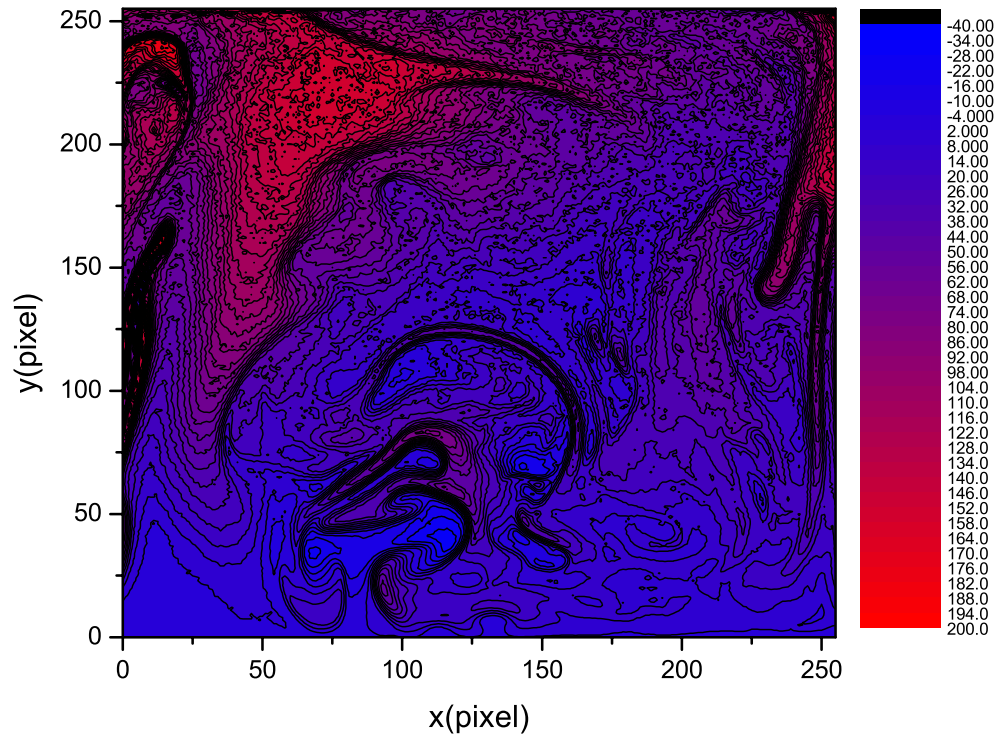


Figure 4-5: A Potential Energy Field  $pe(x,y)$ . The origin  $(0,0)$  is the lower left corner. The intensity of  $pe(x,y)$  is in arbitrary units. Those black lines are contour lines with constant  $pe$ .

As a last test, we calculated the two dimensional spatial correlation of the  $pe$  fields. Figure 4-6(a) is a final result of the correlation after an ensemble average of 600 pictures. The correlation in the horizontal direction is relatively smooth compared with the vertical direction at a scale around 2mm as indicated in Fig. 4-6(b). For even smaller scales, these two correlations in different directions are almost identical. This suggests that the physics above and below the 2 mm scale is very different and the 2 mm scale seems to correspond to the Bolgiano length scale in the system.

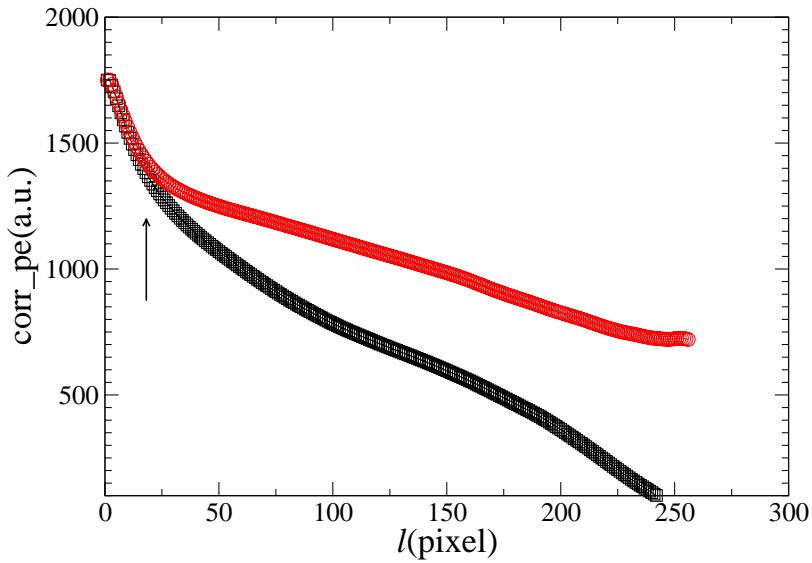
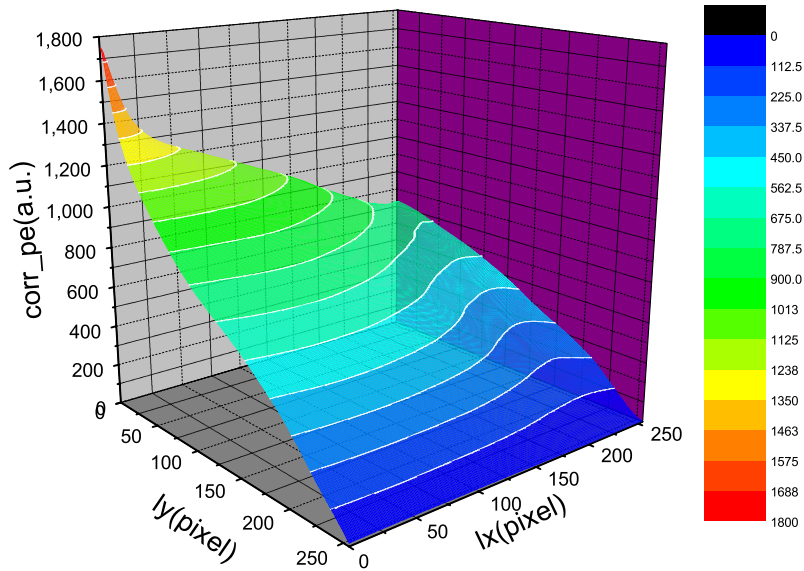


Figure 4-6: The 2D Correlation of  $pe$  as a Function of Separation Distance ( $l_x, l_y$ ). The lower plot is the 1D correlation cut along horizontal and vertical directions, where an arrow indicates the Bolgiano length scale ( $l_B \approx 2$  mm). The red (black) curve is the correlation in the horizontal (vertical) direction.

### 4.3. The skewness of the thickness fluctuations

#### 4.3.1. Lumley's Theory

In Kolmogorov's 1941 paper [47], the kinetic energy flux  $\varepsilon$  was assumed to be a constant in the inertial range, and the kinetic energy spectrum  $E(k)$  in the wavenumber space is only a function of  $\varepsilon$  and wavenumber  $k$ . Hence, the dimensional argument gives  $E(k) = \varepsilon^{2/3} k^{-5/3} \Phi_0$ , where  $\Phi_0$  is a dimensionless quantity. About two decades later, in a paper published in the physics of fluid [70], Prof. J. Lumley generalized the Kolmogorov spectrum form  $E(k)$  to cases, where the kinetic energy flux  $\varepsilon$  is not exactly a constant under the consideration of the external perturbations such as the viscosity effect, the effect of the buoyancy due to temperature field and magnetic field *etc.* An interesting problem discussed in the paper is about the effect of buoyancy, which is manifested by Eq. (11) and Eq. (12) in Lumley's paper. Eq. (11) is given by:

$$\partial \varepsilon_k / \partial k = - (g/T) [\overline{\partial u_3}]_k, \quad (4.6)$$

in which the subscript  $[_k]$  denotes that the quantity is expressed in the wavenumber  $k$  space,  $g$  is the gravitational constant,  $T$  is the absolute temperature,  $\partial$  is the temperature fluctuation, and  $u_3$  is the velocity along the gravitation direction. The above equation describes that the energy flux is not a constant in  $k$  space and it is modified by the buoyancy effect. The line on top of  $\partial u_3$  designates an ensemble average. Using a pure dimensional argument, Lumley got an expression for the heat flux  $\partial u_3$  as following:

$$[\overline{\partial u_3}]_k = \Theta' \varepsilon_k^{1/3} k^{-7/3} 2\varphi(\Theta' g/T \varepsilon^{2/3} k^{4/3}), \quad (4.7)$$

where  $\Theta'$  is the mean temperature gradient, and  $\varphi(\Theta' g/T \varepsilon^{2/3} k^{4/3})$  is a dimensionless function.

The above relation is central and has been used to predict the skewness of temperature fluctuation, as a function of length scale  $l$ , along the direction of mean temperature gradient by many physicists [53, 71]. Let us define the  $n^{\text{th}}$  order structure function of the temperature fluctuation  $S_n \equiv \langle (\partial(x,y+l) - \partial(x,y))^n \rangle$ . Consequently the skewness of temperature fluctuations along the temperature gradient direction is given by the dimensional argument:

$$S_3 / (S_2)^{3/2} \sim S_2(\overline{\partial u_3}) / ((S_2)^{3/2} u_3) \sim (\overline{\partial u_3}) / ((S_2)^{1/2} u_3) \sim (l/l_0)^{4/3} / ((l/l_0)^{1/3} \cdot (l/l_0)^{1/3}) = (l/l_0)^{2/3}.$$

This skewness gradually disappears as the length scale  $l$  becomes very small compared to the system size  $l_0$ . In a more profound way, the memory of an imposed large scale temperature gradient of the system will be gradually lost as a result of the turbulent mixing of temperature fluctuations. In another words, large scale anisotropy will be eventually eliminated at sufficiently small scales, where local isotropy will be recovered. The local isotropy assumption was first utilized by Kolmogorov in his derivation of K41 result [47] and has not been well justified since then [62]. According to K41 theory, the skewness of velocity fluctuations is in the order of unity for all scales along any longitudinal direction, which is a direct consequence of local isotropy assumption. This skewness has a very clear physical meaning for velocity fluctuations because the velocity 3<sup>rd</sup> moment can be related to the kinetic energy flux, which cascades down from large scales to small scales in 3D turbulence. However, the skewness of the scalar field is unexpected and is highly nontrivial since the 3<sup>rd</sup> order moment of the scalar fluctuation does not have the meaning of scalar flux.

The skewness predicted from Lumley's result has been tested in the numerical simulations [41, 72] and in the wind-tunnel experiments of a temperature field with a uniform mean temperature gradient [53]. The findings were contradictory to the prediction. The skewness along the mean temperature direction does not vanish and is in the order of unity at the Kolmogorov's dissipative scale. This finding plays a important role in theoretical developments of passive scalar turbulence [72].

#### **4.3.2. Re-deriving Lumley's Result Using Bolgiano's Assumption**

Because of the experimental finding of the existing scalar skewness in small scales [53], this issue seems to have settled down to the point that it may be foolish to raise the question concerning "whether it is a generic characteristic of a passive scalar that anisotropy can be remembered down to small scales by the turbulent mixing". However, after a careful reading of J. Lumley's original paper, we found that there is a fundamental problem in the derivation, which may potentially cause the skewness prediction to be invalid. Therefore, the whole physical picture towards the understanding of the passive scalar turbulence could be changed.

The starting point of Lumley's paper is very interesting. He tried to examine all the cases where small perturbations of external fields could lead to the changes to the original K41 result [47]. This is conceptually very helpful since K41 assumed local isotropy, which could be broken due to couplings between velocity and external fields. One example of such couplings is the effect of buoyancy, which leads to Eq. (4.7) above. However, Eq. (4.7) will give rise to a  $E(k) \sim k^{-3}$  asymptotic behavior in small  $k$  regimes, which correspond to the large scales. This asymptotic limit recovers a similar result in Wheelon's paper [51]. In the paper, Wheelon also assumed the gradient of the mean temperature  $\nabla\Theta$  is a constant and used this constant to form a dimensional argument, which predicted a  $E(k) \sim k^{-3}$  form in the low wavenumber  $k$  regime. Wheelon's result was strongly criticized by Bolgiano in his review article [73]. If one believes that the Bolgiano's results [28] are correct, then Lumley's dimensional form of the heat flux has to be reformulated in order to give a new asymptotic limit, which shall recover the Bolgiano's scaling relation  $E(k) \sim k^{-11/5}$  in large scales, where buoyancy plays the important role of converting kinetic energy to potential energy. As a consequence, the skewness predicted using Lumley's old relation has to be rewritten.

In the following, we will follow the similar dimensional arguments of Lumley to obtain a new expression of Eq. (4.7) and this new expression will give an asymptotic limit, which recovers Bolgiano's scaling and provides a new form of the skewness! In Eq. (4.6), the  $\partial\varepsilon_k/\partial k$  term in the left hand side has the dimension of  $[\text{cm}^3/\text{s}^3]$ , and this is the same dimension of the  $-(g/T)[\overline{\mathcal{G}u_3}]_k$  in the right hand side. To find the scaling relation of  $[\overline{\mathcal{G}u_3}]_k$  in wavenumber space, we adopted Bolgiano's assumption that the square fluctuation rate of temperature is a constant, which is defined as  $\partial\langle\vartheta^2\rangle/\partial t \equiv \chi_\vartheta$ . Using  $\chi_\vartheta$  to form a dimensional argument, it shows

$$-(g/T)[\overline{\mathcal{G}u_3}]_k \sim \chi_\vartheta^\alpha \cdot \varepsilon_k^\beta \cdot k^\gamma \cdot g/T \sim [\text{cm}^3/\text{s}^3].$$

Since  $\chi_\vartheta$  has a dimension of  $[\text{T}^2/\text{s}]$ , the exponent  $\alpha$  has to be  $1/2$  in order to eliminate the temperature  $T$ . Since  $\varepsilon_k$  has a dimension  $[\text{cm}^2/\text{s}^3]$ ,  $k$  has a dimension of  $[1/\text{cm}]$  and the  $g/T$  has a dimension of  $[\text{cm}/(\text{s}^2 \cdot \text{T})]$ , one substitutes them to the above relation and easily finds  $\beta=1/6$  and  $\gamma=-5/3$ . Applying a similar trick, one will find that the dimensionless function  $\varphi(g/T\chi_\vartheta^{\alpha'} \cdot \varepsilon_k^{\beta'} \cdot k^{\gamma'})$  requires  $\alpha'=1/2$ ,  $\beta'=-5/6$ , and  $\gamma'=-2/3$ . Assembling all these numbers together, the new result becomes:

$$\partial \varepsilon_k / \partial k = - (g/T) [\overline{\mathcal{G}u_3}]_k \sim \chi_\theta^{1/2} \cdot \varepsilon_k^{1/6} \cdot k^{-5/3} \cdot g/T \cdot \varphi (g/T \cdot \chi_\theta^{1/2} \cdot \varepsilon_k^{-5/6} \cdot k^{-2/3}). \quad (4.8)$$

To simplify the above equation, a similar technique as used in [70] is applied, by defining two new variables  $y \equiv (\varepsilon_k / \varepsilon_0)^{5/6}$  and  $x \equiv (k/k_0)^{-2/3}$ . Here  $\varepsilon_0$  is the kinetic energy flux without the perturbation of buoyancy and is a constant in the normal K41 sense, and  $k_0$  satisfies  $g/T \cdot \chi_\theta^{1/2} \cdot \varepsilon_0^{-5/6} \cdot k_0^{-2/3} = 1$ . After a simple algebra, applying the chain law of differentiation, Eqn. 4.8 is now  $\partial y / \partial x = \varphi(x/y)$ . For  $x/y \ll 1$ , one can expand  $y \approx 1 + \varphi_0 x$ . The definition of  $y$  yields  $\varepsilon_k^{2/3} \sim \varepsilon_0^{2/3} y^{12/15}$ . Thus, the K41 spectrum  $E(k) \sim \varepsilon_k^{2/3} k^{-5/3} \varphi \sim \varepsilon_0^{2/3} k^{-5/3} \varphi_0 (1 + \varphi_0 x)^{12/15} \sim k^{-5/3}$ . This implies that for sufficient small scales, K41 scaling still holds. For  $x \gg 1$ , the spectrum  $E(k) \sim \varepsilon_0^{2/3} k^{-5/3} \varphi_0 (1 + \varphi_0 x)^{12/15} \sim k^{-5/3} x^{12/15} \sim k^{-5/3} ((k/k_0)^{-2/3})^{12/15} \sim k^{-11/5}$ , reproduces the Bolgiano's scaling as expected [28]. In the same regime  $x \gg 1$ , one starts from the  $\varepsilon_k^{2/3} \sim \varepsilon_0^{2/3} y^{12/15}$ , which gives that the  $\varepsilon_k \sim k^{-4/5}$ , a result similar to the one found in Ref. [48].

Applying these new results for different  $k$  regimes, the skewness of the temperature is reformulated. In a small  $k$  regime, the skewness is given by:

$$S_3 / (S_2)^{3/2} \sim (\overline{\mathcal{G}u_3})_l / ((S_2)^{1/2} u_3) \sim \varepsilon_l^{1/6} \cdot l^{2/3} / (l^{1/5} \cdot l^{3/5}) \sim l^{4/5} / l^{4/5} = 1.$$

And at the opposite limit in the large  $k$  regime, the skewness is given as:

$$S_3 / (S_2)^{3/2} \sim (\overline{\mathcal{G}u_3})_l / ((S_2)^{1/2} u_3) \sim l^{2/3} / (l^{1/3} \cdot l^{1/3}) \sim l^{2/3} / l^{2/3} = 1.$$

Therefore, in all  $k$  regimes, the skewness of the temperature fluctuations along the mean temperature gradient direction always remains in the order of 1. This is a very encouraging result because it is close to what was seen in the previous studies [53, 71] and is based only on a dimensional ground, without invoking any complicated triple correlations [71].

### 4.3.3. Skewness Measurements

Figure 4-7 is a plot of 2D gradient field of the thickness fluctuation on top of the corresponding 2D thickness fluctuation field. The plume structures are clearly perceptible in the plot. There are two fundamental mechanisms responsible for the large gradients seen here. The first mechanism is because of the 2D compressibility of the film, which could explain those strong thickness gradients almost perpendicular to the mushroom heads of plumes due to the

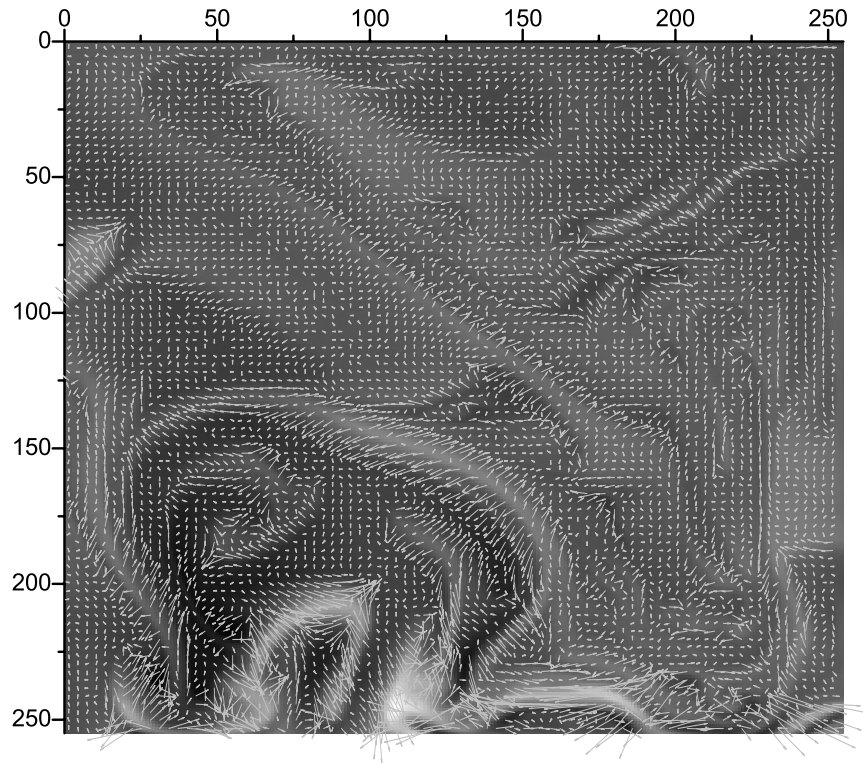


Figure 4-7: A thickness fluctuation field  $\delta h(x,y)$  and its thickness gradient field. The origin  $(0,0)$  is the top left corner of the film.

squeezing of plume fronts. This mechanism is different from most large scalar gradients seen in normal scalar turbulence, where the velocity is incompressible [41]. The second mechanism is due to powerful shears in the velocity fields, which is generally found in literature [41]. Those large gradients near the stems of plumes are due to the strong shears between thin stems and their neighbors. The small plumes are enclosed in a bigger one, which is similar to the super plumes found in strong convection regimes [34]. The topological structures are very complicated, containing many stretches and folds, which is a landmark of the multifractal structures of the thickness dissipation fields. These structures could greatly enhance effective thickness dissipation under the influence of turbulence.

One important issue of scalar turbulence is the local isotropy of the scalar fluctuations. This issue can be revealed by the direct measurement of the skewness of the thickness fluctuations along the vertical, mean thickness gradient, direction for different length scales. The skewness on length scale  $l$  is defined simply as the ratio  $\langle \delta h_l^3 \rangle / \langle (\delta h_l^2)^{3/2} \rangle$ , in which  $\delta h_l \equiv (\delta h(x, y+l) - \delta h(x, y))$ , is the difference of two thickness fluctuations at a vertical separation distance  $l$ . The angle brackets denote spatial average of all pairs followed with a time average of all pictures. The length scale  $l$  covers two decades in scales, from  $\sim 80 \mu\text{m}$  to  $\sim 1\text{cm}$  scales. The PDF on small and large scales skews towards different side, which indicates that the PDF is not self-similar on large and small scales. One specific case of the PDF is when  $l$  equals the smallest scale  $78 \mu\text{m}$ , which is determined by the image resolution, one pixel size. That is the PDF of the thickness gradient along the vertical direction.

The skewness was directly calculated from the PDF for different  $l$ , and the results are plotted in Fig. 4-9. At the smallest length scale  $l=78 \mu\text{m}$ , the skewness of  $\delta h$  gradients is about 0.8, which is close to unity and is similar to the results found in [53]. As  $l$  increases, the skewness decreases and finally becomes negative at large scales. The absolute value of the skewness at the largest scales, about 1cm, is close to 0.8 as found at the smallest scale. When the skewness crosses zero, the length scale  $l$  is around 1.5 mm as seen in the plot, which is very close to the Bolgiano length scale in the system. It is very interesting that the extreme skewness was found on smallest and largest scales, and the skewness switches signs from positive to negative. The decreasing of the skewness as a function of  $l$  has also been found in a wind tunnel

experiment [53], in which the skewness decreases from 1 to a value close to zero as the length scale increases from Kolmogorov dissipative scale to a length scale comparable to system size. However, no negative skewness was discovered in the wind tunnel experiment [53].

The positive skewness in the small scales can be understood intuitively: When a plume rises up it pushes the fluid in its front. As a result, there is a very sharp cliff due to the squeezing of the plume, following with a gentle ramp. This is manifested as those small scale cliff and ramp (CR) structures in Fig. 4-10. The main contributions of the skewness on small scales come from those sharp cliffs, whose gradients align towards the direction of the mean thickness gradient. The mean thickness is sketched using two dashed lines in Fig. 4-10 and has a gradient pointing downwards. Therefore, the skewness on small scales is positive. The negative skewness on large scales can also be explained in a similar way: When a plume rises to the top, because of the gravity, it has to fall down. The falling of the plume occurs on large scales and it also pushes the fluids in its front, producing big CR structures. This is depicted as the large CRs on top of those small scale CR structures. The skewness on large scale thus is dominated by the large scale cliffs, which have the gradient direction pointing opposite to the mean gradient direction. Thereby the skewness becomes negative on large scales. Interestingly, the maximum values of the skewness occur at the largest and smallest scales. A dimensional argument as discussed in the beginning predicts the skewness close to the order of one at all scales, but it can not predict the sign of the skewness. Apparently, the measurement shows more than what could be predicted from the pure dimensional arguments.

#### **4.3.4. Summary**

To summarize, we have measured the skewness of the thickness fluctuations along downward direction and the skewness is nonzero, with positive values in small scales and negative values in large scales. In particular, the skewness at the smallest scale is around 0.8 and the skewness around the large scale is about -0.8. These two values are close to unity as predicted by pure dimensional arguments.

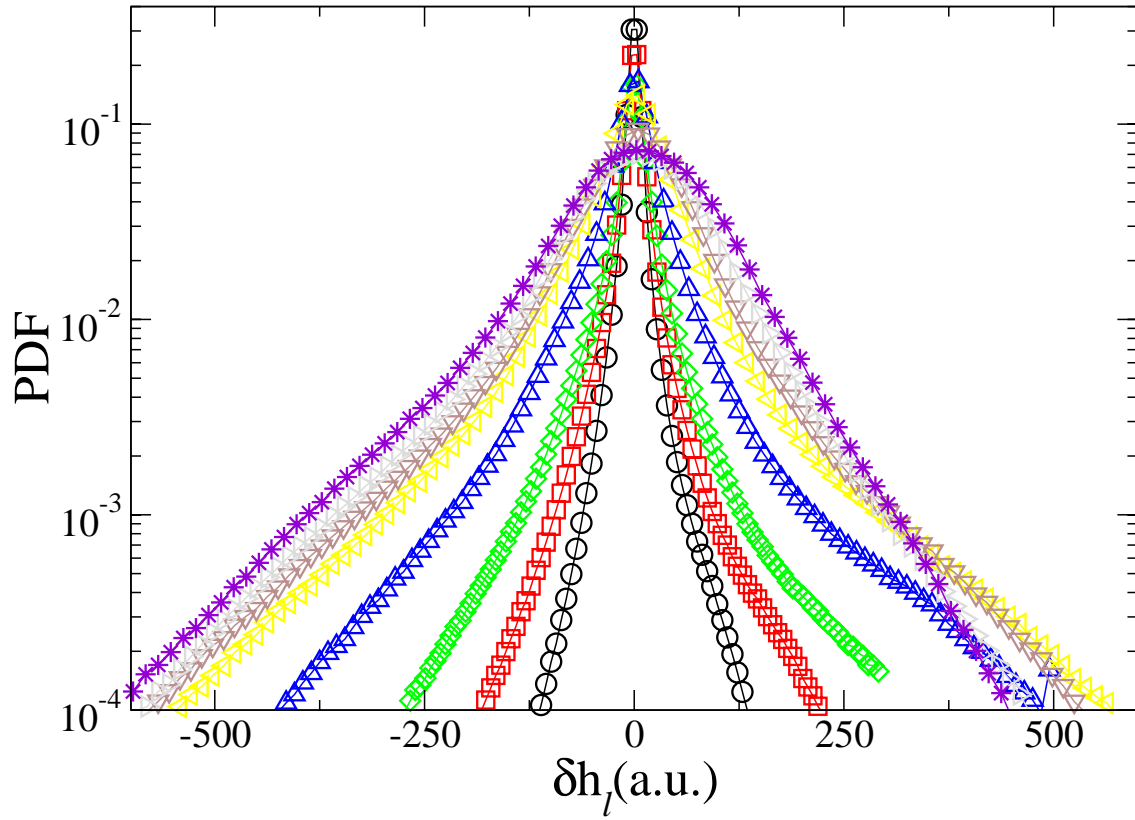


Figure 4-8: The PDF of  $\delta h_l \equiv \langle \delta h(x, y+l) - \delta h(x, y) \rangle$ . Here the angle bracket  $\langle \rangle$  is the ensemble average over the whole film for all  $(x, y)$  followed with a time average of all pictures. The length scale  $l$ s are in the units of pixels. Different symbols are  $l=1$  (circles), 2 (squares), 4 (diamonds), 8 (triangle-ups), 16 (triangle-lefts), 32 (triangle-downs), 64 (triangle-rights), and 90 pixels (stars). One pixel is  $78 \mu\text{m}$ .

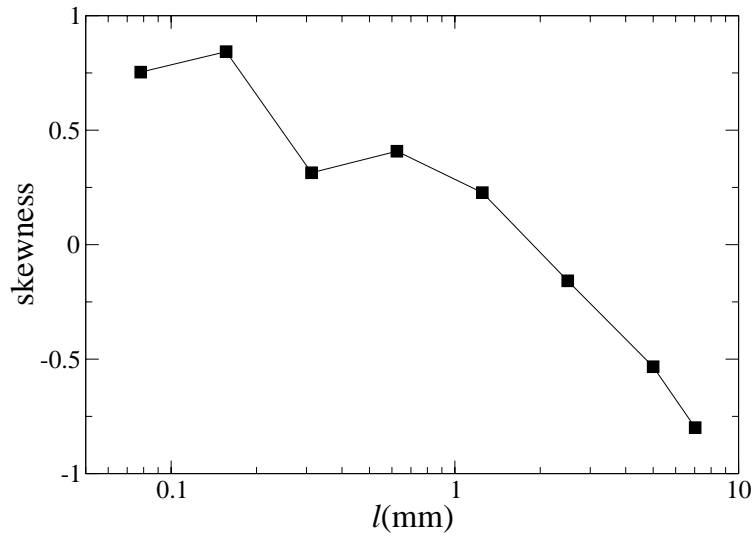


Figure 4-9: The skewness ( $\equiv \langle \delta h_i^3 \rangle / \langle \delta h_i^2 \rangle^{3/2}$ ) along the vertical direction as a function of  $l$ .

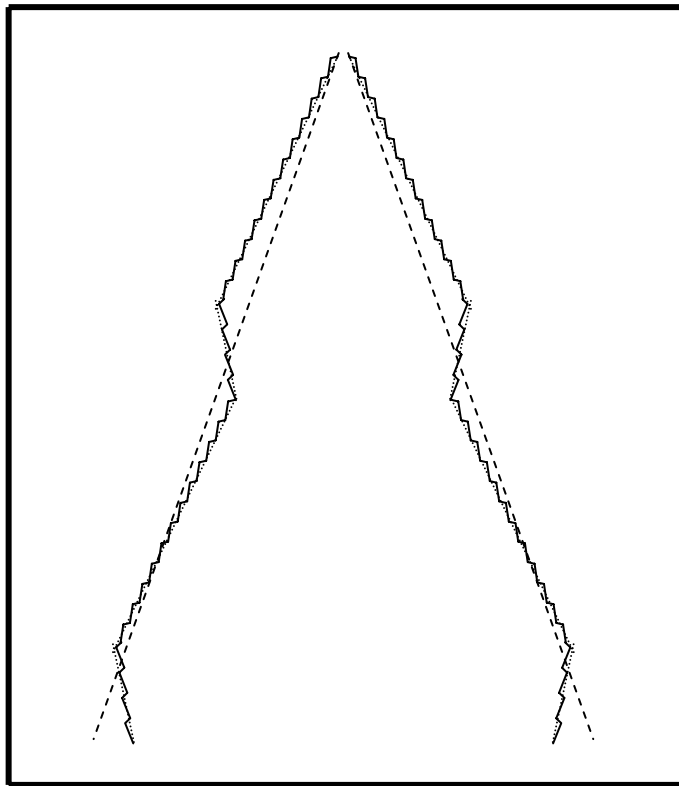


Figure 4-10: A simple sketch demonstrates the existence of positive and negative skewness on small and large scales.

## 5. Single Point Velocity Statistics

### 5.1. Abstract

We investigated velocity statistics of convective turbulence driven by a thermal gradient in a freely suspended soap film. The single point velocity probability density function (PDF) measured at the center region of the convection cell is strongly non-Gaussian and is asymmetric along the vertical direction. For positive fluctuations (velocity against gravity), the PDF is exponential with  $P(v_y) \sim \exp(-c_>(v_y/v_{rms}))$ , whereas for negative fluctuations (velocity parallel to gravity), the PDF is super-Gaussian with  $P(v_y) \sim \exp(-c_<(|v_y+v_0|/v_{rms})^{3/2})$ . We showed that such asymmetry can be explained in terms of plume dynamics and are consistent with the single point velocity theory (Falkovich and Lebedev, PRL, 79, 1997) that relates input and output statistics of turbulence. An interesting buffering effect of turbulent kinetic energy fluctuation is also discovered.

### 5.2. Introduction

In the studies of atmospheric turbulence, it has been long realized that interaction between the turbulence field and the gravitational effect due to buoyancy is significant and could account for noticeable deviations from the Kolmogorov  $-5/3$  law on sufficiently large scales. Such revelations are most commonly demonstrated by velocity second order structure functions and are inspired by Bolgiano and Oboukhov's original theoretical work [28, 74]. In the present work, we report that the exchange of turbulent kinetic energy (KE) and gravitational potential energy (PE) is significant even at the level of single-point velocity statistics. The observation is made possible in a two-dimensional (2D) soap film driven by a vertical temperature gradient along the film. The stratification of the film is significant, which accentuates the importance of gravity on turbulent convection. By means of example, in Fig. 5-1, typical convection patterns, measured at a low temperature difference  $\Delta T=36$  K with an equal time interval  $\tau=1/30$  s, are displayed. They show that, unlike Reyleigh-Bernard convection (RBC), thermal plumes are predominantly ejected from the bottom of the cell and they could not reach the top of the cell unless the initial kinetic energy of the plume is sufficiently large. The overall density stratification in the film, measured from the top to the bottom, is at least a factor of 2, equivalent to the earth's atmosphere of 7 km. Another contribution of this work is the possible connection

between the plume (input) statistics and the single-point (SP) velocity (output) statistics of turbulence. Such a connection has been postulated by Falkovich and Lebedev [75], but to our knowledge, there has been no experimental verification of such a connection.

Our experiments were carried out in a freely suspended soap film that behaves two dimensionally because of its thinness [5, 12, 76]. The soap film is supported by a thin metallic frame and subjected to a vertical temperature gradient ( $\Delta T/H$ ) along the film. Here  $H=2$  cm is the height of the film. The detailed experimental setup can be found in the early chapters of this thesis. For a small  $\Delta T$ , the onset of the flow is oscillatory, consistent with the idea that the system is double diffusive (temperature and density formed two active scalars) and stably stratified [17]. When  $\Delta T$  increases a few degrees above the onset, the flow consists of rolls at the lower part similar to standard RBC, but there is a quiescent regime at the top. The word “quiescent” describes how the fluid at the top is laminar (oscillatory) but not motionless. When  $\Delta T$  increases further, the lower part of the flow is turbulent and dominated by thermal plumes. For  $\Delta T > 48 \pm 3$  K, the flow remains turbulent but is strongly influenced by the presence of a large-scale circulation (LSC) in the film. It should be pointed out that despite the small size of the cell ( $2 \times 2 \text{ cm}^2$ ) hallmarks of Bolgiano-Oboukhov turbulence were observed in the system. In the current study, we focused on plume-dominant regimes in the absence of LSC, where the random emission of thermal plumes assumes that the forcing is stochastic. The magnitude of forcing can be related to plume initial velocities when they emerge from a thermal boundary layer. The plume ejection speed and emission rate were readily measured with the shadowgraph technique, such as graphs seen in Fig. 5-1.

### 5.3. Experimental Results

Using LDV, single point velocity statistics were collected at the locations in the center mixing region of the cell, which is shown more specifically as those red crosses marked in Fig. 5-1. Those locations were selected roughly at the middle of the cell, as seen in the figure.

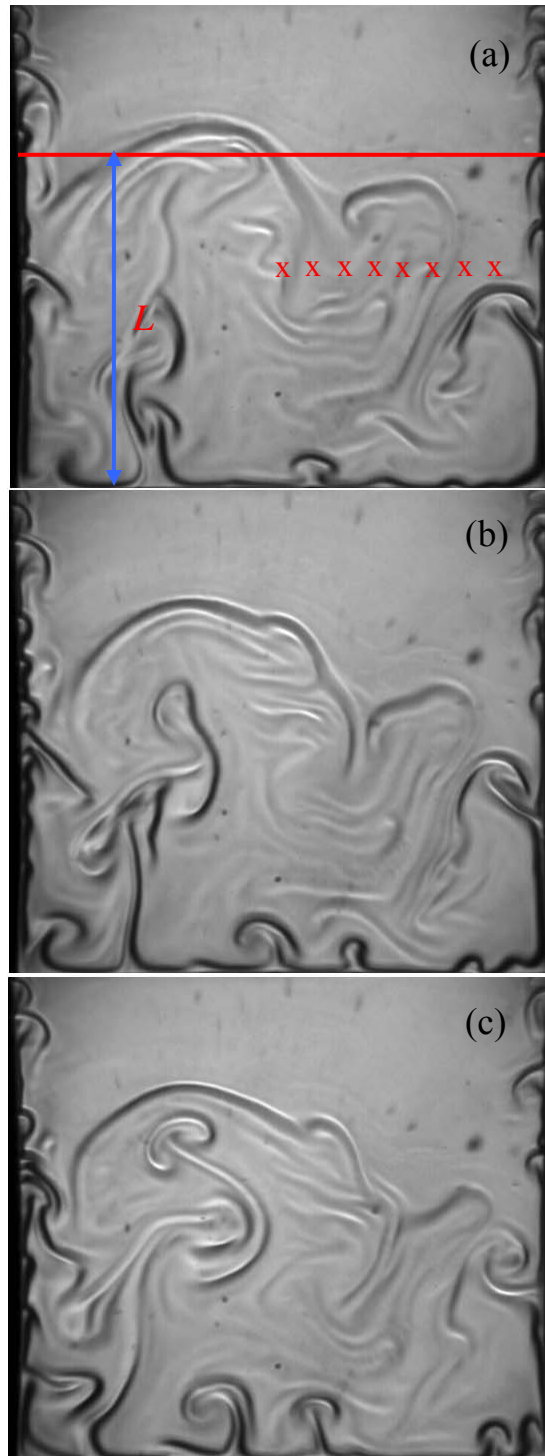


Figure 5-1: Three shadow graphs (a), (b), and (c) of the thermal convection. These three pictures were taken consecutively with a time delay  $\tau=1/30$  s. Red Crosses in (a) illustrate the measurement locations of the single point velocity measurements. There exists a mixing zone as indicated by the blue arrows, with height  $L$ .

In the measurements, the LDV focusing spot was moved from the “red cross” at the center to the other “red crosses” in the right-hand side of the film with no measurements made in the left side of the film, assuming the statistical properties of the SP velocity are left-right symmetric along the vertical center line of the film.

As demonstrated in Fig. 5-2, the PDF of the velocity component along the vertical direction  $v_y$  is strongly anisotropic, which is a hallmark of convective turbulence under the influence of gravity. The positive  $v_y$  is defined in the direction against gravity. The temperature difference was  $\Delta T=31.1$  K and different symbols correspond to different horizontal positions of the measurements performed in the convection cell; see the figure caption for more details. We noticed that even along the vertical direction, Fig. 5-2(b), the fluctuation along  $+y$  is significantly more intermittent than that along the  $-y$  direction (the gravity direction). As will be seen below, this asymmetry is mainly due to velocity fluctuations in  $+y$  is strongly influenced by random emission of thermal plumes, whose speed has a broad distribution. However, since there are few cold plumes emitting from the top, the fluctuation of negative  $v_y$  is weakly affected by plume statistics. Quantitatively, it was found that the tails of PDF could be described piece-wise by the following functions:

$$P(v_y > 0) \propto \exp(-c_> v_y / v_{y\text{rms}}), \quad \text{and}$$

$$P(v_y < 0) \propto \exp(-c_< (|v_y + v_0| / v_{y\text{rms}})^{3/2}),$$

as delineated by the solid lines in the graph, where  $P(v_y < 0)$  is plotted using an orange solid line with a dotted line extending the functional form to positive  $v_y$ , and  $P(v_y > 0)$  is illustrated with a red solid line up to  $v_y \approx 12$  cm/s, which is 4.6 times of  $v_{y\text{rms}}$ . In the above functions,  $v_{y\text{rms}} = 2.63 \pm 0.08$  cm/s,  $c_> = 0.87 \pm 0.02$ ,  $c_< = 2.44 \pm 0.11$ , and  $v_0 = 1.2 \pm 0.1$  cm/s, respectively. The  $v_y$  with very large values are rare as seen from the sharp decay of PDF for  $v_y > 12$  cm/s. Figure 5-2(a) plots PDF of the horizontal component of velocity  $v_x$ . In this case we found that the PDF is nearly symmetrical in the two tails in terms of their shapes, which show a functional form close to the negative fluctuations of  $v_y$ , i.e.  $P(v_x) \propto \exp(-c |v_x + v_0'|^{3/2} / |v_{x\text{rms}}|^{3/2})$ , where  $v_{x\text{rms}} = 1.56 \pm 0.23$  cm/s,  $c = 1.11 \pm 0.06$ , and  $v_0' \approx 0$  (circles)  $v_0' \approx 0.25 \pm 0.23$  (squares). The orange solid line is a super-Gaussian curve, which compares favorably with the tails of PDF.

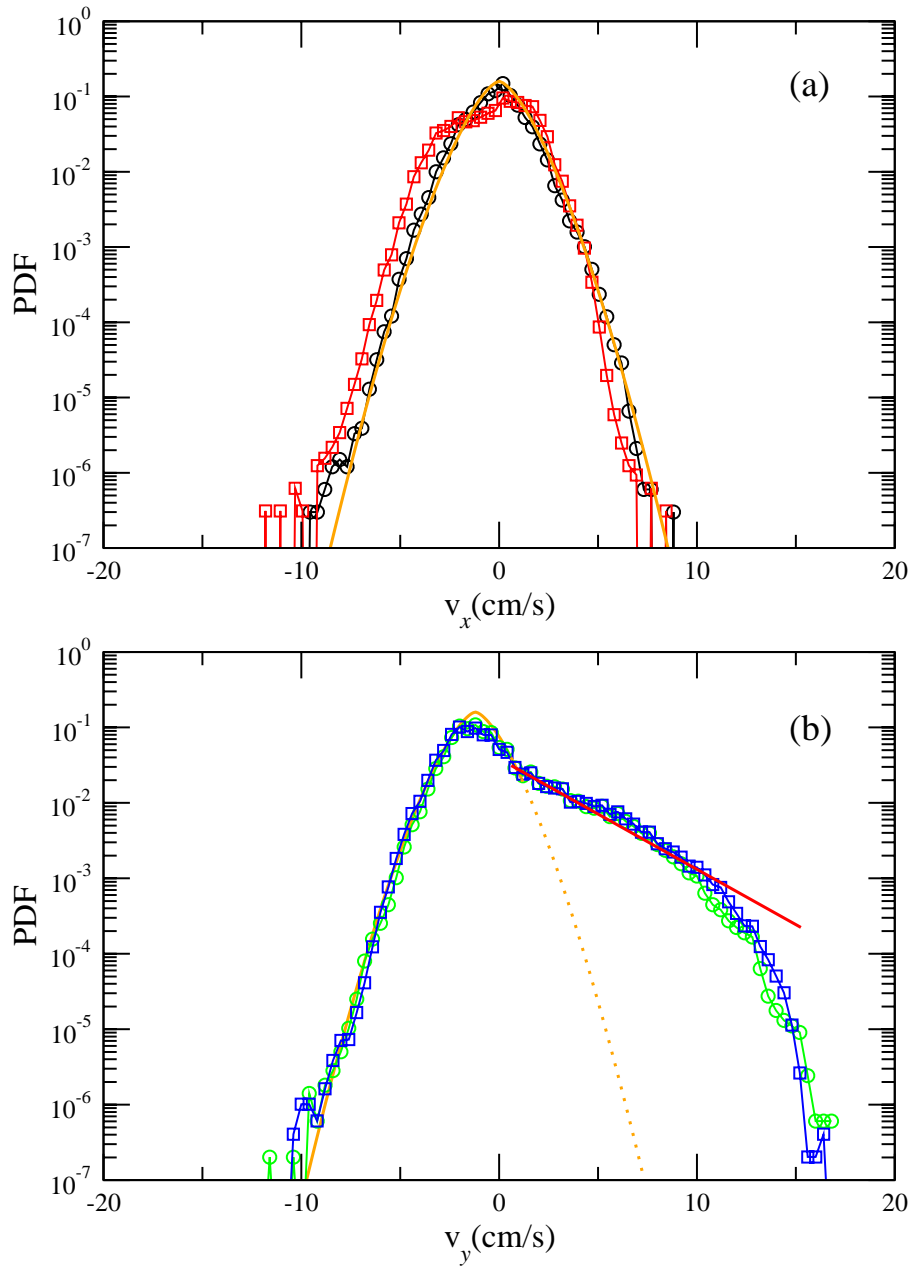


Figure 5-2: Single-point Velocity PDF along the Horizontal  $x$  Direction (a) and along the Vertical  $y$  direction (b). In (a) and (b), the circle symbol is measured at the center, and the square symbol is measured 2mm away from the center. In (a), PDF are close to super-Gaussian forms in the tail part and in (b) PDF have large slow decay tails for positive  $v_y$ .  $\Delta T=31.1$  K in the measurements, and the film with a square geometry is used.

The existence of  $v_0'$  is the reflection of existing biased flow in our system due to the side walls. It is noticeable in Fig. 5-1 that the plumes close to the two side walls tend to move towards the walls. As a result, statistically speaking eddies rotate more frequently from the walls to center than from the center to the walls. In Fig. 5-2(a), for the SP velocity measurement performed at center (the left most “red cross” indicated in Fig. 5-1) shows a negligible mean flow  $\langle v_x \rangle \approx -0.06$  cm/s because the center spot is almost symmetric for two side walls. The negative sign of  $v_x$  is defined as the direction from the right wall to the center. However, the square symbol, which were measured at 2 mm away from the center, shows a noticeable mean flow  $\langle v_x \rangle = -0.21 \pm 0.22$  cm/s. This mean flow of  $v_x$  has an absolute value close to the  $v_0'$  in above  $P(v_x)$  expression. We also noted that  $v_0$  in  $P(v_y < 0)$  is nonzero and  $v_0 = 1.2 \pm 0.1$  cm/s. The survival of  $v_0$  may come from two different reasons. The first cause is reminiscent of the mean flow  $\langle v_y \rangle = -0.245 \pm 0.3$  cm/s due to a similar argument as  $v_x$ . Even after considering the nonzero  $\langle v_y \rangle$ ,  $P(v_y)$  will still not peak at  $v_0 = 0$  cm/s because of the large slowly decaying tail of  $P(v_y > 0)$ , which is the second cause.

In order to make sure that the observation of the SP velocity statistics is robust, we also did measurements at different  $\Delta T$ s. Figure 5-3(a,b) is another set of data taken at a  $\Delta T = 37.1$  K with the same measuring locations as in Fig. 5-2(a,b). Comparing with Fig. 5-2(a,b), the shapes of PDF are similar. Those fitting parameters are  $c = 1.05 \pm 0.03$ ,  $v_0' = 0.31 \pm 0.05$  cm/s,  $c_< = 1.7 \pm 0.1$ ,  $c_> = 0.85 \pm 0.13$ , and  $v_0 = 1.5 \pm 0.1$  cm/s for the given  $v_{x\text{rms}} = 1.65 \pm 0.04$  cm/s,  $\langle v_x \rangle = -0.24 \pm 0.15$ ,  $v_{y\text{rms}} = 2.70 \pm 0.1$  cm/s, and  $\langle v_y \rangle = -0.74 \pm 0.3$  cm/s.

Intriguing from those SP velocity statistics measurements from Fig. 5-2 and Fig. 5-3, we made one more extensive measurement at a  $\Delta T = 41.7$  K for different locations spanning from the center up to 2 mm from the right side wall. During the experiment, there were two little bubbles (millimeter size or less) trapped in the left corner. The “left” denotes the opposite side of the measurement locations and has the same meaning as in Fig. 5-2 and Fig. 5-3. The results were displayed in Fig. 5-4(a,b), in which different symbols were used to represent a set of locations. The PDF of  $v_x$  at different locations resemble each other and also close to a super-Gaussian form as delineated with the violet solid line, which has  $c = 1.0 \pm 0.06$ ,  $v_0' = 0.4 \pm 0.1$  cm/s,  $c_< = 1.52 \pm 0.08$ ,  $c_> = 0.94 \pm 0.03$ , and  $v_0 = 1.6$  cm/s.

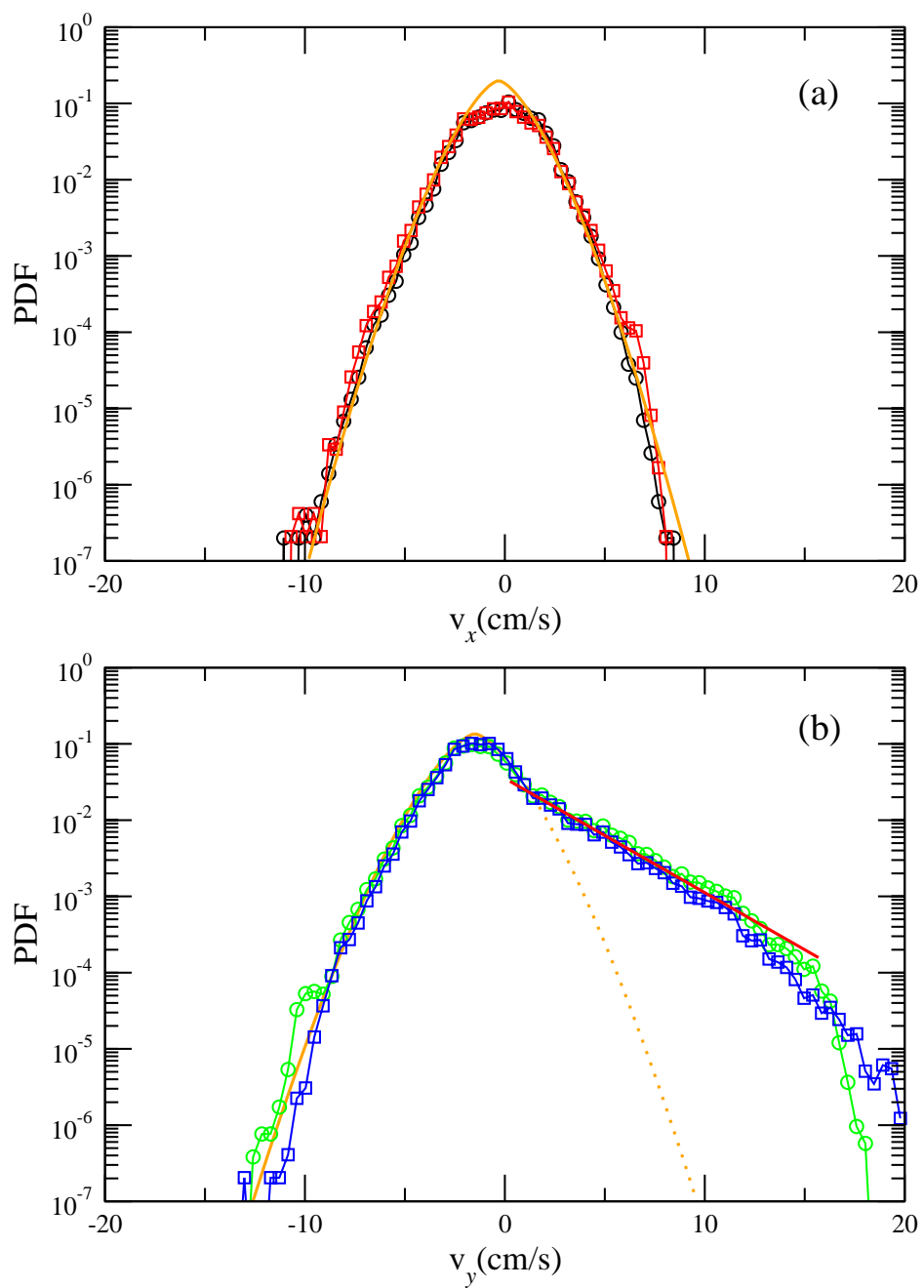


Figure 5-3: Another set of PDF measured in a square geometry at a different  $\Delta T=37.1$  K with all other conditions same as Fig. 5-1.

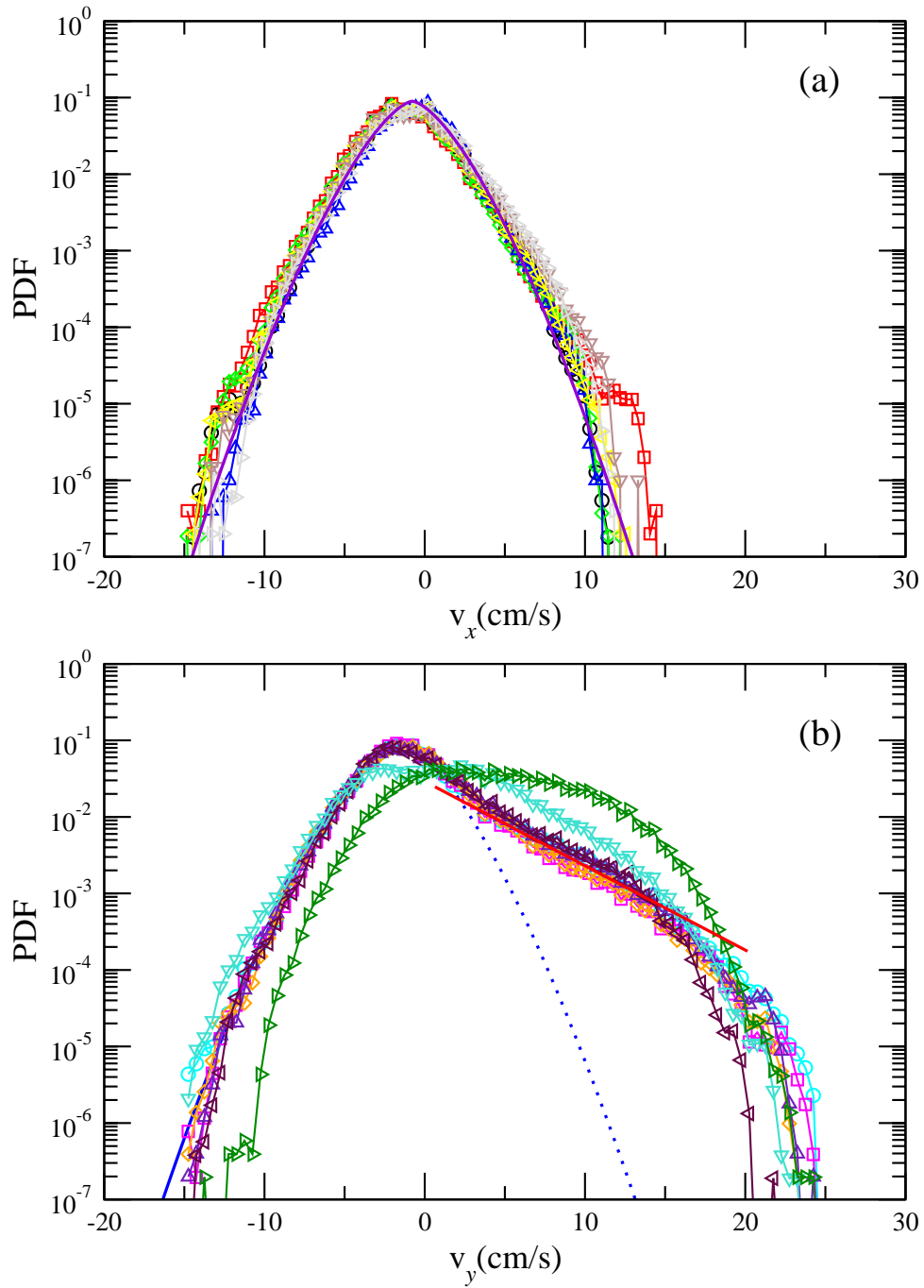


Figure 5-4: Single point velocity PDF measured in a square geometry at  $\Delta T=41.7$  K in the absence of large scale circulation. Different symbols stand for different measurement spots away from the center of the cell, circles (0 mm), square (1 mm), diamond (2 mm), triangle-up (3 mm), triangle-left (4 mm), triangle-down (6 mm) and triangle-right (8mm). Again, (a) plots PDF of  $v_x$ , and (b) plots PDF of  $v_y$ .

Notice that the values of  $c$ ,  $c_<$ , and  $c_>$  are very close at different locations except the locations very close to side wall, i.e. those two  $P(v_y)$  (triangle-downs and triangle-rights) show strange shapes in Fig. 5-4(b). In a contrast,  $v_0'$  and  $v_0$  generally depend on local mean flows along  $x$  and  $y$  directions thus vary from place to place, which can be evident from those spreading of different symbols in the figure.

To make a complete story, the local mean flow  $\langle v_x \rangle$ ,  $\langle v_y \rangle$ , and the local fluctuations  $\langle (v_x - \langle v_x \rangle)^2 \rangle^{1/2}$ ,  $\langle (v_y - \langle v_y \rangle)^2 \rangle^{1/2}$  as a function of distance  $\Delta x$ , which is defined as zero at the center and 1 cm at the right wall, are calculated using the same set of data as Fig. 5-4 and plotted in Fig. 5-5(a-d). Figure 5-5(c) shows that the mean flow along  $y$  direction  $\langle v_y \rangle$  is strongly positive at the boundary and switches to negative sign when approaching the middle. Right at the wall ( $\Delta x = 1$  cm),  $\langle v_y \rangle$  must vanish as a direct consequence of the non-slip boundary condition. For  $0 \leq \Delta x \leq 4$  mm,  $\langle v_y \rangle$  is almost a constant, it then crosses the zero around  $\Delta x = 5$  mm, and finally it grows linearly for  $5 < \Delta x \leq 8$  mm. This region, about 2~3 mm away from the wall, can thus be characterized as a turbulent velocity boundary layer, which is further confirmed from Fig. 5-5(d) since the local fluctuations in this region are also stronger. In Fig. 5-5(a,b),  $\langle v_x \rangle$  and  $\langle (v_x - \langle v_x \rangle)^2 \rangle^{1/2}$  give similar trend, where  $\langle v_x \rangle \neq 0$  at  $\Delta x = 0$  is because the trapped bubbles at the left lower corner further biased the flow in the system. The turbulent flow in the system can never be completely symmetric. The asymmetry of the foot of the soap film, i.e. some trapped bubbles at one side, and different thermal contact at the two lower corners of the film, can cause the flow to lose symmetry. Nonetheless, the functional forms of the SP velocity statistics are weakly affected by those small perturbations as seen in Fig. 5-4.

Convection patterns as shown in Fig. 5-1 strongly indicate that velocity fluctuations in the center of the cell are affected by plumes ejected from the bottom of the cell, and thus may carry the signature of plume statistics. To quantify such an observation, emission properties of plumes are investigated with a focus on their speed and the emission interval distributions. Shadowgraph video images were acquired at 30 frames per second, and the emission statistics were measured directly from the video images.

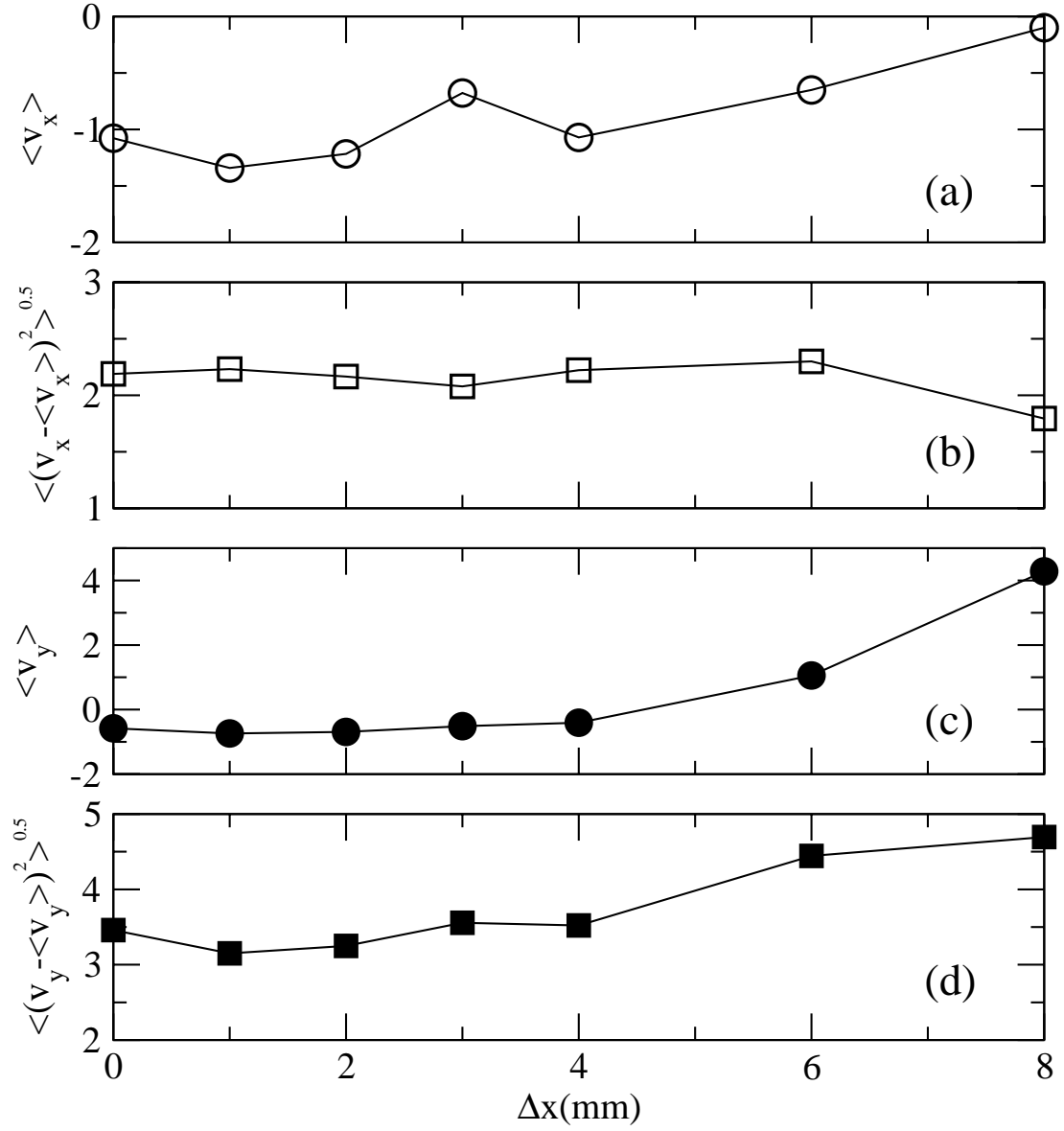


Figure 5-5: Local mean flow  $\langle v_x \rangle$  (a),  $\langle v_y \rangle$  (c), and the local fluctuations  $\langle (v_x - \langle v_x \rangle)^2 \rangle^{1/2}$  (b),  $\langle (v_y - \langle v_y \rangle)^2 \rangle^{1/2}$  (d) as a function of distance  $\Delta x$ . The distance  $\Delta x$  is defined as  $\Delta x = 0$  at the middle of the film and  $\Delta x = 1$  cm at the right side wall.

We noted that the shadowgraph techniques are also commonly used in 3D convection to visualize the fluid motion [77]. However, in 2D convection, individual plumes can be followed more closely than in 3D. This set of measurements differs from the LDV data reported above in that individual plumes are isolated and thus the measurements are untainted by the background fluctuations. Figure 5-6 (a) displays the plume statistics at  $\Delta T=36$  K. We noted that the PDF for the initial plume velocity,  $v_{\text{plume}}$ , is strongly peaked at  $\langle v_{\text{plume}} \rangle \sim 3.5$  cm/s with a broad tail stretching up to  $5\langle v_{\text{plume}} \rangle$ . The weak plumes with  $v_{\text{plume}}$  less than  $\langle v_{\text{plume}} \rangle$  are rare, and their distribution drops sharply. The kinetic energy contained in plumes is thus strongly intermittent, similar to earthquakes [78]. In fact the tail part of the distribution function for  $v_{\text{plume}}$  can be approximated by an exponential function  $P(v_{\text{plume}}) \sim \exp(-v_{\text{plume}}/v_{p0})$ , as indicated by the solid line in the figure. The inverse of the slope gives the typical fluctuations in the plume velocity  $v_{p0}$ , which turns out to be  $v_{p0}=3.3 \pm 0.2$  cm/s, comparable to the mean speed of the plumes.

Likewise, we also measured the rate of emission statistics, which is displayed in Fig. 5-6(b). The emission rate is highly peaked with sharp drops in both sides of PDF.

So far, all of our investigations have been concentrated on velocities at certain heights of the cell. How does the velocity change as a function of the vertical position  $y$ ? For strongly stratified fluid, the convection is dominated by emission of plumes that effectively mix the fluid in the lower part of the cell, which we define as a mixing zone as illustrated in Fig. 5-1. Naively, therefore, one would expect that velocity fluctuations along the  $y$  direction are more intense at the bottom of the cell and decrease upwards. However, we will show below this intuition is incorrect. Moreover, since convection in our system is strongly compressible, the mean velocity at any given height  $y$  may not vanish.

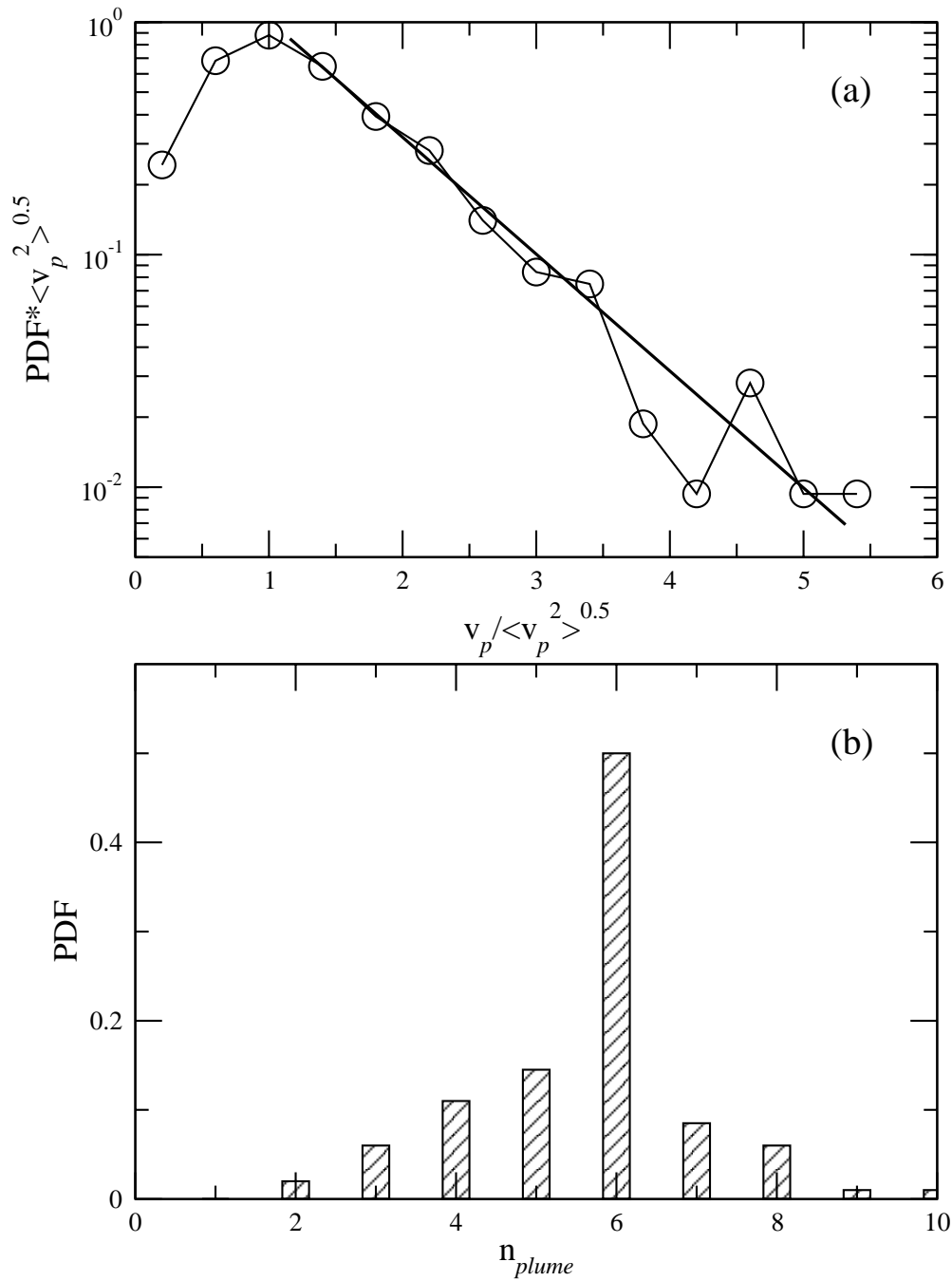


Figure 5-6: Plume Emission Statistics in 2D Convection. The plume velocity (a) and the emission rate  $n_{plume}$  (number of emitting plumes per 33 ms) (b) were measured using consecutive shadowgraphs similar to the ones shown in Fig. 5-1. The measurements were taken when an incipient plume just emerges from the lower thermal boundary layer.

This can be seen by imposing the condition of mass conservation  $\partial\rho/\partial t + \nabla \cdot (\rho\vec{v}) = 0$  instead of the two dimensional incompressible condition  $\nabla_2 \cdot \vec{v} = 0$ . Performing the integration over the 3D volume and applying the Gauss law, it is found that the time averaged total fluid mass within the film  $I = \langle \int (\partial\rho/\partial t + \nabla \cdot (\rho\vec{v}))dV \rangle = \langle \oint \rho\vec{v} \cdot \vec{n}ds \rangle = 0$ , where  $s$  is a surface element oriented at  $\vec{n}$ , the  $\langle \rangle$  is the time average. The first integral is performed over the volume of the film, which is vertically from a given height  $y$  up to the film top boundary and horizontally across two side walls. The Gauss law is used to rewrite the volume integral in terms of the surface integral, in which the  $\partial\rho/\partial t$  contribution vanishes for a steady state. The integral  $I=0$  should be true after ensemble average. The fluxes on the top, the side edges, and the two free surfaces of the film are zero, thus one ends up with the integration along the lower cross section area  $I = \int \rho_0 \langle h(x,y)v(x,y) \rangle dx = 0$  in steady state. Therefore, for a uniform mass distribution (or an incompressible fluid),  $h(x,y)=\text{const}$ , the integration along the lower edge is the horizontally averaged vertical velocity  $\langle v_y(y) \rangle \equiv \langle \int v(x,y)dx \rangle$  and is zero as expected. For a compressible fluid such as ours,  $I=0$  implies that  $\langle v_y(y) \rangle$  is not necessarily zero and will, in general, depend on  $y$ . A simple calculation shows that  $\langle v_y(y) \rangle = -\langle h(y) \rangle^{-1} \int \langle \delta h(x,y)v_y(y) \rangle dx$  is negative if the ascending plumes carries more fluid mass per unit area than the average mass density  $\langle h(y) \rangle$ . Likewise, if the descending plumes carry more fluid mass than the average,  $\langle v_y(y) \rangle$  will be positive. Measurements of  $\langle v_y(y) \rangle$  at different  $y$  strongly support the above analysis as seen in Fig. 5-7(a). Notice that we are in the process of using two different meanings of the symbol “ $\langle v_y \rangle$ ”. The first  $\langle v_y \rangle$  appearing in the SP velocity denotes a time averaged velocity component  $v_y$  along  $y$  direction at a fixed measuring spot. The second  $\langle v_y \rangle$  or  $\langle v_y(y) \rangle$  denotes the mean velocity along  $y$  direction averaged in a given horizontal layer from one side wall to another side wall at height  $y$ .

A conspicuous finding of this experiment is that despite small  $\langle v_y(y) \rangle$  seen in Fig. 5-7(a), the variance of the velocity is far greater. Figure 5-8(a) shows a set of velocity variances measured at different temperature difference  $\Delta T$ s (See Fig. 5-8 captions for details). We noted that the normalized variance  $\langle v_y^2 \rangle / v_{y\text{max}}^2$  are not a monotonic function of  $y$  but increases and then decreases with height. The variance  $\langle v_y^2 \rangle / v_{y\text{max}}^2$  thus attain a maximum value at a certain height  $y_p$  for a given  $\Delta T$ .

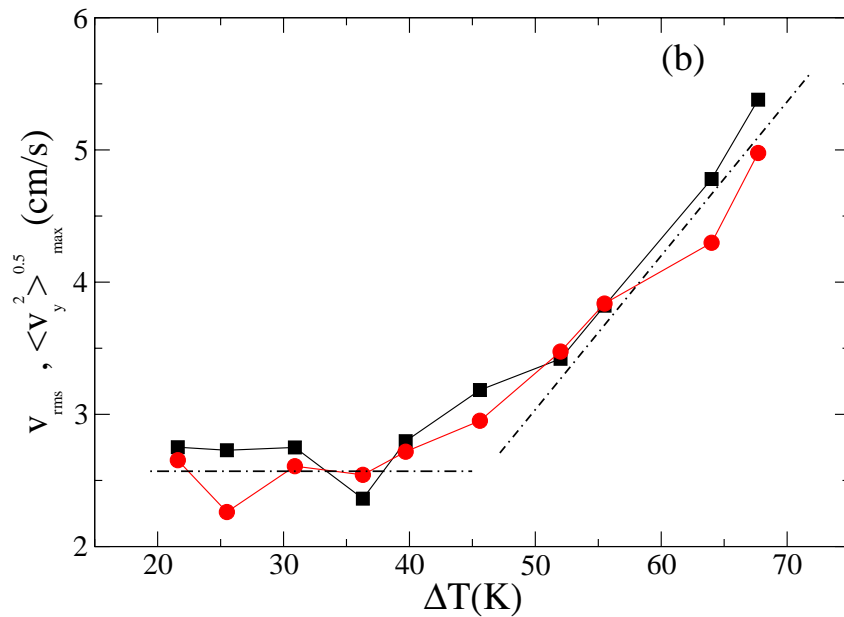
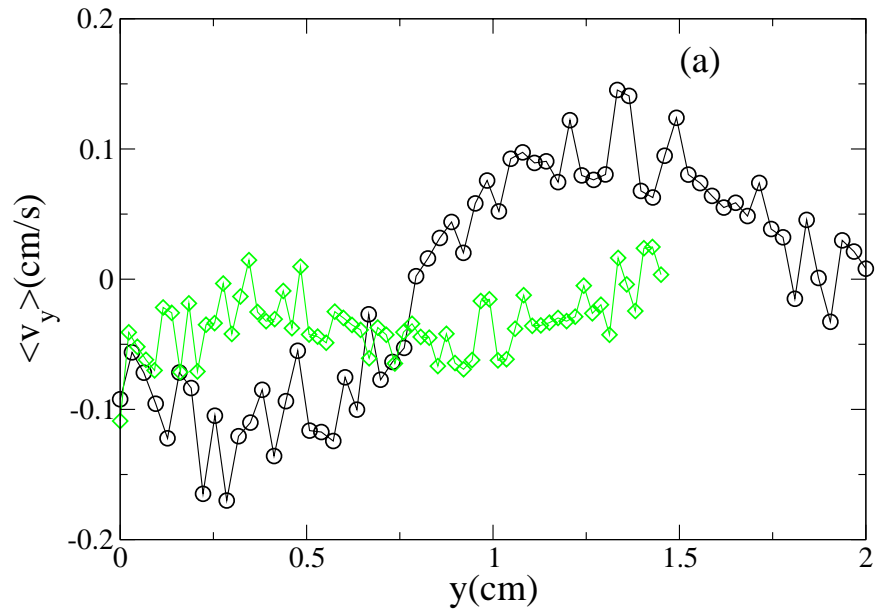


Figure 5-7: (a)  $\langle v_y \rangle$  as a function of vertical height  $y$ . Here  $\langle \rangle$  stands for the assemble average over a horizontal layer with same height  $y$  in one velocity field and then average over all velocity fields. Only two temperature differences,  $\Delta T=67.7$  K (circles) and  $\Delta T=25.5$  K (diamonds), are plotted to illustrate  $\langle v_y \rangle \neq 0$ . Other  $\Delta T$ s show similar behavior. (b) The  $v_{rms}$  (black squares) and  $\langle v_y^2 \rangle_{max}^{0.5}$  (red circles) as a function of  $\Delta T$ . The dot dashed line is guide to the eye.

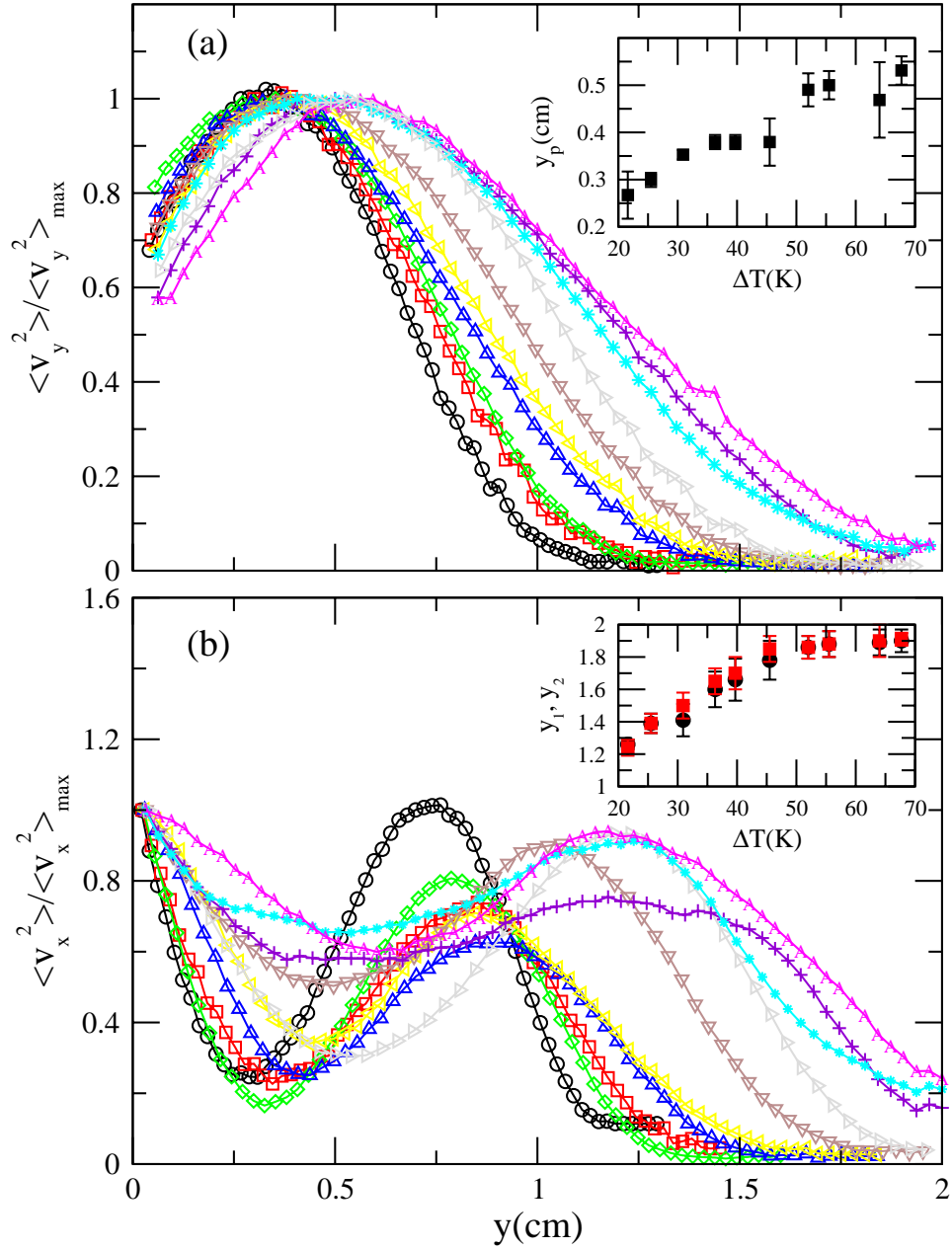


Figure 5-8: (a)  $\langle v_y^2 \rangle^{1/2} / \langle v_y^2 \rangle_{\max}^{1/2}$  and (b)  $\langle v_x^2 \rangle^{1/2} / \langle v_x^2 \rangle_{\max}^{1/2}$  vs. height  $y$ .  $\langle \rangle$  indicates the ensemble average of a horizontal layer at a height  $y$  at a  $\Delta T$ . The inset in (a) is a plot of  $y_p$  (peak of  $\langle v_y^2 \rangle^{1/2} / \langle v_y^2 \rangle_{\max}^{1/2}$ ) vs.  $\Delta T$ . The inset in (b) plots  $y_1$  (black color, max  $y$  of  $\langle v_y^2 \rangle^{1/2} / \langle v_y^2 \rangle_{\max}^{1/2}$ ) and  $y_2$  (red color, max  $y$  of  $\langle v_x^2 \rangle^{1/2} / \langle v_x^2 \rangle_{\max}^{1/2}$ ) vs.  $\Delta T$ . Different symbols in (a-b) represent  $\Delta T=21.6$  (circle), 25.5 (square), 30.9 (diamond), 36.3 (triangle-up), 39.7 (triangle-left), 45.5 (triangle-down), 52 (triangle-right), 55.5 (star), 64 (plus) and 67.7 K (A).

A plot of  $y_p$  as a function of  $\Delta T$  in the inset of Fig. 5-8(a) shows that  $y_p$  increases with  $\Delta T$ ; indicating plumes gain more KE energy as  $\Delta T$  raises and are able to ascend to greater heights. A similar conclusion can also be drawn from the spread of  $\langle v_y^2 \rangle / v_{y\max}^2$  in the vertical direction. For small  $\Delta T$ ,  $\langle v_y^2 \rangle / v_{y\max}^2$  is essentially zero at the top part, indicating the boundary  $y_1$  (or  $y_2$ ) of the mixing zone. As  $\Delta T$  increases,  $y_1$  increases and eventually reaches the top of film at  $\Delta T \sim 45.5 \pm 3$  K as displayed in the inset of Fig. 5-8 (b). The smallness of  $\langle v_y^2 \rangle / v_{y\max}^2$  near the upper boundary are expected because velocity there is predominantly horizontal. The formation of LSC is the extreme form of horizontal “wind” near the boundaries. The similar boundary effect can also be recognized from  $\langle v_x^2 \rangle / v_{x\max}^2$  in Fig. 5-8 (b).

It is also interesting to examine the dependence of  $v_{y\max}$  on  $\Delta T$  because it is a measure of the KE of the system or the turbulence intensity. Surprisingly, we found that  $v_{y\max}$  is nearly independent of  $\Delta T$  for small temperature difference ( $20 < \Delta T < 45$  K) and increases monotonically for large temperature difference ( $\Delta T \geq 45$  K), as represented by red circles in Fig. 5-7(b). The overall turbulent intensity can also be characterized by the root-mean-square fluctuations of velocity  $v_{\text{rms}}$  of the whole film. The  $v_{\text{rms}}$ , plotted using black squares in Fig. 5-7(b), has a similar dependence with the  $\Delta T$  as the  $v_{y\max}$ .

The above observations allow us to draw an important conclusion concerning the interaction between a turbulent field and an active scalar field with a constant exchange of energy between these two fields. In our system the 2D density (thickness fluctuation) field is such a scalar field that stores gravitational PE. Our experiment shows that the net energy input is expended to overcome PE of the stratification, while maintaining the constant KE of overall turbulent fluctuations. The height of the lower turbulent region expands as  $\Delta T$  increases. Once this region occupies the whole film, PE is saturated and then KE begins to increase with further increase of  $\Delta T$ . In our soap film, the above scenario corresponds to the condition where individual plumes are able to climb the top of the film, triggering a LSC which switches randomly from clockwise to counter-clockwise in the time scale of a second. Thus, the constancy of  $v_{\text{rms}}$  is a result of the interaction between the gravitational PE and the turbulent KE. The active scalar field serves as an energy buffer with a finite capacity. An analogue is the melting of ice, i.e.,  $v_{\text{rms}}$  resembles, phenomenologically, the melting temperature of the ice. When a system

undergoes a phase transition such as ice melting process, the input energy does work to break the water molecular bound in ice while keeping Gibbs free energies of the ice and the water to be same [36]. Thus, during the ice melting, the melting temperature is constant until all ice has melted. Our result may have general implications because couplings of the turbulence to another field are common. Elastic deformation of polymer chains and cavitations in strongly compressible fluids are just a few examples [79].

The second point we would like to make concerns input and output statistics of turbulence. It is generally believed that in fully developed turbulence a single-point velocity distribution is Gaussian, resulting from random accelerations integrated over some finite time [75]. However, this Gaussian behavior was called into question by the theoretical analysis of Falkovich and Lebedev (FL) [75]. FL proposed that due to nonlinear interactions in turbulent flow, there should be correlations between velocity ( $v$ ) fluctuations and force ( $f$ ) fluctuations. Such correlations manifest themselves most strongly for rare events, i.e. large deviations from the mean events. In the special case of Gaussian random forcing on large scales, the single-point velocity pdf was found to be  $P(v) \propto \exp(-(v/v_{rms})^n)$  [75]. Here, the exponent  $n$  depends on the time scale  $\tau$  of forcing. If  $\tau$  is much smaller than the typical eddy turn over time  $t^* \sim l_0/v$ ,  $v$  growth relates to  $f$  as  $v^2 \sim f^2 \cdot \tau \cdot t^* \approx f^2 \cdot \tau \cdot t^*$ , which gives  $v^3 \sim f^2 \cdot \tau \cdot l_0$  corresponding to  $n=3$ . Here  $l_0$  is the typical eddy size. In the opposite limit,  $\tau \gg t^*$ ,  $v$  grows linearly with  $f$  until  $t^*$  as  $v \sim f \cdot t^* \approx f \cdot t^*$ , which yields  $v^2 \sim f \cdot l_0$ , producing  $n=4$ . In either case tails of velocity pdf decay faster than Gaussian and are called sub-Gaussian behavior.

In thermal convection, thermal plumes are closely related to energy and momentum input of system. In our vertical soap film, the role of thermal plumes becomes even more important due to the stable stratification. One simple clue comes from the SP velocity pdf for  $v_y > 0$  is close to exponential PDF of plume injection speed. Thus, we believe that the SP velocity statistics, especially for large velocity fluctuations, may relate to the large tail part of the plume statistics. By observing the video image of flow motion, one finds that the plume rises from the boundary and enters into the mixing region with almost constant speed. This suggests a rough balance between buoyancy force, which is the driving force of the plume, and its neighboring shears. The observation thus leads our following assumption. The assumption is that

plumes with large velocity produce an effective shear force to the fluid as  $f \sim \alpha v_p$ . Here  $v_p$  is plume velocity and  $\alpha$  is an unknown drag coefficient. It then follows, based on the theoretical consideration of FL, that the single-point velocity PDF is given by  $v^2 \sim f^2 \tau t^*$ . In the above we have assumed that forcing (or acceleration) is random and acting on a short time scale  $\tau$ . Our observation shows that the typical eddy turn over time  $t^* \approx 2\pi(L/2)/v_{\text{rms}} \sim 1$  s and the plume emission interval  $\tau \approx 0.2$  s. The above  $t^*$  and  $\tau$  give the ratio  $t/\tau \gg 1$ , which satisfies the short-time limit in FL theory. Since  $t^* \sim L/v$ , we find  $v^3 \sim f^2 \tau L$ , where  $L$  is the typical size of an eddy, which is the height of the mixing zone. The exponential distribution of  $f$  thus implies that the single-point velocity PDF is given by  $P(v) \sim \exp(-\beta(v/v_{\text{rms}})^{3/2})$ , where  $\beta$  is a coefficient. This super Gaussian form (exponent  $n=3/2$ ) explains what we have seen in Fig. 5-2 to Fig. 5-4, in which  $P(v_y > 0)$  can be treated as a superposition of the plume statistics, exponential form, and the super Gaussian form (dot lines). Only exponential tail is seen in the measurements because that  $\exp(-\beta(v/v_{\text{rms}})^{3/2})$  decays much faster than exponential form.

Although our results showed an agreement between the single-point velocity statistics and a predicted super-Gaussian form from the FL theory, the agreement still could be just coincidental because of the prerequisite assumption of the linkage between plume speed and forcing term, which is very hard to justify. The data plotted in Fig. 5-2 to Fig. 5-4 were acquired at low  $\Delta T$ s with the absence of LSC. The plume speed measurement in a regime absent of LSC is in principle still feasible. However, in the LSC dominant regime, this type of measurement using shadow graph is extremely difficult. The single point velocity measurement is still as easy as in the low  $\Delta T$  regime. Figure 5-9 demonstrates a set of single point velocity PDF in the presence of LSC. The super Gaussian form nevertheless persists! Presumably, the plume speed histogram should have an exponential form, which we are, unfortunately, unable to verify using current experimental method. To our knowledge, the FL theory has not been investigated systematically in any laboratory experiment but was only referred in a computer simulation for the passive-scalar turbulence [80]. Nonetheless, the FL theory is very profound, as it provides a practical mean to examine an output (single-point velocity) statistics, which is usually difficult to obtain, based up an input (or forcing) statistics, which can be readily measured by LDV or PIV.

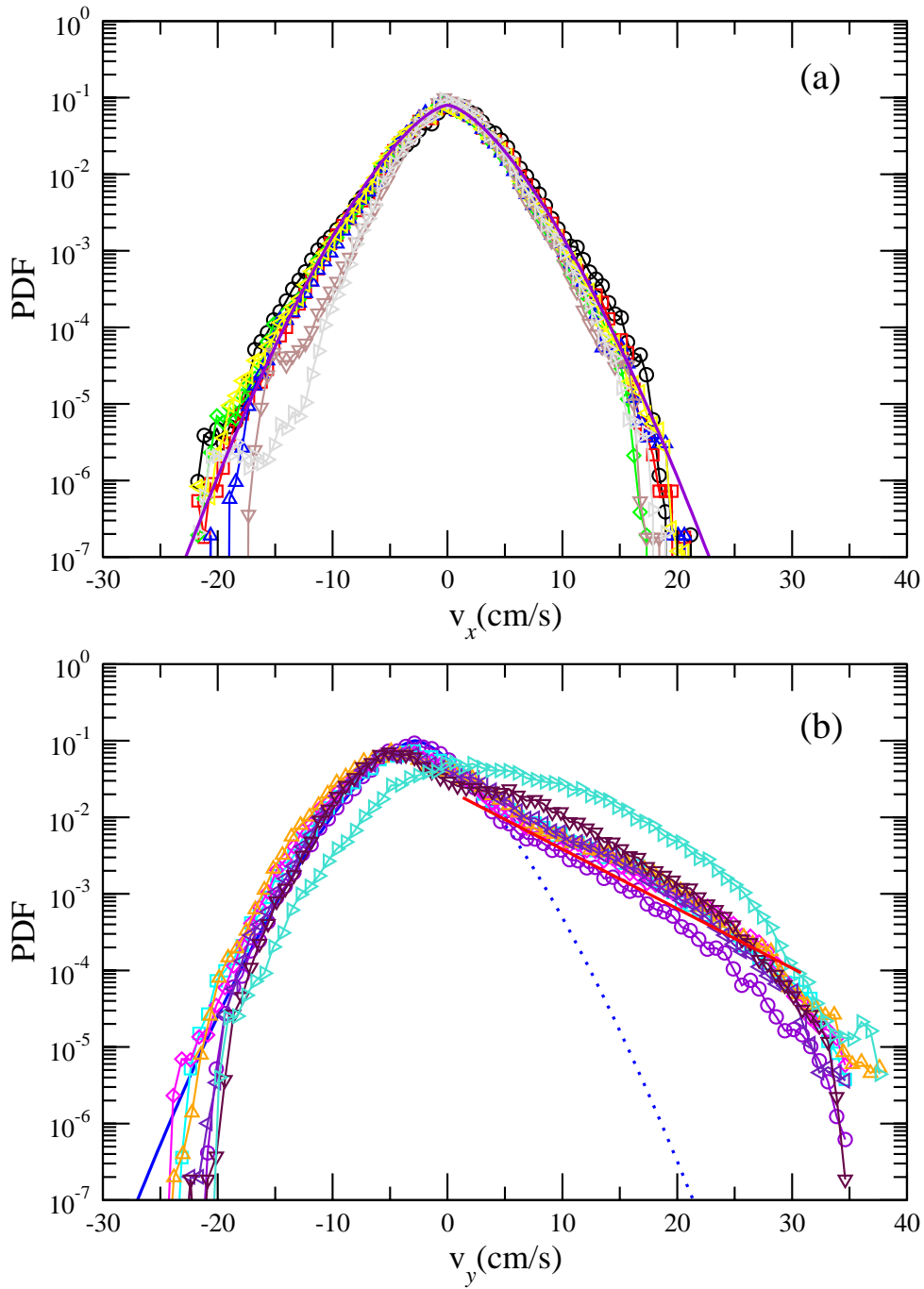


Figure 5-9: Single point velocity PDF measured in a square geometry at  $\Delta T=70-14.3=55.7$  K with large scale circulations. Different symbols stand for different measurement spots away from the center of the cell, circles (0 mm), square (1 mm), diamond (2 mm), triangle-up (3 mm), triangle-left (4 mm), triangle-down (6 mm) and triangle-right (8mm).

#### 5.4. Summary

To summarize, we have found that in strongly stratified vertical soap film convection, turbulent fluctuations are strongly anisotropic and manifest themselves in the velocity statistics. In particular, the single point velocity statistics shows a super Gaussian form, which can be explained using a theory developed by Falkovich and Lebedev. Another finding is the buffering effect of turbulence intensity with a control parameter  $\Delta T$ . It remains an intriguing possibility that such an effect is general and should manifest itself in strongly coupled systems where kinetic energy can be readily shuffled between turbulence and another active field.

## 6. Velocity Intermittency in a Buoyancy Sub-range

### 6.1. Abstract

In a two-dimensional soap film convection experiment, the velocity fields were found to be strongly intermittent in the buoyancy sub-range, which was reported to be non-intermittent in a recent numerical simulation. The longitudinal velocity structure functions  $S_q(l) (= \langle |\delta v_l|^q \rangle)$  exhibit self-similar structures and can be described by power laws  $l^{\zeta_q}$  for integers  $1 \leq q \leq 8$ . By extending Kolmogorov's refined similarity hypothesis to our system, an analytical form is derived for the scaling exponent  $\zeta_q = q/2 + (\mu/18)(3q - q^2)$ . Our measurements yield  $\mu = 0.42$ , which is significantly greater than 0.2 found in high-Reynolds number turbulence in wind tunnels.

### 6.2. Introduction

Intermittency in barotropic turbulence has long been recognized and investigated intensely by theory and experiment [62]. In contrast, the problem has received little attention for buoyancy driven turbulence. The fundamental difference between these two types of turbulence was established due to Bolgiano who studied turbulence in the earth's atmosphere [27, 28]. An important feature of Bolgiano's theory is the interaction between gravitational potential energy (PE) and turbulent kinetic energy (KE). For large scales, called the Bolgiano regime (BR), such coupling is sufficiently strong that the Kolmogorov  $k^{-5/3}$  law gives way to a new scaling for the energy spectrum  $E(k) \sim k^{-11/5}$ . While the Bolgiano's theory has succeeded in explaining low-order correlations of velocity and density fields, it leaves the intermittency issue untouched. Recent experiments and computer simulations have left little doubt that scalar fields are strongly intermittent, but the same cannot be concluded for velocity statistics [31, 81]. In a recent numerical simulation, velocity statistics in the BR were found to be non-intermittent [23], whereas intermittency were reported in Rayleigh-Bénard convection (RBC) in a water tank [82]. Since the simulation was performed in a two-dimensional (2D) geometry, it is unclear if the lack of intermittency is due to the particular spatial dimension used or it is a generic feature of

convective turbulence. The issue is of considerable interest in that all 2D experiments reported to date showed no sign of intermittency on large scales [83].

In this study it is demonstrated that in a 2D soap film driven by a temperature gradient, the velocity fields on large scales exhibit strong spatiotemporal fluctuations. Specifically, the velocity structure functions  $S_q(l) = \left\langle \left| \left( \bar{\mathbf{v}}(\bar{\mathbf{r}} + \bar{\mathbf{l}}) - \bar{\mathbf{v}}(\bar{\mathbf{r}}) \right) \cdot \bar{\mathbf{l}} / l \right|^q \right\rangle (= \langle |\delta v_l|^q \rangle)$  exhibit self-similarity and can be characterized by a power law  $S_q(l) \sim l^{\zeta_q}$ , where  $\delta v_l$  is the longitudinal velocity difference on scale  $l$  and  $q$  is an integer. The fluctuation is also strongly intermittent in that the exponent  $\zeta_q$  deviates strongly from linear  $q$  dependence. Using a random-cascade model and assuming a lognormal distribution for the energy flux,  $\zeta_q$  was calculated and found to be in excellent agreement with the measurement. The large velocity fluctuation arises because of a strong gravity-induced density gradient ( $\Delta\rho_2/\rho_2 \sim 30\%$ ) in the film, where  $\rho_2$  is the 2D density. The stratification in our system is  $\sim 30$  times greater than those typically attained in RBC in water and is equivalent to  $\sim 7$  km in atmospheric height. A significant finding of this experiment is that flow intermittency takes place concurrently with the inverse energy cascade. This is rather surprising, considering that enstrophy is not strictly conserved in a stratified fluid. The inverse energy cascade, from small to large scales, precludes the classical interpretation of intermittency, i.e. the spottiness of the energy dissipation at small scales. Our experiment suggests that in turbulent convection, the source of the intermittency is the coupling of the two energy sources, the KE and the PE. By certain measures, which we discuss in the summary, the intensity of intermittency in our film is stronger than those observed in barotropic turbulence with very high Taylor micro scale Reynolds numbers,  $Re_\lambda > 500$  [84].

### 6.3. Experimental Method

Our experiment was carried out in a convection cell, which is described in a detail in previous chapters. In this experiment, velocity differences  $\delta v_l$  on scales  $l$  were measured using two laser Doppler velocimeters. The measurement positions are deliberated in Fig. 6-1. The diameter of the laser beam focus is  $33 \mu\text{m}$  and its value determines the spatial resolution of  $l$ . The data rate was  $\sim 10^4$  per second, and the coincidence window was set to be  $50 \mu\text{s}$ . The measured  $\delta v_l$  is therefore free of a frozen-turbulence assumption.

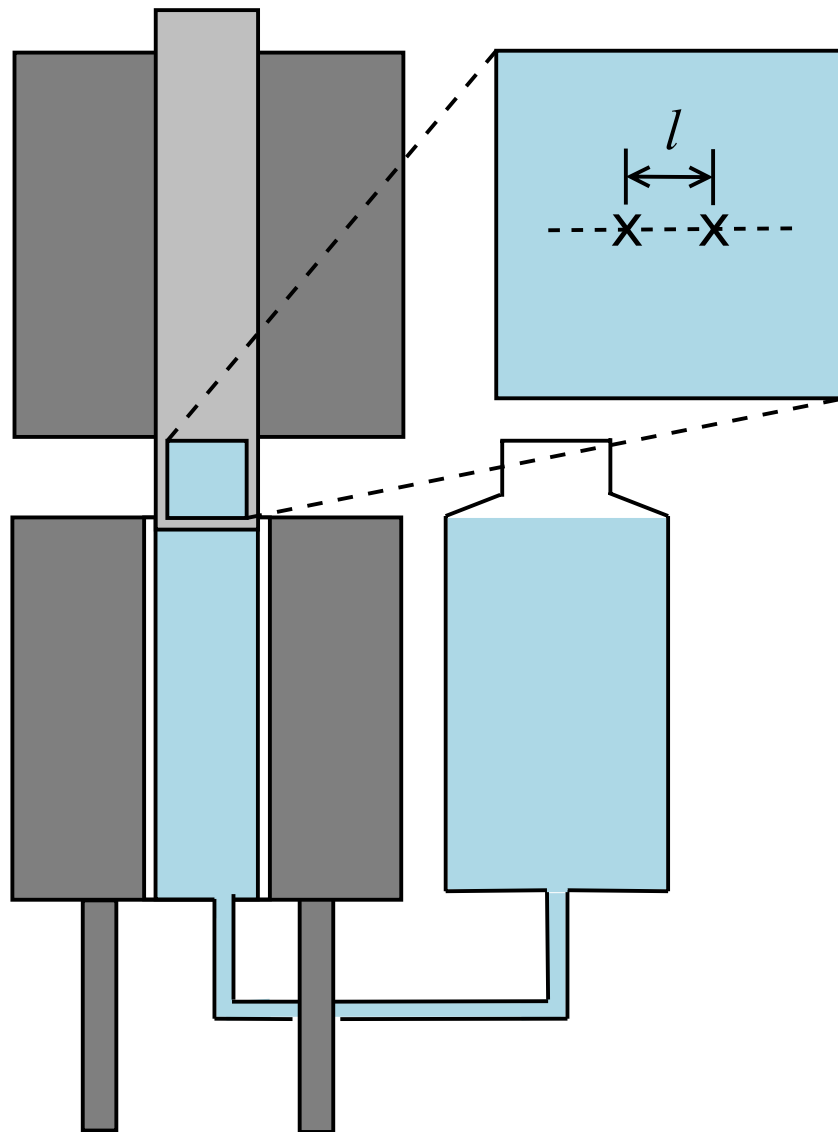


Figure 6-1: The experimental setup. The film is sandwiched between two aluminum blocks and is in contact with a soap-solution reservoir. The velocity difference  $\delta v_l$  is measured by two LDV probes at locations indicated by two “X” on the sketch to the upper right. Only the horizontal component of the velocity is measured.

## 6.4. Experimental Results

This study focused on turbulent convection with a large temperature gradient  $\Delta T=63.5$  K. The large  $\Delta T$  causes intense velocity and density fluctuations that are nearly isotropic. Figure 6-2(a) shows a set of measurements for the probability distribution functions (pdf)  $P(\delta v_l)$ , each containing  $>10^6$  data points. The separation distance was varied from 120 to 14,000  $\mu\text{m}$ , covering two decades in  $l$ . As can be seen, the pdf tails are highly non-Gaussian for all  $l$ , and there is also a change in the shape of the pdf as  $l$  was varied. For small scales,  $l < 1440$   $\mu\text{m}$ , the flanks of pdf consist of two tails; a fast and a slow decay. However, for large scales,  $l > 1440$   $\mu\text{m}$ , only the slow decay remains. Thus, there is a typical scale  $l_C \sim 1400$   $\mu\text{m}$  that separates these two different set of pdf's. As will be discussed below,  $l_C$  may be identified as the Bolgiano scale  $l_B$  of the system. For all runs, the background fluctuations are surprisingly Gaussian-like as suggested by the rounded top of the pdf's; this is the case even for  $l$  as small as 120  $\mu\text{m}$ . This behavior is different from barotropic turbulence where the top sharpens rapidly as  $l$  decreases towards the Kolmogorov dissipative scale [62]. This observation indicates that even for  $l \sim 10^2$   $\mu\text{m}$ , velocity fluctuations are still active in the soap film.

Using these pdf's, the velocity structure functions  $S_q(l) = \langle |\delta v_l|^q \rangle$  were calculated for different  $q$ . Of particular interest is  $S_2(l)$ , which is related to the energy spectrum  $E(k)$ , with the wavenumber  $k=1/l$ . Figure 6-2(b) shows that  $S_2(l)$  obeys a power law  $S_2(l) \sim l$  on large scales ( $10^3 < l < 10^4$   $\mu\text{m}$ ), spanning a decade of  $l$ . This scaling corresponds to  $E(k) \sim k^{-2.0 \pm 0.1}$  and compares favorably with the Bolgiano's prediction  $E(k) \sim k^{-11/5}$ . For  $l > 10^4$   $\mu\text{m}$ ,  $S_2(l)$  levels off and becomes independent of  $l$ , which is expected because of the finite system size ( $L=2$  cm). The rounding on small scales was also observed, suggesting that for  $l < 10^3$   $\mu\text{m}$ , turbulence is no longer driven by buoyancy. The crossover from the buoyancy dominated to the KE dominated fluctuations is marked by the Bolgiano scale  $l_B = 2\pi(\chi_\rho^{3/4}(g/\rho_2)^{3/2}/\varepsilon^{5/4})^{-1}$  [28], where  $\chi_\rho$  is the mean-squared density fluctuation rate (assumed to be a constant),  $g$  is the gravitational constant,

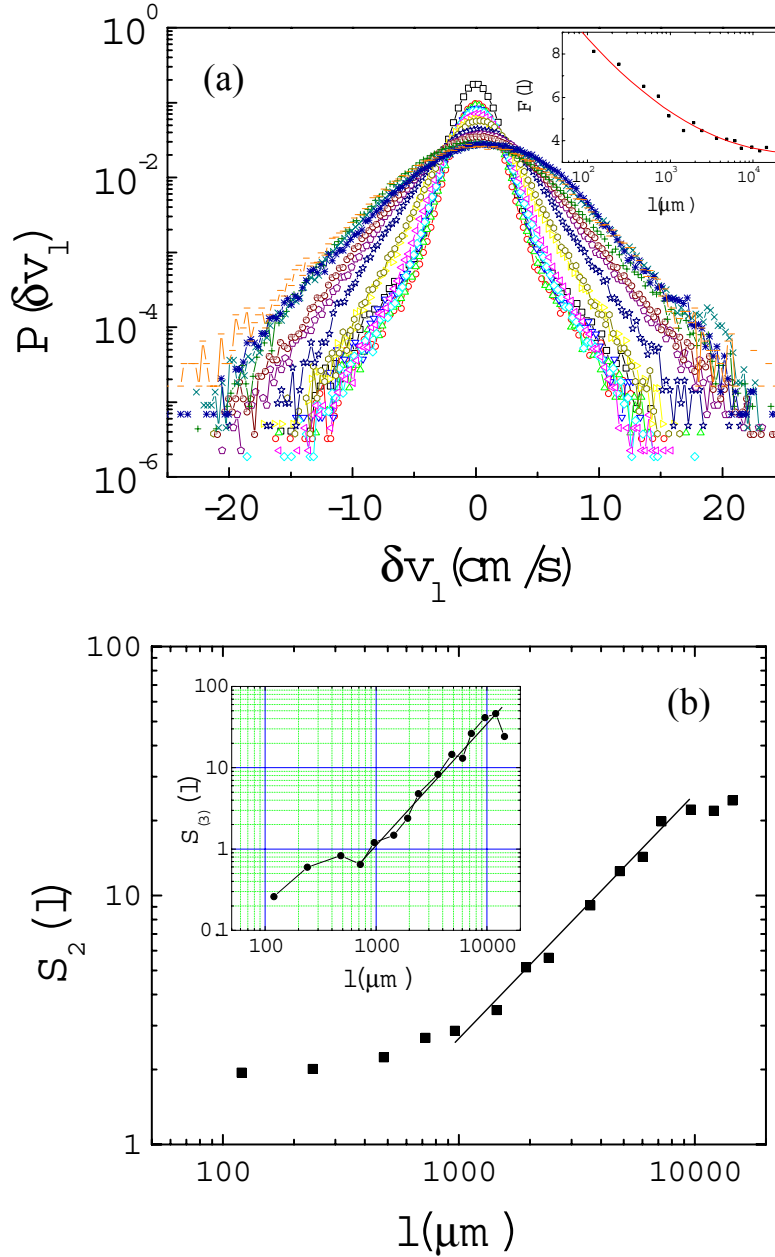


Figure 6-2: (a) The velocity-difference pdf's  $P(\delta v_l)$  as a function of  $l$  (in  $\mu\text{m}$ ), 120 (squares), 240 (circles), 481 (up triangles), 721 (down triangles), 962 (diamonds), 1442 (left triangles), 1923 (right triangles), 2404 (hexagons), 3606 (stars), 4808 (pentagons), 7212 (pluses), 9616 (crosses), 12020 (asterisks). The inset is the flatness  $F(l)$  as a function of  $l$ . The solid line is a guide to the eyes. (b) The log-log plot of  $S_2(l)$ . The line indicates a power-law  $S_2(l) \sim l$  in the Bolgiano regime ( $10^3 < l < 10^4 \mu\text{m}$ ). The inset is a plot of  $S_{(3)}(l) (= \langle \delta v_l^3 \rangle)$ , showing  $S_{(3)}(l) \sim l^{1.5}$ . The  $S_{(3)}(l) > 0$  indicates that there is an inverse energy cascade in our system.

and  $\varepsilon$  is the kinetic energy injection rate. For our system, a simple calculation showed that  $l_B \sim 2600 \text{ } \mu\text{m}$  [85], which is consistent with the rounding of  $S_2(l)$  for small scales and the crossover length  $l_C$  seen in Fig. 6-2(a).

In a 2D system, it is generally believed that the energy cascade direction is reversed; the energy flux is from small to large scales. However, the situation is not clear in the presence of density stratification, where enstrophy is not strictly conserved. We measured the 3<sup>rd</sup> moment of the velocity increment  $S_{(3)}(l) = \langle \delta v_l^3 \rangle$ , which gives the scale-by-scale energy flux. Here the subscript notation (3) is used to distinguish the 3<sup>rd</sup> moment calculated without the absolute sign. As shown in the inset of Fig. 6-2(b),  $S_{(3)}(l)$  is positive for  $10^3 < l < 10^4 \text{ } \mu\text{m}$ , indicating an inverse energy cascade in the BR. The data shows a power law  $S_{(3)}(l) \sim l^{-1.5}$  over about a decade in  $l$ . We note that the scaling laws for  $S_{(3)}(l)$  and  $S_2(l)$  are consistent with  $S_{(3)}(l) \sim S_2(l)^{3/2}$ . Furthermore, since  $S_{(3)}(l) \sim \varepsilon_l l$ , the kinetic energy dissipation  $\varepsilon_l$  is not scale invariant [48] but depends on  $l$  as  $\varepsilon_l \sim l^{1/2}$ .

An important question regarding the above measurements is whether the velocity fluctuations are isotropic. We answered this question by measuring the 2D spectrum  $E(k_x, k_y)$  using particle imaging velocimetry. A typical velocity field and  $E(k_x, k_y)$  are shown in Fig. 6-3(a) and 3(b). The latter was calculated based on 200 velocity fields. For  $\Delta T = 63.5 \text{ K}$ , the flow self-organizes and forms a large scale circulation (LSC), which homogenizes velocity fluctuations on small and intermediate scales. As shown in Fig. 6-3(b),  $E(k_x, k_y)$  consists of concentric rings over a range of wavenumbers,  $1 < k < 10.5 \text{ cm}^{-1}$ . Only for small wavenumbers,  $k < 1 \text{ cm}^{-1}$ , does the spectrum become anisotropic and elongated along the vertical direction. This large-scale anisotropy is consistent with buoyancy driven turbulence; the largest vortex is squashed vertically due to stratification, giving rise to a longer correlation length in the horizontal direction.

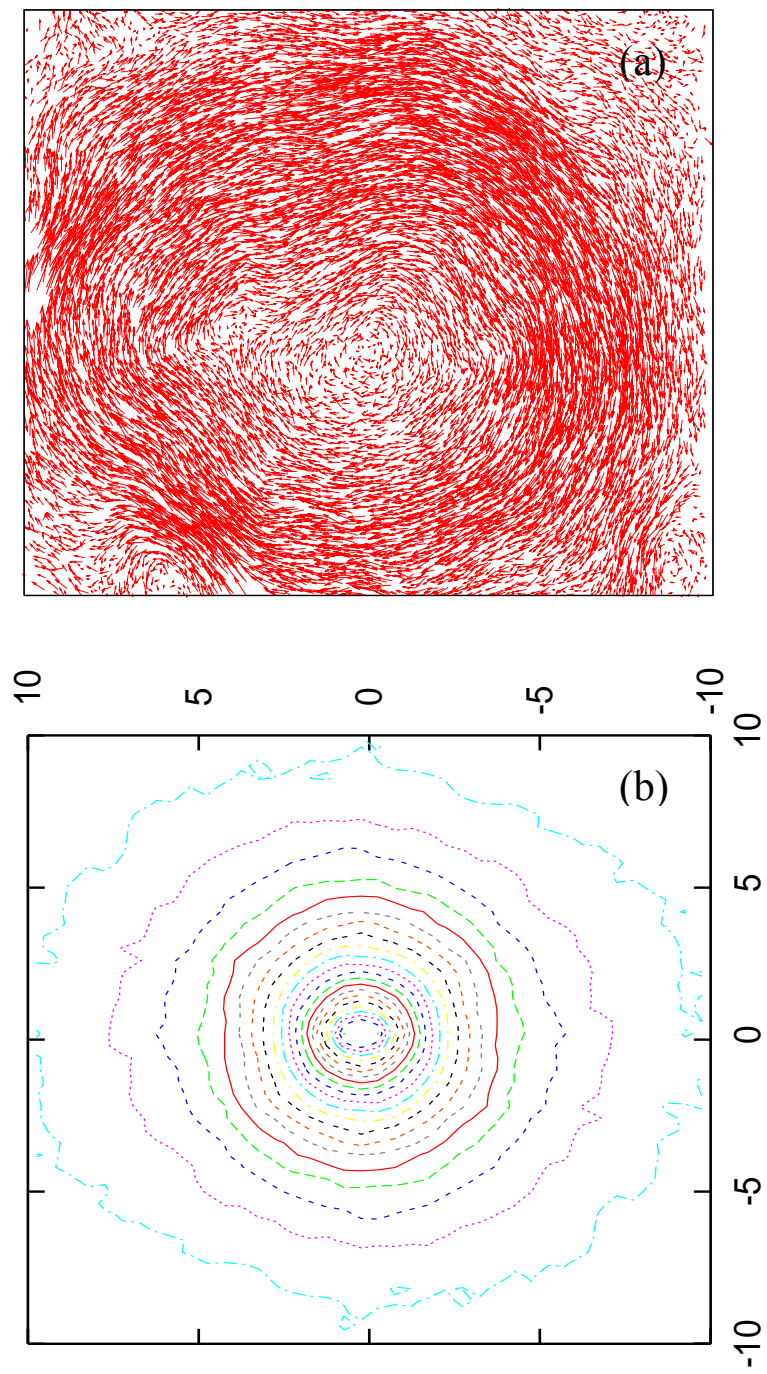


Figure 6-3 (a): A typical velocity field measured by PIV at  $\Delta T=63.5$  K. The presence of a LSC is evident. The velocity field is isotropic as indicated by the 2D energy spectrum  $E(k_x, k_y)$  in (b). The division in the horizontal and vertical axes is  $\Delta k_x = \Delta k_y = 5 \text{ cm}^{-1}$ .

After identifying a range of scales where Bolgiano scaling is approximately valid and fluctuations are nearly isotropic, we next investigate intermittent velocity fluctuations on large scales  $l \geq l_B$ . This is a significant issue because unlike barotropic turbulence there is no consensus on whether 2D turbulent convection is intermittent [83]. If intermittency is indeed present and strong enough, it could alter the Bolgiano scaling law for  $S_2(l)$  [49, 86]. The problem is also interesting because it has been postulated [83] and observed [87] that 2D turbulence on large scales is not intermittent. Flow intermittency reveals itself in different manners and can be analyzed with different levels of sophistication. An inspection of  $P(\delta v_l)$  in Fig. 6-2(a) shows that the flow is intermittent because most pdfs decay slower than Gaussian and their functional form changes from scale to scale. A convenient way to quantify deviations from Gaussian statistics is to calculate the flatness  $F_l = \langle \delta v_l^4 \rangle / \langle \delta v_l^2 \rangle^2$ , as shown in the inset of Fig. 6-2(a). It can be seen that  $F_l$  depends on  $l$  and increases rapidly from 3.5 to 8 as  $l$  decreases. These flatness values are considerably greater than the Gaussian value  $F=3$ . The increasing flatness for small  $l$  also suggests that turbulent fluctuations are not space filling and may be characterized by fractal distributions [62].

It was conjectured in Obukhov and Kolmogorov's 1962 study [49, 86] that the source of intermittency in turbulence is a non-uniform distribution of the energy dissipation rate  $\varepsilon_l$ , where  $\varepsilon_l$  is averaged over the scale  $l$ . Thus, it would be useful to directly measure  $\varepsilon_l$  and to elucidate the direct cause of the burstiness in the velocity field. However such an approach is not practical because of the uncertainties associated with taking derivatives of the velocity field deep in a dissipative scale. In the present case, as mentioned above, even at the scale of 100  $\mu\text{m}$ , the velocity field is still active and jagged enough to invalidate such a procedure. Instead, in the following investigation we used the velocity structure functions  $S_q(l)$  calculated from the pdfs to quantify intermittency. We point out that this approach, though overcoming the smoothness problem, has the hidden assumption  $\delta v_l \sim (\varepsilon_l l)^{1/3}$ , which is known as the Kolmogorov Refined Similarity Hypothesis (KRSH) [49]. Figure 6-4(a) displays a set of measurements of  $S_q(l)$  for  $q$  varying between 1 to 8. We found that to a good approximation, all  $S_q(l)$  are power laws of  $l$ ,  $S_q(l) \sim l^{\zeta_q}$ . The exponent  $\zeta_q$  increases monotonically as a function of  $q$  as shown in Fig. 6-4(b). The error bars in the figure were estimated based on noises in the fit to the power-law scaling. In the absence of intermittency,  $\zeta_q$  is expected to scale linearly with  $q$  with the slope 3/5 according

to the Bolgiano theory (dotted line) and 0.5 based on our measured  $S_{(3)}(l)$  (dot-dashed line). It is evident from Fig. 6-4(b) that  $\zeta_q$  is not linear in  $q$ , confirming our assertion that turbulence is intermittent and that a multi-scale analysis is warranted [62].

A simple model that accounts for scale-to-scale energy dissipation is the random cascade model [62]. Imagine a 2D square domain of size  $l_0$  that has a mean energy dissipation rate  $\varepsilon_0$ . This domain is subdivided into four equal pieces of size  $l_0/2$ . Assign each piece with a dissipation rate  $\varepsilon_{l_0/2} = \varepsilon_0 W_1$ , which is randomly weighed by  $W_1$ . It is evident that for  $\varepsilon_0$  to be conserved,  $\langle W_1 \rangle = 1$ . Following this procedure, each of the small squares can be subdivided multiple times and at the  $n$ th generation, one ends up with square patches of size  $l = l_n = l_0(1/2)^n$  and  $\varepsilon_l = \varepsilon_0 W_1 W_2 \dots W_n$ . The problem becomes tractable if one assumes that  $W_i$  is lognormally distributed, i.e.,  $W_i = (1/2)^{m_i}$  with  $P(m_i) \sim \exp(-(m_i - \bar{m})^2 / 2\sigma^2)$ , where  $\bar{m}$  is the mean and  $\sigma$  is the standard deviation. It follows that  $\varepsilon_l / \varepsilon_0 = (1/2)^{m_1 + m_2 + \dots + m_n} = (1/2)^{nx} = (l/l_0)^x$ , where  $x = (m_1 + m_2 + \dots + m_n)/n$  is itself a random number obeying the distribution  $P(x) \sim \exp(-(x - \bar{x})^2 / 2\sigma_x^2)$ . It can be shown that  $\bar{m} = \bar{x}$  and  $\sigma_x^2 = \sigma^2/n$ . The normalization condition  $\langle W_i \rangle = 1$  further constrains  $\bar{m}$  and  $\sigma$  with the result  $\bar{m} = \sigma^2 \ln(2) / 2 = \sigma^2 \ln(l_0/l) / (2n)$ . Thus within the lognormal assumption, the mean and fluctuations are correlated and can be characterized by a single parameter  $\mu = 2\bar{m}$ . The above description shows that the model is purely geometrical and says nothing about the direction of the cascade. The random cascade model thus should be applicable to 2D as well as 3D turbulence.

To make progress, it is further assumed that KRSH can be applied to the BR of 2D convection in soap films. The interaction between the KE of turbulence and the PE of stratification dictates that  $\varepsilon_l$  is not a constant even in the absence of intermittency but depends on  $l$  as  $\varepsilon_l = \varepsilon' l^\gamma$ , where  $\gamma \approx 1/2$  based on our  $S_{(3)}(l)$  measurement [88]. Because of the presence of inverse energy cascade in our system,  $\varepsilon_l$  may be more appropriately interpreted as an energy flux on scale  $l$  rather than the energy dissipation rate. The above  $l$  dependence of  $\varepsilon_l$  reflects the physical reality of an energy *leakage* to PE and is the basis of the steepening of the energy spectrum  $E(k)$  compared to barotropic turbulence [48]. In the presence of intermittency, the

coefficient  $\varepsilon'$  is no longer constant but is itself fluctuating, giving rise to a nontrivial scale dependence  $\varepsilon'=\varepsilon'_l$ . Consistent with the KRSH, we found  $(\delta v_l/\delta v_0)^q=(\varepsilon'_l/\varepsilon'_0)^{q/3}(l/l_0)^{\gamma q}=(l/l_0)^{xq/3+\gamma q}$ , where  $\gamma\approx 1/2$ . The structure function  $S_q(l)$  is defined by averaging  $|(\delta v_l/\delta v_0)|^q$  over the distribution  $P(x)$ . It follows, using a saddle-point approximation, that  $S_q(l)\sim(l/l_0)^{\zeta_q}$  and that the scaling exponent  $\zeta_q$  is given by

$$\zeta_q=q/2+(\mu/18)(3q-q^2). \quad (6.1)$$

When Eq. (1) was compared to the data in Fig. 6-4(b), a remarkably good fit was achieved as delineated by the solid line in the figure. The fitting procedure yields  $\mu=0.42\pm 0.01$ .

### 6.5. Summary

To summarize, we have performed simultaneous two-point velocity measurements in turbulent convection in a soap film. A unique feature of the experiment is that density stratification is significant and there is a strong interaction between the KE of turbulence and PE of stratification. Though the system size is small ( $2\times 2\text{ cm}^2$ ), it shows hallmarks of turbulence including strong intermittency. In contrast with barotropic turbulence in 3D, intermittency in 2D convection emerges as a large-scale phenomenon. Although our theoretical analysis follows the line of thought developed by Obukhov and Kolmogorov [49, 86], the interpretation of intermittency differs from theirs. We believed that the source of intermittency in buoyancy driven flow is not determined by molecular friction but instead by the interaction between the KE of turbulence and the PE of stratification. Such a view is supported by the fact that despite showing canonical features of turbulence, the Reynolds number in our system is modest,  $Re\sim 500$  using the system size and  $Re_\lambda\sim 50$  using a Taylor micro-scale [62]. These  $Re$  are at least a factor of ten smaller than 3D wind-tunnel turbulence, where strong intermittency is reported [84]. However, even for these very large  $Re$  experiments, the intermittency characterized by  $\mu$  is about 0.20, smaller than in our experiment. Another line of evidence that favors our view is the observed inverse energy cascade, which precludes intense energy dissipation on small scales.

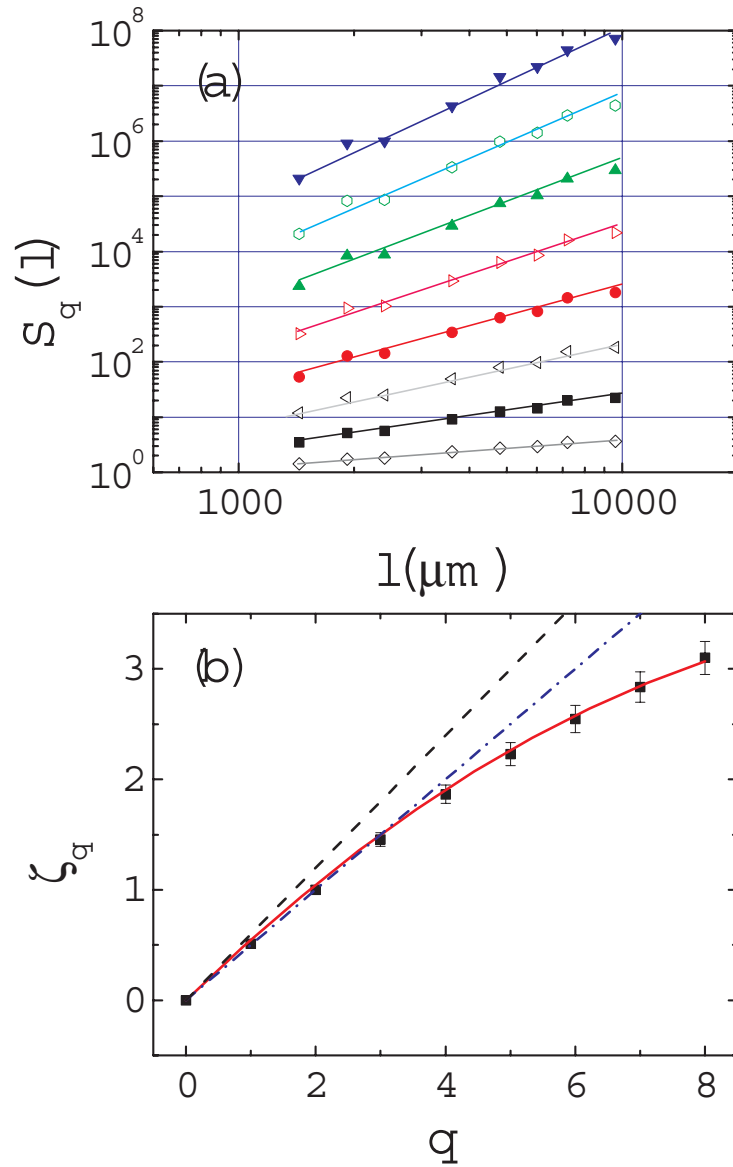


Figure 6-4: (a) The log-log plot of  $S_q(l) \sim l^{\zeta_q}$  for  $1 \leq q \leq 8$  in the Bolgiano regime. (b) The exponent  $\zeta_q$  is plotted against  $q$ . The dashed line is based on Bolgiano's theory, the dot-dashed line is our measurement, assuming no intermittency, and the solid line is the fit to the random cascade model  $\zeta_q = q/2 + (\mu/18)(3q - q^2)$ , where  $\mu = 0.42$ .

## BIBLIOGRAPHY

1. Kadanoff, L.P., *Turbulent Heat Flow: Structures and Scaling*. Physics Today, 2001. August: p. 34.
2. Strogatz, S.H., *Nonlinear Dynamics and Chaos: With Applications to Physics, Biology, Chemistry and Engineering*. 2001: Perseus Books Group.
3. Kundu, P.K. and Ira M., Cohen, *Fluid Mechanics*. 3rd edition (April 8, 2004): Academic Press.
4. Landau, L.D. and E.M. Lifshitz, *Fluid Mechanics*. 1987, New York: Pergamon Press.
5. Couder, Y., J.M. Chomaz, and M. Rabaud, *On the Hydrodynamics of Soap Films*. Physica D, 1989. **37**: p. 384.
6. Gharib, M. and P. Derango, *A Liquid Film Tunnel to Study Two Dimensional Laminar and Turbulent Shear Flows*. Physica D, 1989. **37**: p. 406.
7. Kellay, H., X.L. Wu, and W.I. Goldburg, *Experiments with Turbulent Soap Films*. Physical Review Letters, 1995. **74**(20): p. 3975.
8. Burgess, J.M., et al., *Instability of the Kolmogorov flow in soap film*. Phys. Rev. E, 1999. **60**: p. 715-721.
9. Zhang, J., et al., *One-dimensional flags in a two-dimensional wind*. Nature, 2000. **408**: p. 835-839.
10. Rutgers, M.A., X.L. Wu, and W.B. Daniel, *Conducting Fluid Dynamics Experiments with Vertically Falling Soap Films*. Rev. Sci. Instrum., 2001. **72**: p. 3025.
11. Rivera, M. and X.L. Wu, *Homogeneity and the Inertial Range in Driven 2D Turbulence*. Phys. Fluids, 2002. **14**: p. 3098.
12. Chomaz, J.M., *The dynamics of a viscous soap film with soluble surfactant*. J. Fluid Mech., 2001. **442**: p. 387-409.
13. Kraichnan, R.H. and D. Montgomery, *Two-Dimensional Turbulence*. Rep. Prog. Phys, 1980. **43**: p. 547.
14. Chertkov, M., et al., *Statistics of a passive scalar advected by a large-scale two-dimensional velocity field*. Phys. Rev. E, 1995. **51**: p. 5609.

15. Bracco, A., et al., *Revisiting freely decaying two-dimensional turbulence at millennial resolution*. Phys. Fluids, 2000. **12**: p. 2931.
16. Christov, C.I. and G.M. Homsy, *Nonlinear dynamics of two-dimensional convection in a vertically stratified slot with and without gravity modulation*. J. Fluid Mech., 2001. **430**: p. 335-360.
17. Martin, B. and X.L. Wu, *Double-Diffusive Convection in Freely Suspended Soap Films*. Physical Review Letters, 1998. **80**(9): p. 1892.
18. Godfrey, M.I. and D.H. Van Winkle, *Surface-tension-gradient-induced flow in freely suspended liquid crystal films*. Phys. Rev. E, 1996. **54**: p. 3752.
19. Birnstock, J. and R. Stannarius, *Vertically suspended smectic films with in-plane temperature gradients*. Mol. Cryst. Liq. Cryst., 2001. **366**: p. 815.
20. Moore, D.R. and N.O. Weiss, *Two-dimensional Rayleigh-Benard Convection*. J. Fluid Mech, 1973. **58**: p. 289-312.
21. Curry, J.H., et al., *Order and disorder in two- and three-dimensional Benard convection*. J. Fluid Mech., 1984. **147**: p. 1-38.
22. Werne, J., *Structure of hard-turbulent convection in two dimensions: Numerical evidence*. Phys. Rev. E, 1993. **48**: p. 1020.
23. Celani, A., A. Mazzino, and M. Vergassola, *Thermal plume turbulence*. Physics of fluids, 2001. **13**: p. 2133.
24. Biskamp, D., K. Hallatschek, and E. Schwarz, *Scaling laws in two-dimensional turbulent convection*. Phys. Rev. E, Rapid Communications, 2001. **63**: p. 045302-1.
25. Wu, X.L., et al., *Infrared Technique for Measuring Thickness of a Flowing Soap Film*. Rev. Sci. Instrum., 2001. **72**: p. 2467.
26. Kellay, H., *Dispersion in the enstrophy cascade of two-dimensional decaying turbulence*. Phys. Rev. E, 2004. **69**: p. 036305.
27. Bolgiano Jr., R., *The role of turbulent mixing in scatter propagation*. IEEE Transactions on Antennas and Propagation, 1958. **6**(2): p. 161-168.
28. Bolgiano Jr., R., *Turbulent Spectra in a Stably Stratified Atmosphere*. J. Geophys. Research, 1959. **64**: p. 2226.
29. Merzkirch, W., *Flow Visualization*. 1987, New York: Academic Press, Inc.

30. Busse, F.H., *Non-linear properties of thermal convection*. Rep. Prog. Phys, 1978. **41**: p. 1929-1967.
31. Castaing, B., et al., *Scaling of hard thermal turbulence in Rayleigh-Benard convection*. J. Fluid Mech., 1989. **204**: p. 1-30.
32. Glazier, J.A., et al., *Evidence against 'ultrahard' thermal turbulence at very high Rayleigh numbers*. Nature, 1999. **398**: p. 307.
33. Niemela, J.J., et al., *Turbulent convection at very high Rayleigh numbers*. Nature, 2000. **404**: p. 837.
34. Rogers, T.M., G.A. Glatzmaier, and S.E. Woosley, *Simulation of two-dimensional turbulent convection in a density-stratified fluid*. Phys. Rev. E, 2003. **67**: p. 026315-1.
35. Qiu, X.L. and P. Tong, *Large-scale velocity structures in turbulent thermal convection*. Phys. Rev. E, 2001. **64**: p. 036304-1.
36. Landau, L.D. and E.M. Lifshitz, *Statistical Physics (I)*. 1986, New York: Pergamon Press.
37. Ma, X.L., et al., *Simultaneous retrieval of atmospheric profiles, land-surface temperature, and surface emissivity from moderate resolution imaging spectroradiometer thermal infrared data: extension of a two-step physical algorithm*. Applied Optics, 2002. **41**: p. 909-924.
38. Dutova, K.P., V.N. Morozov, and E.N. Smimova, *Infrared Spectra of Inorganic Glasses and Crystals*. 1972, Leningrad: Ckimia Press.
39. Shen, Y., P. Tong, and K.-Q. Xia, *Turbulent Convection over Rough Surfaces*. Phys. Rev. Lett., 1996. **76**: p. 908.
40. Daya, Z.A. and R.E. Ecke, *Does Turbulent Convection Feel the Shape of the Container?* Phys. Rev. Lett., 2001. **87**: p. 184501-1.
41. Holzer, M. and E.D. Siggia, *Turbulent mixing of a passive scalar*. Phys. Fluids, 1994. **6**: p. 1820.
42. Krishnamurti, R. and L.N. Howard, *Large-scale flow generation in turbulent convection*. Proc. Natl. Acad. Sci. USA, 1981. **78**: p. 1981.
43. Wu, X.Z. and A. Libchaber, *Scaling relations in thermal turbulence: The aspect-ratio dependence*. Phys. Rev. A, 1992. **45**: p. 842.
44. Qiu, X.-L. and P. Tong, *Temperature oscillations in turbulent Rayleigh-Benard convection*. Phys. Rev. E, 2002. **66**: p. 026308-1.

45. Shang, X.-D., et al., *Measured Local Heat Transport in Turbulent Rayleigh-Benard Convection*. Phys. Rev. Lett., 2003. **90**: p. 074501-1.
46. Sano, M., X.Z. Wu, and Libchaber, *Turbulence in helium-gas free convection*. Phys. Rev. A, 1989. **40**: p. 6421.
47. Kolmogorov, A.N., *The local structure of turbulence in incompressible viscous fluid for very large Reynolds number*. Dokl. Akad. Nauk SSSR, 1941. **30**: p. 9.
48. L'vov, V.S., *Spectra of Velocity and Temperature Fluctuations with Constant Entropy Flux of Fully Developed Free-Convective Turbulence*. Phys. Rev. Lett., 1991. **67**: p. 687.
49. Kolmogorov, A.N., *A refinement of previous hypotheses concerning the local structure of turbulence in a viscous incompressible fluid at high Reynolds number*. J. Fluid Mech., 1962. **13**: p. 82.
50. Stolovitzky, G. and K.R. Sreenivasan, *Kolmogorov's refined similarity hypotheses for turbulence and general stochastic processes*. Reviews of Modern Physics, 1994. **66**: p. 229.
51. Wheelon, A.D., *Spectrum of Turbulent Fluctuations Produced by Convective Mixing of Gradients*. Phys. Rev., 1957. **105**: p. 1706.
52. Villars, F. and V.F. Weisskopf, *The scattering of electromagnetic waves by turbulent atmospheric fluctuations*. Phys. Rev., 1954. **94**: p. 232.
53. Mydlarski, L. and Z. Warhaft, *Passive scalar statistics in high-Peclet-number grid turbulence*. J. Fluid Mech., 1998. **358**: p. 135.
54. Zolotarev, V.M., et al., *Dispersion and absorption of liquid water in infrared and radio regions of the spectrum*. Optics and Spectroscopy, 1969. **27**: p. 430-432.
55. Since the fluid motion is 3D incompressible, it follows that the 2D divergence of the velocity is given by  $\nabla_2 \cdot \vec{v}_2 = (\partial_x v_x + \partial_y v_y) = -\partial_z v_z \approx -\delta v_z / \delta h$ . The rms fluctuations of  $\nabla_2 \cdot \vec{v}_2$  and  $\delta h$  were directly measured with the result  $\langle (\nabla_2 \cdot \vec{v}_2)^2 \rangle^{1/2} = 15 \text{ s}^{-1}$  and  $\langle \delta h^2 \rangle^{1/2} \approx 1 \text{ } \mu\text{m}$ . This yields  $\langle \delta v_z^2 \rangle^{1/2} = 1.5 \times 10^{-3} \text{ cm/s}$  or  $\langle \delta v_z^2 \rangle^{1/2} / v_{\text{rms}} = 5 \times 10^{-4}$ . Thus, compressibility of the film cannot affect 2D motion of the film.
56. Rivera, M. and X.L. Wu, *External dissipation in driven soap film turbulence*. Phys. Rev. Lett., 2000. **85**: p. 976.
57. Tsai, P.C., Z. Daya, and S.W. Morris, *Aspect-ratio dependence of charge transport in turbulent electroconvection*. Phys. Rev. Lett., 2004. **92**: p. 084503.

58. Cressman, J.R., et al., *Eulerian and Lagrangian Studies in Surface flow turbulence*. New J. Phys., 2004. **6**: p. 53.
59. Batchelor, G.K., *Small-scale variation of convected quantities like temperature in turbulent fluid*. J. Fluid Mech., 1958. **5**: p. 113.
60. Wu, X.Z., et al., *Frequency Power Spectrum of Temperature Fluctuations in Free Convection*. Phys. Rev. Lett., 1990. **64**: p. 2140.
61. Tong, P. and Y. Shen, *Relative Velocity Fluctuations in Turbulent Rayleigh-Benard Convection*. Phys. Rev. Lett., 1992. **69**: p. 2066.
62. Frisch, U., *Turbulence*. 1995, Cambridge: Cambridge University Press.
63. Meneveau, C. and K.R. Sreenivasan, *The multifractal nature of turbulent energy dissipation*. J. Fluid Mech, 1991. **224**: p. 429-484.
64. Ramshankar, R. and J.P. Gollub, *Transport by capillary waves. Part II: Scalar dispersion and structure of the concentration field*. Phys. Fluids, 1991. **3**(5): p. 1344.
65. Procaccia, I. and H.G.E. Hentschel, *The infinite number of generalized dimensions of fractals and strange attractors*. physica D, 1983. **8**(3): p. 435.
66. Cao, N. and S. Chen, *An intermittency model for passive-scalar turbulence*. Phys. Fluids, 1997. **9**(5): p. 1203.
67. Gallavotti, G. and E.G.D. Cohen, *Dynamical Ensembles in Nonequilibrium Statistical Mechanics*. Physical Review Letters, 1995. **74**(14): p. 2694.
68. Goldberg, W.I., Y.Y. Goldschmidt, and H. Kellay, *Fluctuation and Dissipation in Liquid-Crystal Electroconvection*. Physical Review Letters, 2001. **87**(24): p. 245502.
69. Wang, G.M., et al., *Experimental Demonstration of Violations of the Second Law of Thermodynamics for Small Systems and Short Time Scales*. Physical Review Letters, 2002. **89**: p. 50601.
70. Lumley, J.L., *Similarity and the Turbulent Energy Spectrum*. Phys. Fluids, 1967. **10**(4): p. 855.
71. Mydlarski, L., et al., *Structures and multipoint correlators for turbulent advection: predictions and experiments*. Phys. Rev. Lett., 1998. **81**: p. 4373.
72. Shraiman, B.I. and E.D. Siggia, *Scalar Turbulence*. Nature, 2000. **405**: p. 639.
73. Bolgiano J., R., *Spectrum of Turbulent Mixing*. Physical Review, 1957. **108**(5): p. 1348.

74. Obukhov, A.M., Dolk. Akad. Nauk. SSSR, 1959. **125**: p. 1246.
75. Falkovich, G. and V. Lebedev, *Single-Point Velocity Distribution in Turbulence*. Phys. Rev. Lett., 1997. **79**: p. 4159.
76. Chomaz, J.M. and B. Cathalau, *Soap films as two-dimensional classical fluids*. Phys. Rev. A, 1990. **41**: p. 2243.
77. XI, H.-D., S. LAM, and K.-Q. XIA, *From laminar plumes to organized flows: the onset of large-scale circulation in turbulent thermal convection*. J. Fluid Mech., 2004. **503**: p. 47.
78. SETHNA, J.P., K.A. DAHMEN, and C.R. MYERS, *Crackling noise*. Nature, 2001. **410**: p. 242.
79. Lumley, J.L. and I. Kubo, *The Influence of Polymer Additives on Velocity and Temperature Fields*, ed. G. Gampert. 1984, Berlin: Springer.
80. Boffetta, G., A. Gelani, and S. Musacchio, *Two-Dimensional Turbulence of Dilute Polymer Solutions*. Phys. Rev. Lett., 2003. **91**: p. 034501-1.
81. Celani, A., et al., *Active and passive fields face to face*. New Journal of Physics, 2004. **6**: p. 1.
82. Ching, E.S.C., et al., *Intermittency of velocity fluctuations in turbulent thermal convection*. Phys. Rev. E, 2003. **68**: p. 026307-1.
83. L'vov, V.S., A. Pomyalov, and I. Procaccia, *Quasi-Gaussian Statistics of Hydrodynamic Turbulence in 4/3+epsilon dimensions*. Phys. Rev. Lett., 2002. **89**: p. 064501-1.
84. Anselmet, F., et al., *High-order velocity structure functions in turbulent shear flow*. J. Fluid Mech., 1984. **140**: p. 63-89.
85. To find  $l_B$ , we estimated  $\varepsilon(=v_{rms}^3/L)$  and  $\chi_\rho(=d(\delta\rho_2)^2/dt\sim(1/\tau)(\delta\rho_2)^2)$ , where  $\tau$  is the typical eddy turnover time. For our measurements,  $v_{rms}=5$  cm/s,  $L=2$  cm,  $\delta\rho_2/\rho_2\sim 0.3$  and  $\tau\sim 2\pi(L/2)/v_{rms}=1.26$  s, this gives  $l_B=2\pi(\chi_\rho^{3/4}(g/\rho_2)^{3/2}/\varepsilon^{5/4})^{-1}=0.26$  cm.
86. Obukhov, A.M., *Some specific features of atmospheric turbulence*. J. Fluid Mech., 1962. **13**: p. 77.
87. Tabeling, P., *Two dimensional turbulence: a physicist approach*. Phys. Rep., 2002. **362**: p. 1.
88. Theoretically  $\varepsilon'_l$  should scale as  $\varepsilon'_l\sim l^{4/5}$  if  $S_2(l)\sim l^{6/5}$ . However, since our measurements show  $S_2(l)\sim S_{(3)}(l)^{2/3}\sim(\varepsilon'_l l)^{2/3}\sim l$ ,  $\varepsilon'_l\sim l^{1/2}$  is used instead.